Calculation of the Dzyaloshinskii-Moriya Interaction in ultrathin magnetic Films: Cr/W(110)

von

Bernd Zimmermann

Diplomarbeit in Physik

vorgelegt der

Fakultät für Mathematik, Informatik und Naturwissenschaften
der Rheinisch-Westfälischen Technischen Hochschule Aachen

im
Mai 2010

angefertigt am

Institut für Festkörperforschung (IFF)
Forschungszentrum Jülich

Contents

4

1 Introduction

Since many years, there has been great interest in the magnetic structure of thin film systems as they proved to be the source of a wide spectrum of fascinating properties. One main goal was to determine magnetic properties such as magnetic order (ferro- or antiferromagnetic), the direction of magnetic moments, the formation of magnetic domains and their stability, as well as their thermodynamical properties. Insights in these properties had a big influence in the field of data storage devices, which use magnetic thin film systems to store information in terms of magnetization directions (magnetization pointing up and down corresponding to bit '1' and '0', respectively), and the data density could be increased by several orders of magnitude by designing tailored thin film systems. Over the past 10 years a consistent understanding of the magnetism in thin magnetic films and heterostructures developed and theoretical and experimental findings converged (for summary see for example the review [1]). Open questions arose in molecular magnets and magnetic wires.

Therefore it came as an unexpected surprise as Kubetzka et al. [2] observed that all domain-walls in in a thin film of two monolayers of Fe on W(110) have one rotational sense. Statistically one would expect an equal distribution of left and right rotating domain walls. A new vista of thin film magnetism opened with the discovery of a new magnetic phase in an atomic monolayer of Mn on a W(110) substrate [3], whose ground state is a spiraling magnetic structure of unique rotational sense. The occurrence of this phase can only be explained by considering also the so called Dzyaloshinskii-Moriya interaction (DMI) [4,5]. It arises due to electrons propagating in inversion asymmetric environments and is of the form

$$E_{\mathrm{DM}} = \mathbf{D}_{ij} \cdot (\mathbf{S}_i \times \mathbf{S}_j) \; , \tag{1.1}$$

with $\mathbf{D}$ being the Dzyaloshinskii-vector and $\mathbf{S}_i$ and $\mathbf{S}_j$ two magnetic moments on lattice sites i and j, respectively. The DMI favors spiraling magnetic structures of unique rotational sense, depending on the sign of $\mathbf{D}$, in contrast to other important interactions as the Heisenberg exchange (usually preferring collinear magnetic structures or spirals without being sensitive to the rotational direction) or the magnetocrystalline anisotropy energy (preferring collinear alignment of magnetic moments in a certain crystallographic direction). These competing interactions give rise to a variety of possible magnetic ground states due to frustration.

The DMI can also explain other experimental observations [6], e.g. the regular formation of domain walls in a double layer Fe on W(110) [7,8], and their unique sense of rotation along a path from one domain to the next. A detailed understanding of this new kind of interaction may have impact in the context of facilitating applications in spintronics and spin-dependent transport.

The DMI is a relativistic effect, because spin-orbit coupling (SOC) – meaning that the intrinsic spin degree of freedom of an electron is coupled to its orbital motion – is crucial for its occurrence. The contribution of SOC to the total energy is small and methods with very high accuracy are needed. Density functional theory (DFT) [9, 10] has become a powerful tool in theoretical solid state physics to study ground-state properties of complex, realistic many-electron systems with astonishing accuracy from ab-initio (meaning that no external parameters than the positions and charges of nuclei are needed). In this thesis one of the most accurate methods, namely the full-potential linearized augmented plane-wave (FLAPW) method [11, 12] as implemented in the FLEUR code [13] is used.

It is not straightforward to implement the calculation of the Dzyaloshinskii-Moriya interaction efficiently in the existing ab-initio methods, because the combination of spin-spiral calculations and spin-orbit coupling is needed. One especially faces problems, when the SOC energy of spin spirals with period lengths over several chemical unit cells shall be calculated. In the standard methods, which utilize a supercell in which the magnetic structure is commensurate, the determination becomes impossible due to the huge number of atoms in the magnetic unit cell. In this thesis, a recently implemented perturbative treatment has been used, which treats spin-orbit coupling in first order perturbation theory [14]. This method allows for calculations in the chemical unit cell. However, because of the desired high numerical accuracy, the solution of the underlying physical equations can be done only on state of the art supercomputers.

From an experimental point of view, scanning tunneling microscopy with a spin-polarized tip (SP-STM) allows to study the magnetic properties of thin-film systems on an atomic length scale and allows for comparison with the theoretical results.

A few thin-film systems consisting of $3d$-transition metal layers (a double layer Fe [2, 7, 8] or a monolayer Mn [3, 6]) on a tungsten substrate have been investigated by means of both, DFT and SP-STM, and it was found that the Dzyaloshinskii-Moriya interaction influences their magnetic structure. However, more systems must be studied to obtain a chemical trend and to understand, which quantities determine e.g. the sign and the strength of the DMI. In this thesis we present investigations on the magnetic structure of a monolayer of Cr on W(110) by means of density functional theory. Because of the high spin-orbit coupling strength of the heavy W atoms combined with their magnetic moment induced by the antiferromagnetically ordered Cr-layer, this system is a promising candidate for a strong DMI.

It is a widely used approach to determine the ground state by means of a model, where the required model parameter are obtained by ab-initio calculations. We use a micromagnetic model, because magnetic structures are expected to appear on long length scales compared to the interatomic distance. Three energy contributions are taken into account: the spin stiffness (corresponding to the Heisenberg exchange), the magnetocrystalline anisotropy and the Dzyaloshinskii-Moriya interaction.

This thesis is structured as follows: In chapter 1 and 2 introductions to DFT and the FLAPW method is given, respectively. In chapter 3 and 4 the important magnetic interactions and the micromagnetic model and its solutions are discussed. The system of a free-standing monolayer of Cr is investigated in chapter 5. The spin stiffness is

determined here and special focus was laid on the required numerical cutoffs and errors of applied approximations, e.g. the force theorem. Chapter 6 provides the detailed analysis of the system of a monolayer of Cr on a W(110) substrate. We investigate structural and magnetic properties of the system. We extract the three model parameters from spin-spiral calculations with the FLAPW method. Finally, in chapter 7 we compare our findings to the other systems investigated so far.

2 Density Functional Theory

2.1 The microscopic Hamiltonian in solid state physics

In principle, the stationary Schrödinger equation for a complex many-body problem in solid state physics is known to be

$$\mathcal{H}\left|\Psi\right\rangle = E\left|\Psi\right\rangle \ , \tag{2.1}$$

where $\mathcal{H}$ is the Hamilton operator (also called Hamiltonian), $\left|\Psi\right\rangle$ is the many-body wavefunction and E the eigenenergy of the system. In the following, a system consisting of N_e electrons with mass m and N_k nuclei with (maybe different) mass M_k shall be considered. The Hamiltonian (in the following written in position representation) consists of five different contributions:

$$
\begin{aligned}
\mathcal{H} = \ & -\sum_{i=1}^{N_e} \frac{\hbar^2}{2m}\frac{\partial^2}{\partial \mathbf{r}_i{}^2} - \sum_{k=1}^{N_k} \frac{\hbar^2}{2M_k}\frac{\partial^2}{\partial \mathbf{R}_k{}^2} \\
& + \sum_{i<j} \frac{e^2}{|\mathbf{r}_i - \mathbf{r}_j|} + \sum_{k<l} \frac{Z_k\,Z_l\,e^2}{|\mathbf{R}_k - \mathbf{R}_l|} \\
& - \sum_{i,k} \frac{Z_k\,e^2}{|\mathbf{r}_i - \mathbf{R}_k|} \ ,
\end{aligned}
\tag{2.2}
$$

where the terms in the first line correspond to the kinetic energy of electrons and nuclei, respectively, in the second line they correspond to the electron-electron and nucleus-nucleus interaction and the third line corresponds to the interaction of the electrons with the nuclei. $2\pi\,\hbar$ is Planck's constant, e the elementary charge, and r_i and R_k denote the position of an electron and nuclei, respectively.

If one rewrites the problem to atomic units, which means that lengths are expressed in Bohr radii $a_0 = \hbar^2/me^2$ and energies are expressed in Hartree e^2/a_0, one finds

$$
\begin{aligned}
\mathcal{H} \ = \ & \underbrace{-\frac{1}{2}\sum_i \frac{\partial^2}{\partial \tilde{\mathbf{r}}_i^2}}_{T_{\mathrm{e}}} \underbrace{-\frac{1}{2}\sum_k \frac{m}{M_k}\frac{\partial^2}{\partial \tilde{\mathbf{R}}_k^2}}_{T_{\mathrm{k}}} \\
& + \underbrace{\sum_{i<j} \frac{1}{|\tilde{\mathbf{r}}_i - \tilde{\mathbf{r}}_j|}}_{V_{\mathrm{e-e}}} + \underbrace{\sum_{k<l} \frac{Z_k Z_l}{\left|\tilde{\mathbf{R}}_k - \tilde{\mathbf{R}}_l\right|}}_{V_{\mathrm{K-K}}} - \underbrace{\sum_{i,k} \frac{Z_k}{\left|\tilde{\mathbf{r}}_i - \tilde{\mathbf{R}}_k\right|}}_{V_{\mathrm{e-K}}} \ .
\end{aligned}
\tag{2.3}
$$

Here one can already see, that the contribution of the kinetic energy of the nuclei is relatively small because of the mass ratio of order $m/M_k \approx 10^{-3} - 10^{-5}$. Thus, one can assume that the nuclei are frozen (i.e. $T_K = 0$), which means that the electrons move in a static potential caused by the nuclei. This approximation is also called *adiabatic approximation* or *Born-Oppenheimer approximation*. The positions of the nuclei $\{\mathbf{R}_k\}$ enter the Hamiltonian only as parameters in V_{e-K} and V_{K-K}.

In the Born-Oppenheimer approximation one is left with the problem of solving the Schrödinger equation for N_e electrons in a static potential. This is not an easy task, because the number of degrees of freedom is still very big. Additionally, the Schrödinger equation cannot be solved exactly due to the non-local electron-electron interaction and the requirement that the many body wavefunction must be antisymmetric under exchange of two electrons (because of the Pauli principle) makes the solution even more difficult. A powerful method to treat such problems is called *Density Functional Theory* and will be introduced in the next section 2.2.

2.2 Theorem from Hohenberg and Kohn

The calculation of the electronic many-body wavefunction $\Phi(\mathbf{x}_1, \ldots, \mathbf{x}_N)$ of a system with N electrons is a very demanding task. The Schrödinger equation cannot be solved due to the enormous number of degrees of freedom for a realistic model of a material. Additionally, the many-body wavefunction must be antisymmetric under exchange of two particles because electrons are fermions (Pauli principle). And as a third problem, it is impossible to store Φ in the memory of a computer. However, it contains too much information for most purposes, and in density functional theory a less involved property, namely the density

$$n(\mathbf{r}) = \langle \Phi | \sum_{i=1}^{N} \delta(\mathbf{r} - \mathbf{r}_i) | \Phi \rangle \; , \tag{2.4}$$

is used as basic variable. This is a far more simple quantity, because it depends only on 3 spatial variables instead of $3N$. Hohenberg an Kohn [9] proved that

- all ground-state properties are unique functionals of the (ground-state) density $n_0(\mathbf{r})$,

- the ground-state density minimizes the energy functional $E[n]$:
  $E[n] > E[n_0]$ for all $n \neq n_0$.

The first theorem is quite astonishing, because starting from the exact many-body wavefunction the number of degrees of freedom has been reduced drastically and still all information on the ground state is retained in the density. The energy functional used in the second theorem can be written in two terms:

$$E[n] = \int v_{\text{ext}}(\mathbf{r}) \, n(\mathbf{r}) \, \mathrm{d}\mathbf{r} + F[n] \; , \tag{2.5}$$

where $v_{\text{ext}}(\mathbf{r})$ denotes the external potential, which is generated by the (fixed) nuclei and other external fields. All remaining energy contributions, such as inter-electronic

interactions and kinetic energy, are summed up in $F[n]$, which is universal (i.e. it does not depend on the system), but unfortunately it is not known exactly.

2.3 The Kohn-Sham system

Despite the fact that the unique functional $F[n]$ is not known, Kohn and Sham [10] rewrote the energy functional (2.5) so that reasonable approximations could be made. The main idea is to treat the complex many-body problem as a problem of non-interacting electrons that lead to the same density as the true system. These electrons are moving in an effective potential, which is generated by the nuclei and the other electrons. The major advantage of this picture is, that one can work now with single-particle wavefunctions $\psi_i(\mathbf{r})$ and that the major contribution to the kinetic energy is known explicitly.

$$E[n] = E_{\text{ext}}[n] + \underbrace{T[n] + E_{\text{H}}[n] + E_{\text{xc}}[n]}_{=F[n]} \tag{2.6}$$

Additionally to the kinetic energy $T[n]$, one can also separate the Hartree term $E_{\text{H}}[n]$ from $F[n]$ and remaining many-body effects – such as exchange and correlation – are summed up in E_{xc}. Again, this functional is not known explicitly, but reasonable approximations can be made, e.g. the *local density approximation* (LDA, see section 2.5).

The contributions in equation (2.6) can be written as (in Hartree units)

$$E_{\text{ext}}[n] = \int v_{\text{ext}}(\mathbf{r})n(\mathbf{r})\mathrm{d}\mathbf{r} \ , \tag{2.7}$$

$$T[n] = -\frac{1}{2}\sum_{i=1}^{N} \int \psi_i^*(\mathbf{r})\nabla^2\psi_i(\mathbf{r})\mathrm{d}\mathbf{r} \ , \tag{2.8}$$

$$E_{\text{H}}[n] = \int \frac{n(\mathbf{r})n(\mathbf{r}')}{|\mathbf{r}-\mathbf{r}'|}\,\mathrm{d}\mathbf{r}'\,\mathrm{d}\mathbf{r} \ . \tag{2.9}$$

The ground state is found by minimizing equation (2.6) under the constraint, that the single particle wavefunctions must be normalized. This is done by introducing Lagrange parameters ϵ_i. Variation with respect to ψ_i^* yields the Kohn-Sham-equation,

$$\left(-\frac{1}{2}\nabla^2 + V_{\text{eff}}(\mathbf{r})\right)\psi_i(\mathbf{r}) = \epsilon_i\ \psi_i(\mathbf{r}) \ . \tag{2.10}$$

where the effective potential had been introduced,

$$V_{\text{eff}} = V_{\text{ext}} + V_{\text{Hartree}} + V_{\text{xc}} \tag{2.11}$$

$$= V_{\text{ext}} + 2\int \frac{n(\mathbf{r}')}{|\mathbf{r}-\mathbf{r}'|}\mathrm{d}\mathbf{r}' + \frac{\delta E_{\text{xc}}[n(\mathbf{r})]}{\delta n(\mathbf{r})} \ . \tag{2.12}$$

The density can be written as

$$n(\mathbf{r}) = 2\sum_{i=1}^{N/2} \psi_i^*(\mathbf{r})\psi_i(\mathbf{r}) \ , \tag{2.13}$$

where the summation runs over the $N/2$ states with lowest single particle energies ϵ_i and a factor 2 accounts for the spin degeneracy.

The effective potential (2.11) is not only dependent on $\mathbf{r}$, but also on the electron density. Because the solution ψ_i of the Kohn-Sham equation (2.10) determines the ground state density via equation (2.13), but this density also enters the Kohn-Sham equation, one has to find a self-consistent solution. In DFT, this is done by solving the Kohn-Sham equation iteratively, and thus approaching the ground state density from an initial guess.

2.4 Vector-spin DFT

Without the restriction in (2.13) DFT can also deal with magnetic systems. The ground state (energy) of a magnetic system is not only dependent on the electron density $n(\mathbf{r})$, but also the magnetization density $\mathbf{m}(\mathbf{r})$ [15],

$$E = E[n, \mathbf{m}] \geq E[n_0, \mathbf{m}_0] \ . \tag{2.14}$$

An equivalent and similar form to the Kohn-Sham equation of the non-magnetic case is obtained by replacing the wavefunctions by a two component spinor,

$$\Psi_i(\mathbf{r}) = \begin{pmatrix} \psi_i^\uparrow(\mathbf{r}) \\ \psi_i^\downarrow(\mathbf{r}) \end{pmatrix} \ . \tag{2.15}$$

Then the Kohn-Sham equations for spin-polarized systems reads

$$\left(-\frac{1}{2}\nabla^2 + V_{\mathrm{eff}}(\mathbf{r}) + \mathbf{B}_{\mathrm{eff}} \cdot \boldsymbol{\sigma} \right) \Psi_i(\mathbf{r}) = \epsilon_i \ \Psi_i(\mathbf{r}) \ , \tag{2.16}$$

where $\boldsymbol{\sigma}$ is the vector of the three Pauli spin matrices,

$$\sigma_x = \begin{pmatrix} 0 & 1 \\ 1 & 0 \end{pmatrix}, \quad \sigma_y = \begin{pmatrix} 0 & -i \\ i & 0 \end{pmatrix} \quad \sigma_z = \begin{pmatrix} 1 & 0 \\ 0 & -1 \end{pmatrix}, \tag{2.17}$$

and the effective magnetic field $\mathbf{B}_{\mathrm{eff}}$ consists of two contributions: an external part $\mathbf{B}_{\mathrm{ext}}$ and an exchange-correlation part,

$$\mathbf{B}_{\mathrm{xc}} = \frac{\delta E_{\mathrm{xc}}[n, \mathbf{m}]}{\delta \mathbf{m}(\mathbf{r})} \ . \tag{2.18}$$

The latter is the analogue to the exchange-correlation potential, but now the variation of E_{xc} is done with respect to $\mathbf{m}$ instead of n. The occupied states are determined by the Fermi energy, $\epsilon_i < \epsilon_F$. The resulting densities are then expressed in terms of the spinor wavefunctions

$$n(\mathbf{r}) = \sum_i^{\mathrm{occ.}} \Psi_i^\dagger \Psi_i \ , \tag{2.19}$$

$$\mathbf{m}(\mathbf{r}) = \sum_i^{\mathrm{occ.}} \Psi_i^\dagger \boldsymbol{\sigma} \Psi_i \ . \tag{2.20}$$

2.5 Local (Spin) Density Approximation

Unfortunately, the exchange-correlation energy E_{xc}, which describes all electron-electron interactions beyond the Hartree approximation, is not known. A simple and powerful approximation is the *local density approximation* (LDA), where the functional is replaced by a function and thus becomes local in space,

$$E_{xc}[n, \mathbf{m}] = \int d\mathbf{r} \; \varepsilon_{\mathrm{LDA}}(n(\mathbf{r}), |\mathbf{m}(\mathbf{r})|) \; . \tag{2.21}$$

The function $\varepsilon_{\mathrm{LDA}}$ is the exchange and correlation energy per particle of a homogeneous electron gas. For the exchange part an exact expression can be derived, whereas approximations to the correlation part are obtained by Quantum-Monte-Carlo [16–18] calculations for example. $\varepsilon_{\mathrm{LDA}}$ only depends on the values of the electron density and the magnitude of the magnetization. Because of the local nature of the functional it cannot depend on the direction of the magnetization.

The LDA is exact for systems with constant charge and magnetization density and gives good results for slowly varying densities. However, it turns out that LDA can also be applied to a wider class of systems, even to atomic systems where the densities are far away from being uniform, leading to correct trends across the periodic table [19]. However, a generalization to functions that depend also on gradients, *Generalized Gradient Approximation* (GGA), has been made to give a better description of systems with strongly varying densities. The widely used PBE functional [20] takes only gradients of the density into account:

$$E_{xc}[n, \mathbf{m}] = \int d\mathbf{r} \; \varepsilon_{\mathrm{GGA}}(n(\mathbf{r}), |m(\mathbf{r})|, |\nabla n(\mathbf{r})|) \, . \tag{2.22}$$

The PBE-functional and others [21] were constructed for collinear magnetization densities (i.e. $\mathbf{m}(\mathbf{r}) = m(\mathbf{r})\hat{\mathbf{n}}$, $\hat{\mathbf{n}} = \frac{\mathbf{m}}{|\mathbf{m}|} = $ const) as an approximation to the exchange-correlation energy. It is to emphasize, that these functionals are not constructed to describe non-collinear magnetic densities in contrast to LDA functionals. It was found out that GGA does not lead to more precise results as LDA in the case of transition metals and magnetic materials [22].

One major advantage of the used approximations is that $\mathbf{B}_{\mathrm{xc}} = B_{\mathrm{xc}} \frac{\mathbf{m}}{|\mathbf{m}|}$ is collinear to the magnetization density [23].

2.6 Relativistic corrections

When one describes systems with heavy atoms, relativistic effects become important due to the high kinetic energy of the electrons in the vicinity of the nucleus. A relativistic density functional theory [24] is derived from the Dirac-equation and reads

$$\left\{ c\boldsymbol{\alpha} \cdot \mathbf{p} + \frac{1}{2}\beta c^2 + V_{\mathrm{eff}}(\mathbf{r}) + \mathbf{B}_{\mathrm{xc}} \cdot \boldsymbol{\sigma} \right\} \boldsymbol{\Psi}_\nu(\mathbf{r}) = E_\nu \boldsymbol{\Psi}_\nu(\mathbf{r}) \; , \tag{2.23}$$

where c is the velocity of light, $\mathbf{p}$ is the momentum operator, $E_\nu = \epsilon_\nu + \frac{1}{2}c^2$ is the eigenenergy plus rest mass, $\boldsymbol{\Psi}_\nu$ is a spinor wavefunction with four components and

$$\boldsymbol{\alpha} \;=\; \begin{pmatrix} 0 & \boldsymbol{\sigma} \\ \boldsymbol{\sigma} & 0 \end{pmatrix}, \tag{2.24}$$

$$\beta \;=\; \begin{pmatrix} \mathbb{1} & 0 \\ 0 & -\mathbb{1} \end{pmatrix}. \tag{2.25}$$

Here $\boldsymbol{\sigma}$ denotes the vector of Pauli spin-matrices (cf. section 2.4) and $\mathbb{1}$ is the (2×2) identity matrix.

The 4-component spinor wavefunction $\boldsymbol{\Psi}_\nu$ can be separated into two parts (φ_ν and χ_ν), each having two components,

$$\boldsymbol{\Psi}_\nu = \begin{pmatrix} \varphi_\nu \\ \chi_\nu \end{pmatrix}, \qquad \varphi_\nu = \begin{pmatrix} \varphi_\nu^\uparrow \\ \varphi_\nu^\downarrow \end{pmatrix}, \;\; \chi_\nu = \begin{pmatrix} \chi_\nu^\uparrow \\ \chi_\nu^\downarrow \end{pmatrix}, \tag{2.26}$$

which are called large and small component.

In principle one could solve equation (2.23) directly, but to gain the same accuracy as in the non-relativistic (non-magnetic) case, this would increase the computational effort by a factor of $4^3 = 64$, because solving equation (2.23) (which is equivalent to diagonalize a matrix) scales with the third power. Instead, only relativistic corrections to the Kohn-Sham equation (2.16), which can be derived by a $\frac{1}{c^2}$-expansion of the full Dirac equation (c.f. e.g. [25]), are considered. The Kohn-Sham equation then reads

$$\mathcal{H}_{\text{rel}}\phi_\nu = \epsilon_\nu \phi_\nu \tag{2.27}$$

where the small and large component are expressed in terms of the two-component wavefunction ϕ_ν as

$$\varphi_\nu \;=\; \left(1 - \frac{1}{2\,c^2}\,\mathbf{p}^2\right)\phi_\nu + \mathcal{O}(c^{-4}) \tag{2.28}$$

$$\chi_\nu \;=\; \left(\frac{1}{c}(\boldsymbol{\sigma}\cdot\mathbf{p}) + \frac{1}{c^3}(-\frac{\mathbf{p}^2}{2} + V - \epsilon_\nu)(\boldsymbol{\sigma}\cdot\mathbf{p})\right)\phi_\nu + \mathcal{O}(c^{-5}). \tag{2.29}$$

The corresponding Hamiltonian takes then the form

$$\mathcal{H}_{\text{rel}} = \mathcal{H}_{\text{KS}} \;\; + \;\; \frac{1}{c^2}\left(-\mathbf{p}^4\,\mathbb{1} + \frac{1}{2}\left(\nabla^2(V_{\text{eff}}\,\mathbb{1} + \boldsymbol{\sigma}\cdot\mathbf{B}_{\text{xc}})\right)\right)$$

$$+ \;\; \frac{1}{c^2}\,\boldsymbol{\sigma}\cdot((\nabla V_{\text{eff}})\times\mathbf{p}) + \frac{1}{c^2}\underline{\mathbf{B}} \tag{2.30}$$

where $\mathcal{H}_{\text{KS}}$ is the non-relativistic Kohn-Sham Hamiltonian and $\underline{\mathbf{B}}$ is a (2×2)-matrix whose elements are usually small compared to the other corrections and thus neglected. Let us have a look at the other contributions: The correction in the first line of (2.30) is invariant under rotations in spin space and the non-relativistic Hamiltonian (which also exhibits rotational symmetry in spin space) corrected by this contribution is called

scalar-relativistic approximation [26] (denoted by $\mathcal{H}_{\text{SR}}$). That $\mathcal{H}_{\text{SR}}$ is invariant under a rotation in spin space is expressed by the following equality:

$$U^\dagger \, \mathcal{H}_{\text{SR}} \, U = \mathcal{H}_{\text{SR}} \,, \tag{2.31}$$

where U is a (2×2) spin-rotation matrix. That the term $\boldsymbol{\sigma} \cdot \mathbf{B}_{\text{xc}}$ commutes with the rotation matrix can be seen directly, when one recalls that

$$\mathbf{B}_{\text{xc}} \parallel \mathbf{m} \qquad \text{with} \quad \mathbf{m} = \sum_i^{\text{occ.}} \Psi_i^\dagger \, \boldsymbol{\sigma} \, \Psi_i \,. \tag{2.32}$$

When a rotation is applied to the system, also the wavefunctions have to be rotated $(\Psi_i \rightarrow U \, \Psi_i)$ and thus $\mathbf{B}_{\text{xc}} \propto \sum_i \Psi_i^\dagger \, U^\dagger \boldsymbol{\sigma} U \, \Psi_i$ is rotated as well. Hence the term $\boldsymbol{\sigma} \cdot \mathbf{B}_{\text{xc}}$ is indeed a scalar product and invariant under spin rotations.

The second correction in equation (2.30),

$$\mathcal{H}_{\text{so}} = \frac{1}{c^2} \, \boldsymbol{\sigma} \cdot \left((\nabla V_{\text{eff}}) \times \mathbf{p} \right) , \tag{2.33}$$

is called spin-orbit coupling [27]. In contrast to the previously discussed terms it is not invariant under rotations in spin space and it is largest in the vicinity of the nuclei where the potential gradient is high. In this region, the potential can be well approximated by its spherical average,

$$\nabla V(\mathbf{r}) \approx \sum_\mu \frac{\partial \tilde{V}(r^\mu)}{\partial r^\mu} \frac{\mathbf{r}^\mu}{r^\mu} \,, \tag{2.34}$$

where $\tilde{V}_\mu$ is the spherically averaged potential and $\mathbf{r}^\mu = \mathbf{r} - \mathbf{R}^\mu$ is the real space coordinate with respect to the position of the μth nucleus. Inserting this approximation into equation (2.33) leads to

$$\mathcal{H}_{\text{so}} = \sum_\mu \xi^\mu(r^\mu) \, \boldsymbol{\sigma} \cdot \mathbf{L}^\mu = \sum_\mu \xi^\mu(r^\mu) \begin{pmatrix} L_z^\mu & L_-^\mu \\ L_+^\mu & -L_z^\mu \end{pmatrix} , \tag{2.35}$$

where $\mathbf{L}^\mu$ denotes the angular momentum operator with respect to the μth nucleus, L_z^μ is its z-component, $L_\pm^\mu = L_x^\mu \pm i \, L_y^\mu$ and $\xi^\mu(r^\mu) = \frac{1}{c^2} \frac{1}{r^\mu} \frac{\partial \tilde{V}(r^\mu)}{\partial r^\mu}$ is the spin orbit coupling constant. ξ^μ is usually a fast decaying function of the distance to the nucleus, r^μ, and proportional to the charge of the nucleus Z.

2.7 Bloch Theorem

When one deals with infinite crystal structures, the computation is only made possible by use of Bloch's theorem.

The Hamiltonian (2.2) is invariant under a translation $\mathcal{T}_{\mathbf{R}}$ of a lattice vector $\mathbf{R} = m \, \mathbf{a}_1 + n \, \mathbf{a}_2 + p \, \mathbf{a}_3$, with $m, n, p \in \mathbb{Z}$ and $\mathbf{a}_i$ being the basis vectors of the unit cell. Thus the Hamiltonian $\mathcal{H}$ commutes with $\mathcal{T}_{\mathbf{R}}$,

$$[\mathcal{H}, \mathcal{T}_{\mathbf{R}}] = 0 \,, \tag{2.36}$$

and the a common set of eigenfunctions can be found. These eigenfunctions are called Bloch waves,

$$\psi_{\mathbf{k},\nu}(\mathbf{r}) = \mathrm{e}^{i\mathbf{kr}} \, u_{\mathbf{k},\nu}(\mathbf{r}) \,, \tag{2.37}$$

where the so called Bloch function $u_{\mathbf{k},\nu}$ exhibits the periodicity of the lattice, $u_{\mathbf{k},\nu}(\mathbf{r} + \mathbf{R}) = u_{\mathbf{k},\nu}(\mathbf{r})$, and is also periodic in reciprocal space, $u_{\mathbf{k},\nu} = u_{\mathbf{k}+\mathbf{K},\nu}$, where ν is the band index and $\mathbf{K}$ is a reciprocal lattice vector. This has important consequences for the practical computation of the electronic structure, as only the unit cell and the first Brillouin zone have to be considered in finding the electron density in a crystal structure.

This powerful approach can also be applied to generalized translations (translation in real space plus rotation in spin space), as will be pointed out later (cf. chapter 3.5).

2.8 Force Theorem

Since V_{xc} depends on $n(r)$, the solution of the Kohn-Sham equation to a given Hamiltonian has to be calculated self-consistently. However, if a small perturbation is added to a Hamiltonian for which the self-consistent solution is already known, only one iteration has to be done to obtain an estimate for the change in total energy. This so called force theorem [28–30] reduces the computational effort a lot. It is explained in the following:

The Kohn-Sham equation for a given Hamiltonian $\mathcal{H}_0$,

$$\mathcal{H}_0[n_0] \, \psi_{\nu,0} = \epsilon_{\nu,0} \, \psi_{\nu,0} \,, \tag{2.38}$$

must be solved self-consistently, where n_0 is the corresponding (self-consistent) electron density and $\psi_{\nu,0}$ and $\epsilon_{\nu,0}$ denote the eigenstates and -values, respectively. When a small perturbation $\delta\mathcal{H}$ is added ($\mathcal{H}_1 = \mathcal{H}_0 + \delta\mathcal{H}$), the change in energy can be well approximated by

$$\delta E = \sum_{\nu}^{\mathrm{occ.}} \epsilon_{\nu,1}^{\mathrm{FT}} - \sum_{\nu}^{\mathrm{occ.}} \epsilon_{\nu,0}. \tag{2.39}$$

Here, $\epsilon_{\nu,1}^{\mathrm{FT}}$ are the eigenvalues of the Kohn-Sham equation, where the perturbed Hamiltonian is dependent on the unperturbed electron density,

$$\mathcal{H}_1[n_0] \, \psi_{\nu,1}^{\mathrm{FT}} = \epsilon_{\nu,1}^{\mathrm{FT}} \, \psi_{\nu,1}^{\mathrm{FT}} \,. \tag{2.40}$$

This stands in contrast to the full self-consistent solution, where $\mathcal{H}_1[n_1]$ is taken.

Because the force theorem can be proved without knowing the explicit form of the perturbation, it can be applied to a large number of perturbations. It is based on the fact, that the changes in total energy in first order perturbation theory coincide with the changes in the single particle energies. However, it fails when the changes in the charge density n or magnetization density $\mathbf{m}$ become too big and one has to take terms beyond first order perturbation theory into account, as it is the case for structural relaxations. But changes in the magnetic structure can often be well described by the force theorem.

In this thesis, the force theorem is applied in two cases: when the propagation vector of a spin spiral is changed by a small amount and when spin-orbit coupling is taken into

account. It is also possible to combine both perturbations, as it is done for calculating the Dzyaloshinskii-Moriya interaction in Cr/W(110). Test were made to confirm the validity (cf. chapters 6.4, 7.4.3 and 7.6).

3 The FLAPW-Method

In the previous section it was shown, that the complicated many-body problem can be transferred into a problem of non-interaction electrons where the many-body effects are treated as contributions to an effective potential. One has now to develop a technique to solve the resulting equations on a computer. This is done by transforming the problem of finding the eigenvalues and eigenfunctions of equation (2.10) into a problem of linear algebra, namely diagonalizing a matrix, by the choice of a basis set $\{\varphi_n\}$. Then the wavefunction is expanded in this basis ($\psi = \sum_n c_n \varphi_n$), and the Kohn-Sham equation reads

$$\underline{\mathbf{H}} \cdot \mathbf{c} = \varepsilon \, \underline{\mathbf{S}} \cdot \mathbf{c} \tag{3.1}$$

where the vector $\mathbf{c}$ contains the coefficients for the wavefunction expansion in the chosen basis, $\underline{\mathbf{H}}$ is the Hamiltonian expressed in the basis and $\underline{\mathbf{S}}$ is the overlap matrix of the basisfunctions,

$$\underline{\mathbf{H}}_{n,n'} \;=\; \int \mathrm{d}\mathbf{r}\, \varphi_n^*(\mathbf{r})\, \mathcal{H}\, \varphi_{n'}(\mathbf{r})\,, \tag{3.2}$$

$$\underline{\mathbf{S}}_{n,n'} \;=\; \int \mathrm{d}\mathbf{r}\, \varphi_n^*(\mathbf{r})\, \varphi_{n'}(\mathbf{r})\,. \tag{3.3}$$

In principle any basis set can be taken, but the number of basisfunctions and hence the size of the matrices is infinite, if the basis should be complete. To diagonalize the matrices practically, one takes only a finite number of basisfunctions. It is important to choose a basis set which already exhibits the properties of the underlying system as much as possible, so that a feasible amount of basisfunctions is sufficient to describe the system.

Plane waves seem to be convenient as basis set, because they are orthogonal (and hence the overlap matrix reduces to unity) and they are eigenfunctions of the Laplace operator, which is contained in the Hamiltonian. Let us recall that they are eigenfunctions of the Schrödinger equation for a constant potential, but in this case the potential is far away from being constant. Instead it even has divergences at the nuclei which makes the wavefunction vary rapidly in these regions, and many basisfunctions would have to be considered to describe these variations correctly. The APW-method, which will be described in the following section and further be improved to LAPW and FLAPW, deals with this deficiency of the plane waves.

3.1 The APW basis set and its problems

To circumvent the deficiencies of plane waves, in the *augmented plane wave* (APW) method [31, 32] the space is divided into two regions: into spheres with radius R_{MT}^μ

around atom μ (called *muffin tin*) and the remaining part (called *interstitial region*). Two different kinds of basis set is used in each region. Because the potential in between the atoms is rather smooth, plane waves are used as a basis in the interstitial region. In the muffin tins atomic wavefunctions are used in order to describe the $1/r$-divergence, which consist of radial functions and spherical harmonics,

$$
\varphi_{\mathbf{G}}(\mathbf{k}, \mathbf{r}) = \begin{cases} e^{i(\mathbf{k}+\mathbf{G})\mathbf{r}} & \mathbf{r} \in \text{interstitial region} \\ \sum_L a_L^{\mu \mathbf{G}}(\mathbf{k})\, u_l(r^\mu)\, Y_L(\hat{\mathbf{r}}^\mu) & \mathbf{r} \in \text{muffin-tin sphere } \mu \end{cases} , \qquad (3.4)
$$

where $\mathbf{k}$ is the Bloch vector, $\mathbf{G}$ is a reciprocal lattice vector, L abbreviates the angular quantum numbers l and m, and $\mathbf{r}^\mu = \mathbf{r} - \mathbf{R}^\mu$ denotes the position relative to the center of muffin-tin μ. The radial functions are chosen as solutions of the Schrödinger equation in a spherical symmetric potential,

$$
\left\{ -\frac{\partial^2}{\partial r^2} + \frac{l(l+1)}{r^2} + V(r) - E \right\} r\, u_l(r) = 0 \,, \qquad (3.5)
$$

where $V(r)$ is the spherical symmetric part of the potential $V(\mathbf{r})$ and E is the band energy. The coefficients $a_L^{\mu \mathbf{G}}(\mathbf{k})$ are determined by the condition, that the basisfunctions must be continuous at the muffin-tin sphere boundary. The role of the energy, E, turns out to be very important. If it were only used as a parameter during the construction of the basis, the Kohn-Sham equation can be represented by this basis and the solution gives the eigenstates and band energies. Unfortunately an accurate description of the system can only be achieved if E is the band energy, and thus also the basis is dependent on them. This turns the solution of the Kohn-Sham equation into a nonlinear problem, which is computationally much more demanding than a standard problem. Among some other difficulties this is the reason why the APW basis has been extended to the LAPW, which will be described in the next section.

3.2 The LAPW basis set

The *linearized augmented plane wave* (LAPW) basis set [33, 34] is a modified APW basis set, where E_l is introduced as a parameter replacing E, and it is expanded to gain more variational freedom. By introducing also the energy derivative of u_l, $\dot{u}_l = \partial u_l / \partial E$, the energy parameters do not have to match the band energies and a nonlinear problem is circumvent. This approach can be thought of as a Taylor expansion of u_l around the true band energy E,

$$
u_l(E) = u_l(E_l) + (E - E_l)\, \dot{u}_l(E_l) + O\left((E - E_l)^2\right), \qquad (3.6)
$$

where the error made by the choice of the approximate band energy E_l is partly corrected by the second term. Then the LAPW basisfunctions take the following form:

$$
\varphi_{\mathbf{G}}(\mathbf{k}, \mathbf{r}) = \begin{cases} e^{i(\mathbf{k}+\mathbf{G})\mathbf{r}} & \mathbf{r} \in \text{IR} \\ \sum_L \left(A_L^{\mu \mathbf{G}}(\mathbf{k})\, u_l(r^\mu) + B_L^{\mu \mathbf{G}}(\mathbf{k})\, \dot{u}_l(r^\mu) \right) Y_L(\hat{\mathbf{r}}^\mu) & \mathbf{r} \in \text{MT } \mu \end{cases} , \qquad (3.7)
$$

where the coefficients are called *muffin-tin A- and B-coefficients* and are determined by the condition, that the basisfunctions and their first derivatives must be continuous at the muffin-tin boundary. Differentiation of equation (3.5) yields

$$\left\{ -\frac{\partial^2}{\partial r^2} + \frac{l(l+1)}{r^2} + V(r) - E_l \right\} r\, \dot{u}_l(r) = r\, u_l(r) \,, \tag{3.8}$$

and the solution of this equation gives $\dot{u}_l$. From the derivative of the normalization condition of the radial function u_l it can be easily shown that u_l and $\dot{u}_l$ are orthogonal. However, the whole LAPW basis set is not orthogonal and this has to be taken into account when diagonalizing the Hamiltonian matrix. But they form a good basis in the sense that a relatively small number of basisfunctions is sufficient to describe the Hamiltonian.

Please note that during each self-consistency cycle the basis has to be reconstructed because the density (and thus also the potential $V(r)$ in equation (3.5)) changes.

3.2.1 The LAPW basis for film geometries

The LAPWs as described in the previous section form a good basis for potentials which are periodic in three dimensions such as bulk systems. If one wants to describe surfaces or interfaces, one can in principle work with the normal LAPW basis set, but has to use huge super cells and thus many basisfunctions in order make the interaction of the surface with its periodically repeated images small enough. Of course this approach is computationally very ineffective and a modified LAPW basis [35] is used instead. Here one has an infinite, periodic system in two dimensions that is non-periodic in the third dimension. The surface is chosen to be perpendicular to the z-direction. Additionally to the muffin tins and the interstitial region, two *vacuum regions* are introduced in the regions $|z| > D/2$. Of course, now the Bloch theorem applies only in the two dimensional periodic subspace and the wavefunctions can be written as

$$\psi_{\mathbf{k}_\parallel}(\mathbf{r}) = e^{i\mathbf{k}_\parallel \cdot \mathbf{r}_\parallel} \sum_{\mathbf{G}_\parallel} c_{\mathbf{k}_\parallel, \mathbf{G}_\parallel}(z)\, e^{i\mathbf{G}_\parallel \cdot \mathbf{r}_\parallel} \,, \tag{3.9}$$

where $\cdot_\parallel$ and $\cdot_z$ denote the component parallel and normal to the surface, respectively. $\mathbf{G}_\parallel$ denotes the reciprocal lattice vectors of the two-dimensional unit cell. The functions $c_{\mathbf{k}_\parallel, \mathbf{G}_\parallel}(z)$ are non-periodic in z, but in the interstitial region, $|z| < D/2$, they are expanded to plane waves as well. The wave vectors are defined as $G_z = \frac{2\pi n}{\tilde{D}}$, where $\tilde{D}$ is chosen a bit larger than D in order to make sure that the basisfunctions keep their full variational freedom: If $\tilde{D} = D$ was chosen, all plane waves would have $c_{\mathbf{k}_\parallel, \mathbf{G}_\parallel}(\pm D/2) = \pm 1$ at the interstitial/vacuum boundary. In the vacuum region, $c_{\mathbf{k}_\parallel, \mathbf{G}_\parallel}(z)$ are functions that are solutions of a 1-dimensional Schrödinger equation with the potential in the vacuum,

$$\left\{ \left(\mathbf{G}_\parallel + \mathbf{k}_\parallel\right)^2 - \frac{\partial^2}{\partial z^2} + V_{\text{vac}}(z) - E_{\text{vac}} \right\} v_{\mathbf{G}_\parallel}(\mathbf{k}_\parallel, z) = 0 \,, \tag{3.10}$$

where E_{vac} is the vacuum energy parameter and the potential $V_{\text{vac}}(z)$ is constructed by averaging $V_{\text{eff}}(\mathbf{r})$ over x and y. In analogy to the construction of the radial functions

inside the muffin tins, also the energy derivative $\dot{v}_{\mathbf{G}_\parallel}$ are included in the basisfunctions, so that they finally take the following form ($\mathbf{K} = \mathbf{G} + \mathbf{k}$):

$$\phi_{\mathbf{K}}(\mathbf{r}) = \begin{cases} e^{i\mathbf{K}\cdot\mathbf{r}} & \mathbf{r} \in \text{interstitial} \\ \sum_L \left(A_L^{\mu\mathbf{K}}\, u_l(r^\mu) \right. & \mathbf{r} \in \text{MT } \mu \\ \qquad \left. + B_L^{\mu\mathbf{K}}\, \dot{u}_l(r^\mu) \right) Y_L(\hat{\mathbf{r}}^\mu) & \\ e^{i\mathbf{K}_\parallel \cdot \mathbf{r}_\parallel} \left(A_{\text{vac}}^{\eta\mathbf{K}_\parallel} v_{\mathbf{K}_\parallel}(z) \right. & \mathbf{r} \in \text{vacuum } \eta \\ \qquad \left. + B_{\text{vac}}^{\eta\mathbf{K}_\parallel} \dot{v}_{\mathbf{K}_\parallel}(z) \right) & \end{cases} . \qquad (3.11)$$

The *vacuum A- and B-coefficients* are determined in the same way as the coefficients of the muffin tin, namely by requiring that the basisfunctions and their first derivatives are continuous at the vacuum/interstitial boundary. $\eta = 1, 2$ labels the vacuum region above and below the film, respectively.

3.3 Shape approximations in the (L)APW method and extension to FLAPW

So far only the basis to represent the wavefunctions was described. But in both methods (APW and LAPW), usually also shape approximations to the potential are applied. The potential in the interstitial is often set to a constant value and in the muffin tins the potential is approximated by its spherically symmetric average (in the APW method this is even mandatory). However, these approximations lead to problems when open structures – such as surfaces, interfaces or 1-dimensional structures – are under consideration. Then one has to go beyond these approximations, which is done in the *full-potential linearized augmented plane wave* (FLAPW) method [11,12]. Here, the potential in the interstitial is expressed in terms of plane waves (they are expanded up to a wave-vector g_{max} and $g_{\text{max,xc}}$ for the potential and exchange-correlation potential, respectively). In the muffin-tin radii a logarithmic radial mesh is introduced and rV is expanded in spherical harmonics $Y_{\ell,m}$ for each mesh point r up to $\ell = \ell_{\text{max}}$. In the vacuum regions, an equidistant grid in the direction normal to the surface is introduced and in the planes going through the grid points, 2-dimensional plane waves are used to expand the potential inside the pane. The expansion is cut off at a finite distance from the film surface.

3.4 Magnetic calculations

Recall the Kohn-Sham equation for the magnetic case,

$$\begin{pmatrix} \mathcal{H}\mathbb{1} + B_{\text{xc}}\frac{m_z}{|\mathbf{m}|} & B_{\text{xc}}\frac{m_x - im_y}{|\mathbf{m}|} \\ B_{\text{xc}}\frac{m_x + im_y}{|\mathbf{m}|} & \mathcal{H}\mathbb{1} - B_{\text{xc}}\frac{m_z}{|\mathbf{m}|} \end{pmatrix} \begin{pmatrix} \psi_\nu^\uparrow \\ \psi_\nu^\downarrow \end{pmatrix} = \epsilon_\nu \begin{pmatrix} \psi_\nu^\uparrow \\ \psi_\nu^\downarrow \end{pmatrix}, \qquad (3.12)$$

where the abbreviation $\mathcal{H}\mathbb{1} = \mathbf{p}^2 + V_{\text{eff}}$ has been used, and an external magnetic field has been neglected.

When magnetic calculations are done within FLAPW, it is useful to distinguish between collinear and non-collinear configurations:

- Let's discuss collinear configurations first: As long as we neglect spin-orbit coupling, the orientation of the spin coordinate-system (describing the vector $\mathbf{m}$) does not depend on the real-space orientation. Thus, for a collinear calculation, we can choose $\mathbf{m}(\mathbf{r}) = m(\mathbf{r})\hat{\mathbf{e}}_z$. Then the two components of the spinor are decoupled in the Kohn-Sham Hamiltonian and the problem is similar to the non-magnetic case with two different potentials $V^{\uparrow} = V_{\text{eff}} + B_{\text{xc}}$ and $V^{\downarrow} = V_{\text{eff}} - B_{\text{xc}}$. In this case, the solution of the secular equation is straight forward and the implementation is rather simple: For the spin-up and spin-down components two different basis are constructed using also two independent sets of energy parameters for the construction of the muffin tin and vacuum basisfunctions. The up- and down-components only couple to each other in the self-consistent cycle via the exchange-correlation potential. The computation time is twice as large as in the non-magnetic case.

- In the case of non-collinear spin configurations [36], the magnetization is represented by a field of 3-dimensional vectors $\mathbf{m}(\mathbf{r})$ and we cannot choose a global quantization axis. However, the code that we apply [13] restricts the magnetization direction inside the muffin-tin spheres

$$\mathbf{m}(\mathbf{r}) = \begin{cases} \mathbf{m}(\mathbf{r}) & \text{interstitial and vacuum,} \\ m^{\mu}(\mathbf{r})\,\hat{\mathbf{e}}^{\mu} & \text{muffin-tin sphere } \mu, \end{cases} \tag{3.13}$$

where the direction $\hat{\mathbf{e}}^{\mu}$ is described by two angles α^{μ} and β^{μ}. Then a local coordinate system for each muffin-tin is introduced such, that the local $\hat{z}$-axis points parallel to $\hat{\mathbf{e}}^{\mu}$. Let the $\tilde{}$ denote quantities in the local coordinate frame, then a spin rotation matrix $\mathbf{U}_{\text{MT}\,\mu}$ connects the local and global coordinate frame. The potential then reads

$$\tilde{V} = \mathbf{U}^{\dagger}_{\text{MT}\,\mu} V\, \mathbf{U}_{\text{MT}\,\mu} = (V_{\text{H}} + V_{\text{ext}})\mathbb{1} + \begin{pmatrix} \tilde{V}_{\text{xc}}^{\uparrow\uparrow} & \tilde{V}_{\text{xc}}^{\uparrow\downarrow} \\ \tilde{V}_{\text{xc}}^{\downarrow\uparrow} & \tilde{V}_{\text{xc}}^{\downarrow\downarrow} \end{pmatrix}. \tag{3.14}$$

After one self-consistency cycle, the magnetization can in principle point into any direction. However, if the deviations from the chosen local coordinate frame are small ($\tilde{\mathbf{m}}_x \approx \tilde{\mathbf{m}}_y \approx 0$), it is sufficient to consider only $\tilde{\mathbf{m}}_z$ in the construction of the exchange-correlation potential for the next self-consistency cycle and the exchange-correlation potential inside the muffin-tin sphere, $\tilde{V}_{\text{xc}}$, is diagonal. However, the potential in the global coordinate frame, V_{xc}, has off-diagonal components and the two components of the spinor are not decoupled.

The basis for non-collinear magnetization directions is modified: The radial functions u_l and $\dot{u}_l$ are constructed in the local coordinate frame. The basisfunctions in the interstitial region are constructed in the global frame of reference and have the form

$$\phi_{\mathbf{K}}^{\uparrow}(\mathbf{r}) = \begin{pmatrix} \exp(i\mathbf{K} \cdot \mathbf{r}) \\ 0 \end{pmatrix} \qquad \phi_{\mathbf{K}}^{\downarrow}(\mathbf{r}) = \begin{pmatrix} 0 \\ \exp(i\mathbf{K} \cdot \mathbf{r}) \end{pmatrix}. \tag{3.15}$$

Please notice that both local spin components of the basisfunctions inside the muffin tin have to be matched to the interstitial wavefunction at the muffin-tin/interstitial boundary.

If the magnetization of the muffin tins deviates much from the defined local $\hat{z}$-axis, one has either to relax the direction of the local coordinate frame or to perform a constrained calculation [36, 37].

  – In the former case, the direction of the muffin tin is adapted to the magnetization direction after each self-consistency cycle (which usually converges very slowly).

  – In the latter case, the energy functional is minimized under the constraint, that the magnetization of the muffin tin points into the direction defined by α and β. The Lagrange parameters corresponding to the constraint have the form of a muffin-tin dependent magnetic field (the so called constraining field).

However, in many systems the local x- and y-component of the magnetization is small compared to its z-component, so that a calculation neglecting these (as it is done in this thesis) leads to the same result.

3.5 Spin spirals and the generalized Bloch theorem

Spin spirals are magnetic structures where the magnetization is rotated by a constant angle from one unit cell to the next along a certain direction of the crystal. In absence of spin-orbit coupling, the rotation axis can be defined as global $\hat{z}$-axis without loss of generality. The magnetization direction then reads

$$\hat{e}^{n,\mu} = \begin{pmatrix} \cos(\mathbf{q} \cdot (\mathbf{R}^n + \boldsymbol{\tau}^\mu) + \alpha^\mu) \sin\theta^\mu \\ \sin(\mathbf{q} \cdot (\mathbf{R}^n + \boldsymbol{\tau}^\mu) + \alpha^\mu) \sin\theta^\mu \\ \cos\theta^\mu \end{pmatrix}, \qquad (3.16)$$

where $\mathbf{R}^n$ is the lattice vector pointing from the origin to unit cell n, $\boldsymbol{\tau}^\mu$ is the basis vector of atom μ in the unit cell, $\mathbf{q}$ is the so called spin-spiral vector, θ^μ is the cone angle between the magnetic moment of atom μ and the rotation axis, and α^μ is an atom-dependent phase shift. Four examples are shown in figure 3.1.

Employing the generalized Bloch theorem [38–40], spin spirals can be computed without the usage of super cells in which the magnetic structure is commensurate (these become very large for small q-vectors). This allows calculations in the chemical unit cell and can be proved only if SOC is neglected. A generalized translation $\mathcal{T}_n$, which combines a lattice translation with a rotation in spin space, commutes with the Hamiltonian in scalar-relativistic approximation,

$$[\mathcal{T}_n, \mathcal{H}] = 0. \qquad (3.17)$$

In analogy to the Bloch theorem, this allows us to decompose each component of the spinor wavefunction into a (q-dependent) Bloch factor and a (lattice periodic) Bloch
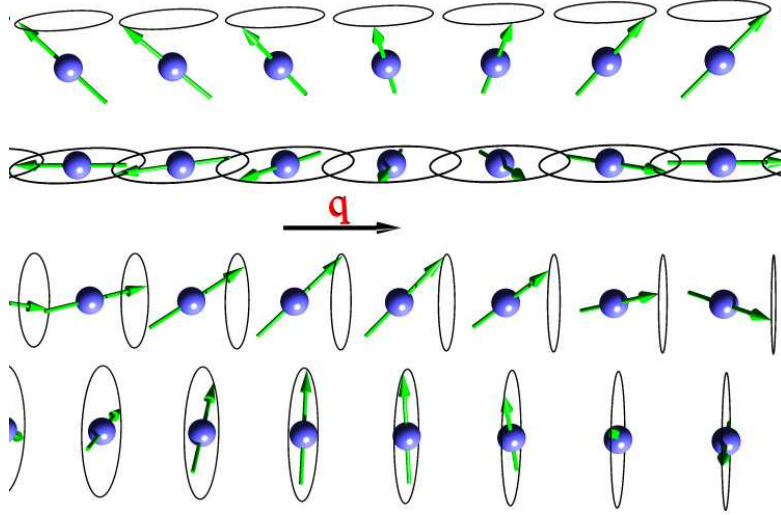
Figure 3.1: Four examples of spin spirals with spin rotation-axis perpendicular (upper two) and parallel (lower two) to the spin-spiral vector $\mathbf{q}$. For each case two spirals with cone angles of $\theta = \pi/2$ and $\theta = \pi/4$ are shown. In the absence of spin-orbit coupling, spirals 1 and 3 (counted from the top), and 2 and 4, respectively, are equivalent, because real space and spin space are decoupled.

function $u_{\mathbf{k}}^{\sigma}(\mathbf{r}) = u_{\mathbf{k}}^{\sigma}(\mathbf{r} + \mathbf{R}^n)$:

$$\Psi_{\mathbf{k}}(\mathbf{r}) = \begin{pmatrix} e^{i(\mathbf{k}-\mathbf{q}/2)\cdot\mathbf{r}} \, u_{\mathbf{k}}^{\uparrow}(\mathbf{r}) \\ e^{i(\mathbf{k}+\mathbf{q}/2)\cdot\mathbf{r}} \, u_{\mathbf{k}}^{\downarrow}(\mathbf{r}) \end{pmatrix} . \tag{3.18}$$

The Bloch factor consists of a real-space translation $e^{i\mathbf{k}\cdot\mathbf{r}}$ and a spin rotation around the $\hat{z}$-axis $\begin{pmatrix} e^{-i\mathbf{q}\cdot\mathbf{r}/2} & 0 \\ 0 & e^{i\mathbf{q}\cdot\mathbf{r}/2} \end{pmatrix}$.

3.6 Spin-orbit coupling

Spin-orbit coupling, as described in section 2.6, is implemented in the FLAPW-method as follows [41]: SOC is only treated in the muffin tins and it is neglected in the interstitial and vacuum regions. This approximation leads to the equation (cf. equation (2.35))

$$\mathcal{H}_{\text{so}} = \sum_{\mu} \Theta^{\mu}(\mathbf{r}^{\mu}) \, \xi^{\mu}(r^{\mu}) \, \boldsymbol{\sigma} \cdot \hat{\mathbf{L}}^{\mu} \ \ \text{with} \ \Theta^{\mu}(\mathbf{r}^{\mu}) = \begin{cases} 1 & \text{if } |\mathbf{r}^{\mu}| < R_{\text{MT}}^{\mu} \\ 0 & \text{else} \end{cases} , \tag{3.19}$$

where $\mathbf{r}^{\mu} = \mathbf{r} - \mathbf{R}^{\mu}$, and $\mathbf{R}^{\mu}$ and R_{MT}^{μ} are the center and the radius of the muffin-tin sphere μ.

We can rewrite the spin-orbit coupling operator in each muffin tin by dropping the

sum and atom index μ as

$$\mathcal{H}_{\text{so}} = \xi(r) \begin{pmatrix} +\hat{L}_z & \hat{L}_- \\ \hat{L}_+ & -\hat{L}_z \end{pmatrix} , \quad \hat{L}_\pm = \hat{L}_x \pm i\,\hat{L}_y \tag{3.20}$$

If the $\hat{z}$-axis is not the spin-quantization axis, a rotation $\mathbf{U}_{\text{rs}}$ has to be performed to rotate the global spin coordinate frame with respect to the lattice. This can be done by rotating the SOC operator,

$$\mathbf{U}_{\text{rs}}^\dagger\, \mathcal{H}_{\text{so}}\, \mathbf{U}_{\text{rs}} = \xi(r)\, \mathbf{U}_{\text{rs}}^\dagger (\boldsymbol{\sigma} \cdot \hat{\mathbf{L}}) \mathbf{U}_{\text{rs}} = \xi(r) \begin{pmatrix} \hat{L}^{(\uparrow,\uparrow)} & \hat{L}^{(\uparrow,\downarrow)} \\ \hat{L}^{(\downarrow,\uparrow)} & \hat{L}^{(\downarrow,\downarrow)} \end{pmatrix} . \tag{3.21}$$

How this correction is added to the scalar-relativistic Hamiltonian depends on the system one wants to study (e.g. spin-spiral systems) and the quantity one is interested in (e.g. Dzyaloshinskii-Moriya interaction (DMI) or magnetocrystalline anisotropy (MCA)). The different approaches can be roughly divided into self-consistent ones (SC) or the ones employing the force theorem:

1. Self consistent in nearly collinear structures (employing a scheme called "second variation")

2. Self consistent in noncollinear structures

3. Force theorem employing exact diagonalization of $\mathcal{H}_{\text{so}}$

4. Force theorem and treating $\mathcal{H}_{\text{so}}$ as a perturbation.

In this thesis, the MCA will be calculated in second variation (because it can be obtained from collinear magnetization directions), and the DMI will be calculated in first order perturbation theory (as it allows the treatment of spin spirals without the use of a supercell, in which the magnetization is commensurate). We will discuss these approaches in more detail in the subsequent sections.

3.6.1 Second variation in nearly collinear structures

Most magnetic systems exhibit a collinear magnetization when SOC is neglected. Therefore, in this scheme first a collinear calculation neglecting SOC is done and the eigenfunctions $\psi_i^\uparrow$ for the spin-up and $\psi_i^\downarrow$ for the spin-down component are obtained. Afterwards, these functions are used as basis to set up the full Hamiltonian (i.e. where $\mathcal{H}_{\text{so}}$ was added to the problem) and obtain the eigenfunctions φ_ν and eigenenergies by diagonalization. Here, $\mathcal{H}_{\text{so}}$ mixes up- and down-components of the unperturbed solution into the wavefunctions φ_ν via its off-diagonal elements. However, because SOC is a small perturbation and thus the elements of $\mathcal{H}_{\text{so}}$ are small compared to the scalar-relativistic Hamiltonian, φ_ν mainly consists of one component of ψ_i^σ and the other is much smaller in magnitude and the magnetization of the perturbed problem is nearly collinear. Therefore, this scheme makes sense in a self-consistent treatment of SOC only if the ground state neglecting SOC is (nearly) collinear.

This procedure is approximately 4 times faster than using the LAPW basis to set up the whole Hamiltonian (including SOC), because the unperturbed eigenfunctions ψ_i^σ already describe the perturbed system quite well and only relatively few (compared to LAPWs) are needed to to form a good basis.

3.6.2 First-order perturbation theory

Because spin-orbit coupling is a small correction compared to the rest of the Hamiltonian, we can treat it as a perturbation. First-order perturbation theory is an easy way to approximate effects that are linear in the spin-orbit coupling parameter ξ. Thus, the strength of the Dzyaloshinskii-Moriya interaction (in spin-spiral calculations) can be approximated by the expectation values

$$\Delta E_j = \langle \psi_j \, |\mathcal{H}_{\mathrm{so}}| \, \psi_j \rangle = \left(\langle \psi_j^{(\uparrow)}|, \, \langle \psi_j^{(\downarrow)}| \right) \begin{pmatrix} \mathcal{H}_{\mathrm{so}}^{(\uparrow,\uparrow)} & \mathcal{H}_{\mathrm{so}}^{(\uparrow,\downarrow)} \\ \mathcal{H}_{\mathrm{so}}^{(\downarrow,\uparrow)} & \mathcal{H}_{\mathrm{so}}^{(\downarrow,\downarrow)} \end{pmatrix} \begin{pmatrix} |\psi_j^{(\uparrow)}\rangle \\ |\psi_j^{(\downarrow)}\rangle \end{pmatrix}, \qquad (3.22)$$

where $|\psi_j\rangle$ is an eigenstate to the unperturbed problem.

First-order perturbation theory is very convenient for spin-spiral calculations with small q-vectors [14]. The atoms of a spin spiral are not equivalent under a generalized translation if SOC is taken into account, because the atoms can be distinguished by their spin-orbit contribution. However, in first order perturbation theory, the correction to the band energies is the same for all atoms, as can be seen as follows:

All 4 components $\mathcal{H}_{\mathrm{so}}^{(\sigma,\sigma')}$ of the spin-orbit operator are lattice periodic. A lattice periodic operator applied to a Bloch wave gives the same Bloch factor and another (lattice periodic) Bloch function $v(\mathbf{r})$, which leads in our case to the equation

$$\mathcal{H}_{\mathrm{so}}^{(\sigma,\sigma')} \underbrace{\mathrm{e}^{i\,(\mathbf{k}\mp\mathbf{q}/2)\cdot\mathbf{r}}\, u_j^{(\sigma')}(\mathbf{r})}_{\psi_j^{\sigma'}(\mathbf{r})} = \mathrm{e}^{i\,(\mathbf{k}\mp\mathbf{q}/2)\cdot\mathbf{r}}\, v_j^{(\sigma')}(\mathbf{r}), \qquad (3.23)$$

where the $-$ ($+$) corresponds to $\sigma' = \uparrow$ ($\downarrow$). The integrals over the off-diagonal elements of $\mathcal{H}_{\mathrm{so}}$, e.g. $\langle \psi_j^{(\uparrow)}|\mathcal{H}_{\mathrm{so}}^{(\uparrow,\downarrow)}|\psi_j^{(\downarrow)}\rangle$, summing over N chemical unit cells so that the magnetization in this supercell is commensurate, vanish:

$$\underbrace{\sum_{n=1}^{N} e^{i\,\mathbf{q}\cdot n\mathbf{R}}}_{=0} \int_{\mathrm{MT}} \mathrm{d}\mathbf{r}\, e^{i\,\mathbf{q}\cdot\mathbf{r}}\, u_j^{(\uparrow)}(\mathbf{r})^*\, v_j^{(\downarrow)}(\mathbf{r}) = 0, \quad \mathbf{q}\cdot\mathbf{R} = 2\pi/N \text{ and } \mathbf{q} \parallel \mathbf{R}. \qquad (3.24)$$

Therefore, we only have to consider the diagonal elements and can write

$$\langle \psi_j \, |\mathcal{H}_{\mathrm{so}}| \, \psi_j \rangle = N \left(\langle u_j^{(\uparrow)}|v_j^{(\uparrow)}\rangle + \langle u_j^{(\downarrow)}|v_j^{(\downarrow)}\rangle \right), \qquad (3.25)$$

where the Bloch factors canceled each other yielding to the same contribution for each atom of the magnetic supercell. The resulting expression is lattice periodic and thus considering only the chemical unit cell is sufficient.

How the expectation values (3.25) are calculated is presented in the following: The wavefunctions are expressed in the LAPW basis,

$$
\phi_{\mathbf{K}_j}^{(\tilde{\sigma})}(\mathbf{r}) = \sum_L \left(A_L^{\mu\mathbf{K}_j,(\tilde{\sigma})} u_\ell^{(\tilde{\sigma})}(r^\mu) + B_L^{\mu\mathbf{K}_j,(\tilde{\sigma})} \dot{u}_\ell^{(\tilde{\sigma})}(r^\mu) \right) Y_L(\hat{\mathbf{r}}^\mu),
\tag{3.26}
$$

where L abbreviates the quantum numbers ℓ and m, and $\mathbf{K}_j = \mathbf{G} + \mathbf{k}_j$. They are constructed in the local (muffin-tin dependent) coordinate frame (denoted by a $\tilde{\cdot}$). The wavefunctions are expanded in this basis,

$$
\tilde{\psi}_j(\mathbf{r}) = \sum_{\mathbf{G}} \begin{pmatrix} c_{j,\mathbf{G}}^{(\tilde{\uparrow})} \phi_{\mathbf{K}_j}^{(\tilde{\uparrow})} \\ c_{j,\mathbf{G}}^{(\tilde{\downarrow})} \phi_{\mathbf{K}_j}^{(\tilde{\downarrow})} \end{pmatrix}, \qquad j = (\mathbf{k}_j, \nu_j).
\tag{3.27}
$$

When we rotate the wavefunctions from the local to the global reference frame, the rotated muffin-tin A- and B-coefficients read

$$
a_{j,\ell,m}^{(\sigma',\tilde{\sigma})} = \mathbf{U}_{\mathrm{MT}}^{(\sigma',\tilde{\sigma})} \sum_{\mathbf{G}} c_{j,\mathbf{G}}^{(\tilde{\sigma})} A_{\mathbf{k},\mathbf{G},\ell,m}^{(\tilde{\sigma})}
\tag{3.28}
$$

$$
b_{j,\ell,m}^{(\sigma',\tilde{\sigma})} = \mathbf{U}_{\mathrm{MT}}^{(\sigma',\tilde{\sigma})} \sum_{\mathbf{G}} c_{j,\mathbf{G}}^{(\tilde{\sigma})} B_{\mathbf{k},\mathbf{G},\ell,m}^{(\tilde{\sigma})}
\tag{3.29}
$$

The searched for expectation value reads

$$
\left\langle \psi_{j'} \left| \mathbf{U}_{\mathrm{rs}}^\dagger \mathcal{H}_{\mathrm{so}} \mathbf{U}_{\mathrm{rs}} \right| \psi_j \right\rangle = \int_{\mathrm{MT}} \mathrm{d}\mathbf{r}\, \psi_{j'}^\dagger(\mathbf{r}) \mathbf{U}_{\mathrm{rs}}^\dagger \mathcal{H}_{\mathrm{so}} \mathbf{U}_{\mathrm{rs}} \psi_j(\mathbf{r}),
\tag{3.30}
$$

which can be evaluated using the following abbreviations (cf. (3.21)):

$$
\begin{aligned}
\mathcal{A}_{\ell,m',m}^{(\sigma',\sigma)} &= \int_0^\pi \mathrm{d}\vartheta \int_0^{2\pi} \mathrm{d}\varphi\, (-\sin\vartheta)\, Y_{\ell,m'}(\vartheta,\varphi)^* L^{(\sigma',\sigma)} Y_{\ell,m}(\vartheta,\varphi), \\
\mathcal{R}_{\ell,\dot{u},u}^{(\tilde{\sigma}',\tilde{\sigma})} &= \int_0^{R_{\mathrm{MT}}} \mathrm{d}r\, r^2\, \xi(r) \dot{u}_\ell^{(\tilde{\sigma}')}(r)\, u_\ell^{(\tilde{\sigma})}(r),
\end{aligned}
$$

and analogous expressions for $\mathcal{R}_{\ell,u,u}$, $\mathcal{R}_{\ell,u,\dot{u}}$ and $\mathcal{R}_{\ell,\dot{u},\dot{u}}$. We use another abbreviation,

$$
\begin{aligned}
\mathcal{I}^{(\sigma',\sigma)} &= \sum_{\tilde{\sigma}',\tilde{\sigma}} \sum_{\ell,m',m} \mathcal{A}_{\ell,m',m}^{(\sigma',\sigma)} \left(a_{j',\ell,m'}^{(\sigma',\tilde{\sigma}')*} a_{j,\ell,m}^{(\sigma,\tilde{\sigma})} \mathcal{R}_{\ell,u,u}^{\tilde{\sigma}',\tilde{\sigma}} + a_{j',\ell,m'}^{(\sigma',\tilde{\sigma}')*} b_{j,\ell,m}^{(\sigma,\tilde{\sigma})} \mathcal{R}_{\ell,u,\dot{u}}^{\tilde{\sigma}',\tilde{\sigma}} \right. \\
&\qquad\qquad\qquad \left. + b_{j',\ell,m'}^{(\sigma',\tilde{\sigma}')*} a_{j,\ell,m}^{(\sigma,\tilde{\sigma})} \mathcal{R}_{\ell,\dot{u},u}^{\tilde{\sigma}',\tilde{\sigma}} + b_{j',\ell,m'}^{(\sigma',\tilde{\sigma}')*} b_{j,\ell,m}^{(\sigma,\tilde{\sigma})} \mathcal{R}_{\ell,\dot{u},\dot{u}}^{\tilde{\sigma}',\tilde{\sigma}} \right)
\end{aligned}
$$

to finally rewrite the expectation value

$$
\Delta E_j = \left\langle \psi_j \left| \mathbf{U}_{\mathrm{rs}}^\dagger \mathcal{H}_{\mathrm{so}} \mathbf{U}_{\mathrm{rs}} \right| \psi_j \right\rangle = \mathcal{I}^{(\uparrow,\uparrow)} + \mathcal{I}^{(\downarrow,\downarrow)}.
\tag{3.31}
$$

4 Magnetic interactions

The properties of magnetic materials are often described by model Hamiltonians, where it is assumed that each atom exhibits a (constant) magnetization. The magnetization direction of an atom j is described by a classical unit vector $\mathbf{S}_j$ (with $|\mathbf{S}_j| = 1$). Instead of the magnetization one often uses the term 'spin', which is the magnetization of an atom divided by Bohr's magneton μ_{B}. The energy of the arrangement of several spins is determined by interactions between these. The physical origin of these interactions lies in the (coulomb-)interaction of electrons whose wavefunctions overlap with electron wavefunctions from the neighboring atoms. Continuing this simple picture, the magnetic moment of an atom is then generated by localized electrons. Of course, in reality a rigorous separation cannot be made and it should be seen as a motivation to consider model Hamiltonians with the restrictions described above.

A general bi-linear interaction between two spins can be written as

$$\mathbf{S}_i^{\mathrm{T}} \, \underline{\mathbf{V}}_{ij} \mathbf{S}_j \qquad \text{with} \qquad \underline{\mathbf{V}}_{ij} = \begin{pmatrix} V_{11}^{ij} & V_{12}^{ij} & V_{13}^{ij} \\ V_{21}^{ij} & V_{22}^{ij} & V_{23}^{ij} \\ V_{31}^{ij} & V_{32}^{ij} & V_{33}^{ij} \end{pmatrix} \tag{4.1}$$

where $\underline{\mathbf{V}}_{ij}$ is a real 3×3 matrix and their elements are dependent on the sites of spins i and j. The Hamiltonian of a system of spins consists of all pair-interactions and can be written as

$$H = \sum_{i,j} \mathbf{S}_i^{\mathrm{T}} \, \underline{\mathbf{V}}_{ij} \mathbf{S}_j \, . \tag{4.2}$$

It is very fruitful to divide the interaction-matrix into three parts: an isotropic part, J_{ij}, a symmetric traceless part, $\underline{\mathbf{V}}_{ij}^+$, and an antisymmetric part, $\underline{\mathbf{V}}_{ij}^-$:

$$J_{ij} = \mathrm{Tr}(\underline{\mathbf{V}}_{ij})/3, \tag{4.3}$$

$$\underline{V}_{ij}^+ = (\underline{\mathbf{V}}_{ij} + \underline{\mathbf{V}}_{ij}^{\mathrm{T}})/2 - J_{ij}, \tag{4.4}$$

$$\underline{V}_{ij}^- = (\underline{\mathbf{V}}_{ij} - \underline{\mathbf{V}}_{ij}^{\mathrm{T}})/2. \tag{4.5}$$

Employing these equations we can rewrite the Hamiltonian (4.2) as

$$H = \sum_{i,j} \left(J_{ij} \mathbf{S}_i \cdot \mathbf{S}_j + \mathbf{S}_i^{\mathrm{T}} \, \underline{\mathbf{V}}_{ij}^+ \mathbf{S}_j + \mathbf{S}_i^{\mathrm{T}} \, \underline{\mathbf{V}}_{ij}^- \mathbf{S}_j \right), \tag{4.6}$$

where one identifies the first (isotropic) part to be the Heisenberg model, which will be discussed in more detail in section 4.1.

Because any antisymmetric (3×3)-matrix can be expressed by a vector quantity

$$\left(\underline{\mathbf{V}}_{ij}^{-}\right)_{m,n} = \sum_{l=1}^{3} D_l^{ij}\, \varepsilon_{lmn}, \tag{4.7}$$

where ε_{lmn} is the Levi-Civita symbol, the antisymmetric part of equation (4.6) reads

$$\mathbf{S}_i^{\mathrm{T}}\, \underline{\mathbf{V}}_{ij}^{-} \mathbf{S}_j = \mathbf{D}_{ij} \cdot (\mathbf{S}_i \times \mathbf{S}_j) \ . \tag{4.8}$$

This so called Dzyaloshinskii-Moriya interaction, which is determined by the Dzyaloshinskii-Vector $\mathbf{D}_{ij}$, shall be discussed in more detail in section 4.2.

The third part of the interaction, the symmetric traceless part $\underline{\mathbf{V}}_{ij}^{+}$, is called "pseudo-dipolar interaction" or "anisotropic exchange" [42]. It is of minor importance, because it is a relativistic two-particle effect and its energy contribution is very small. On the other hand it is also computationally very demanding to resolve this kind of exchange and thus it will be neglected in this thesis. In contrast to this, the magnetocrystalline anisotropy energy (MCA), which is the on-site term of $\underline{\mathbf{V}}_{ij}^{+} = \underline{\mathbf{V}}_{ii}^{+}$,

$$H_{\mathrm{ani}} = \sum_i \mathbf{S}_i^{\mathrm{T}}\, \underline{\mathbf{K}}_i \mathbf{S}_i \,, \tag{4.9}$$

where $\underline{\mathbf{K}}$ is the lattice-dependent anisotropy tensor, is important. It will be further investigated in section 4.3.

The whole energy is descibed by the equation

$$H = \sum_{i<j} \left(J_{|i-j|}\, \mathbf{S}_i \cdot \mathbf{S}_j + \mathbf{D}_{i-j}\, (\mathbf{S}_i \times \mathbf{S}_j) \right) + \sum_i \mathbf{S}_i^{\mathrm{T}}\, \underline{\mathbf{K}}_i\, \mathbf{S}_i \,. \tag{4.10}$$

4.1 Heisenberg Model

The Heisenberg model

$$H = \sum_{i,j} J_{ij}\, \mathbf{S}_i \cdot \mathbf{S}_j = \sum_{i,j} J_{ij} \cos(\varphi_{ij}) \tag{4.11}$$

is the simplest model to describe magnetic interactions. In an insulator the so called exchange integral J_{ij} is mainly determined by the overlap of the wavefunctions of atom i and j, and thus it deceases very fast with increasing distance $\mathbf{R}_{ij}$ of the two atoms, but in metals this can show a long-ranged, oscillatory behavior. The ground state of the Heisenberg model is a spin spiral, where the magnetization $\mathbf{M}(\mathbf{R}_i)$ reads

$$\mathbf{M}(\mathbf{R}_i) = M_0 \begin{pmatrix} \cos(\mathbf{q} \cdot \mathbf{R}_i)\, \sin(\theta) \\ \sin(\mathbf{q} \cdot \mathbf{R}_i)\, \sin(\theta) \\ \cos(\theta) \end{pmatrix} \,, \tag{4.12}$$

where $\mathbf{q}$ is the spin-spiral vector, θ is the cone angle and the $\hat{z}$ was chosen as rotation axis (cf. figure 3.1). Special cases are the collinear alignment, e.g. when nearest neighbor

interactions are dominant and $J_1 < 0$ leads to ferromagnetic order ($\varphi = 0$). On a square lattice for $J_1 > 0$ the energy gets minimal for antiferromagnetic order (antiparallel alignment of spins, i.e. $\varphi = \pi$). Spin-spiral ground states are obtained, when interactions beyond nearest neighbors become relevant. Then, the energies of spin spirals with q-vectors $\mathbf{q}$ and $-\mathbf{q}$ are degenerate, as can be easily seen in equation 4.11: the relative angle between two atoms of a spin spiral is $\varphi_{ij} = \mathbf{q} \cdot \mathbf{R}_{ij}$, and because $\cos(\varphi_{ij})$ is an even function, the sign of $\mathbf{q}$ does not enter the energy term.

Also higher order corrections like a four-spin-interaction or a bi-quadratic interaction,

$$
\begin{aligned}
E_{4-\text{spin}} &= K_{ijkl} \left[(\mathbf{S}_i \cdot \mathbf{S}_j)(\mathbf{S}_k \cdot \mathbf{S}_l) + (\mathbf{S}_i \cdot \mathbf{S}_l)(\mathbf{S}_j \cdot \mathbf{S}_k) + (\mathbf{S}_i \cdot \mathbf{S}_k)(\mathbf{S}_j \cdot \mathbf{S}_l) \right], \\
E_{\text{biquad.}} &= B_{ij} (\mathbf{S}_i \cdot \mathbf{S}_j)^2,
\end{aligned}
$$

can be derived from a Hubbard model expansion. They can be identified with the hopping of electrons across atoms in 4 steps, $1 \rightarrow 2 \rightarrow 3 \rightarrow 4 \rightarrow 1$ for the 4-spin interaction and $1 \rightarrow 2 \rightarrow 1 \rightarrow 2 \rightarrow 1$ for the bi-quadratic interaction. But also these higher order terms are even with respect to the relative angle between two spins and the degeneracy between $\mathbf{q}$ and $-\mathbf{q}$ remains.

4.2 Dzyaloshinskii-Moriya interaction

The term originating from the antisymmetric part of the interaction matrix,

$$
E_{\text{DM}} = \mathbf{D}_{ij} \cdot (\mathbf{S}_i \times \mathbf{S}_j) = (\mathbf{D}_{ij} \cdot \hat{n}) \sin(\varphi_{ij}), \tag{4.13}
$$

is called *antisymmetric exchange* or *Dzyaloshinskii-Moriya interaction* (DMI) [4,5]. The DMI favors canted spin structures, because it is largest for $|\varphi_{ij}| = \pi/2$. Due to the relation $E_{\text{DM}}(\varphi) = -E_{\text{DM}}(-\varphi)$ the degeneracy between spirals with q-vectors of opposite sign is lifted and a certain rotational direction – dependent on the sign of $\mathbf{D} \cdot \hat{n}$ – is preferred. The resulting spin structures are then called 'chiral'.

A DM-term can only occur when spin-orbit coupling is taken into account. This can be seen in the following: consider a flat spin spiral (i.e. a spiral with $\theta = 90°$, cf. equation (4.12)) with certain rotation axis and q-vector. Because the spin space is not coupled to real space in absence of SOC, a reflection in spin space can be made without changing the energy of the system: The Hamilton of this system is invariant under unitary transformations $U^\dagger H U = H$. When the reflection is chosen in such a way, that the mirror plane contains the q-vector and the rotation axis $\mathbf{R}$, the resulting spin spiral is equivalent to the initial one except that its q-vector points in opposite direction: $\mathbf{q} \rightarrow -\mathbf{q}$ (cf. figure 4.1).

Not only SOC is crucial for the existence of the Dzyaloshinskii-Moriya interaction, but also an inversion-asymmetric environment (which is e.g. introduced by a surface) is important to obtain an interaction in the form of equation (4.13). This can be seen easily in figure 4.2: In case of an appropriate structure in the surface or a structureless surface), the mirror plane which connects the two spin spirals on the left and in the middle is preserved. Hence these pairs of spin spirals are still degenerate and the corresponding
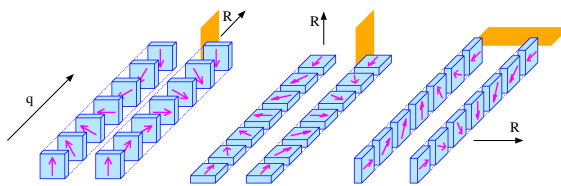
Figure 4.1: Flat spin spirals with rotation axis **R** pointing in different directions. When an initial spin spiral (left spiral of each pair) is mirrored on an appropriate mirror plane, the resulting spiral (right spiral of each pair) is the same as the initial one but with a change of sign in **q**.
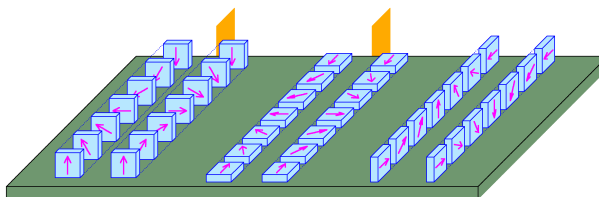

Figure 4.2: The spin spirals as in figure 4.1 are shown, but now a surface is introduced which breaks the symmetry of the environment.

components of the DM-vector, which are determined by the direction of the cross product of two adjacent spins and is thus pointing along the rotation axis, vanishes. For the pair of spirals on the right, the surface brakes the reflection symmetry and in principle a component of $\mathbf{D}_{ij}$ along the rotation axis of these spirals can exist. If the system would exhibit inversion symmetry (see figure 4.1), also this mirror plane would be preserved and all components of the DM-vector would be zero.

As one can see, the direction of the DM-vector can be determined by pure symmetry considerations for the case of spin spirals on an isotropic surface. But the symmetry could in principle also be broken by other mechanisms, such as a structure of the surface or impurities. Then the direction of the DM-vector an be determined according to the following rules [5]:

Consider two spins located at $\mathbf{R}_1$ and $\mathbf{R}_2$. The middle is labeled as $\tilde{\mathbf{R}} = (\mathbf{R}_1 + \mathbf{R}_2)/2$.

- If a center of inversion is located at $\tilde{\mathbf{R}}$: $\mathbf{D} = 0$.

- If a mirror plane perpendicular to $\mathbf{R}_1 - \mathbf{R}_2$ includes $\tilde{\mathbf{R}}$ then $\mathbf{D} \perp (\mathbf{R}_1 - \mathbf{R}_2)$.

- If a mirror plane includes $\mathbf{R}_1$ and $\mathbf{R}_2$ then $\mathbf{D} \perp$ mirror plane.

- If a two-fold rotation axis perpendicular to $\mathbf{R}_1 - \mathbf{R}_2$ includes $\tilde{\mathbf{R}}$ then $\mathbf{D} \perp$ rotation axis.

- If a n-fold rotation axis ($n \geq 2$) includes $\mathbf{R}_1$ and $\mathbf{R}_2$ then $\mathbf{D} \parallel (\mathbf{R}_1 - \mathbf{R}_2)$.

4.3 Anisotropy

The magnetic moments of materials prefer to be aligned in a certain direction, the so called easy axis. The easy axis is determined by the crystal lattice (magnetocrystalline anisotropy (MCA)).

Two physical effects contribute to the MCA: the spin-orbit coupling of the electrons and the dipole-dipole interaction.

The *dipole-dipole interaction* is usually treated classically, where the magnetization is replaced by the magnetic moments of the atoms. Influences on the electronic structure are neglected and can be expected to be small because it is a relativistic 2-particle effect. The magnetostatic interaction energy E^{dip} of a magnetic dipole at position $\mathbf{R}_0$ with moment $\mathbf{M}_0$ in a lattice is

$$E^{\mathrm{dip}} = \frac{\mu_{\mathrm{B}}^2}{2} \sum_{j \neq 0} \frac{(\mathbf{M}_j \cdot \mathbf{M}_0)\, \mathbf{R}_{j0}^2 - 3\,(\mathbf{M}_j \cdot \mathbf{R}_{j0})\,(\mathbf{M}_0 \cdot \mathbf{R}_{j0})}{|\mathbf{R}_{j0}|^5}\,, \qquad (4.14)$$

where the other dipoles are located at positions $\mathbf{R}_j$ with moments $\mathbf{M}_j$ and $\mathbf{R}_{j0} = \mathbf{R}_j - \mathbf{R}_0$ is the distance vector. The total anisotropy energy equation (4.14) has to be evaluated for all inequivalent magnetic moments of the sample.

The contribution originating from *spin-orbit coupling* must be treated quantummechanically, e.g. in the FLAPW method where the total energy is calculated with magnetization directions along high symmetry directions. The spin-orbit contribution to the anisotropy energy is enhanced at surfaces and interfaces due to the broken symmetry [43].

4.3.1 Symmetry considerations

We can expand the anisotropy energy in the polar angles and neglect terms that do not reflect the crystal symmetry. The general expansion [44] has the form

$$
\begin{aligned}
E_{\mathrm{ani}} &= \sum_j k_j\, m_j + \sum_{j,j'} k_{j,j'}\, m_j\, m_{j'} + \sum_{j,j',j''} k_{j,j',j''}\, m_j\, m_{j'}\, m_{j''} \\
&\quad + \sum_{j,j',j'',j'''} k_{j,j',j'',j'''}\, m_j\, m_{j'}\, m_{j''}\, m_{j'''} + \ldots
\end{aligned}
$$

where $j \in \{x, y, z\}$ and

$$\mathbf{M} = \begin{pmatrix} m_x \\ m_y \\ m_z \end{pmatrix}. \qquad (4.15)$$

All terms containing an odd number of moments must vanish, because both energy contributions to the MCA, the dipole-dipole and spin-orbit interaction, are invariant under inversion of spins, i.e.

$$
\left.
\begin{aligned}
E^{\mathrm{dip}}(\{\mathbf{M}_i\}) &= E^{\mathrm{dip}}(\{-\mathbf{M}_i\}) \\
\mathcal{H}^{\mathrm{SOC}} = \xi\, \mathbf{S} \cdot \mathbf{L} &= \xi\,(-\mathbf{S}) \cdot (-\mathbf{L})
\end{aligned}
\right\} \Rightarrow E_{\mathrm{ani}}(\mathbf{M}) = E_{\mathrm{ani}}(-\mathbf{M})\,. \qquad (4.16)
$$

easy axis	medium axis	hard axis	
$\hat{x}$	$\hat{y}$	$\hat{z}$	$k_x < k_y < 0$
$\hat{x}$	$\hat{z}$	$\hat{y}$	$k_x < 0 < k_y$
$\hat{y}$	$\hat{x}$	$\hat{z}$	$k_y < k_x < 0$
$\hat{y}$	$\hat{z}$	$\hat{x}$	$k_y < 0 < k_x$
$\hat{z}$	$\hat{x}$	$\hat{y}$	$0 < k_x < k_y$
$\hat{z}$	$\hat{y}$	$\hat{x}$	$0 < k_y < k_x$

Table 4.1: Possible combinations of easy, medium and hard axis and resulting relations between k_x and k_y.

Because the systems studied in this thesis exhibit a bcc(110) unit cell, we investigate the symmetry of this structure to find further conditions for the anisotropy energy. Two orthogonal mirror planes cause other terms to vanish as well. For example, the coordinate frame shall be defined as $\hat{x} \parallel [1\bar{1}0]$, $\hat{y} \parallel [001]$ and $\hat{z} \parallel [110]$ and we consider the mirrorplane in the yz-plane. Due to the relation $E_{\text{ani}}(m_x, m_y, m_z) = E_{\text{ani}}(-m_x, m_y, m_z)$ all odd terms in m_x in the expansion, such as $m_x m_y$ and $m_x m_z$, must vanish. Applying the same rules for the xz-mirrorplane gives additionally $k_{y,z} m_y m_z = 0$ and the remaining terms (in lowest order) are

$$E_{\text{ani}} = k_{x,x} m_x^2 + k_{y,y} m_y^2 + k_{z,z} m_z^2 = \mathbf{S}^{\text{T}} \underline{\mathbf{K}} \mathbf{S}.$$

where the anisotropy tensor $\underline{\mathbf{K}}$ is diagonal for the underlying crystal symmetry. The elements can be written as $k_{x,x} = \frac{2}{3} E_x - \frac{1}{3}(E_y + E_z)$ (and cyclic), where E_μ is the total
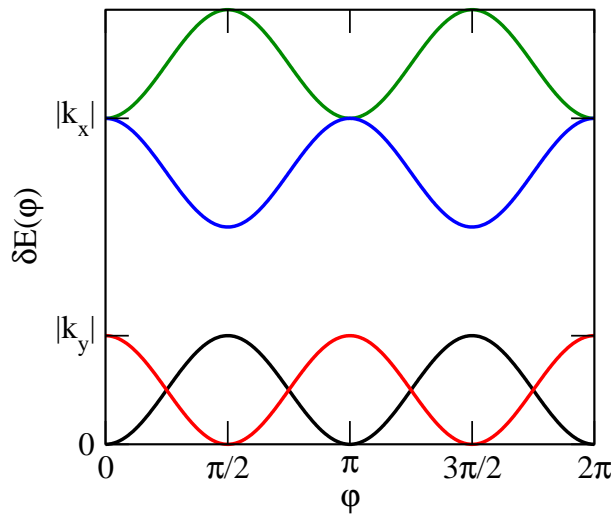

Figure 4.3: Required energy δE to rotate a spin from the easy axis into direction $\sin(\varphi)\hat{y} + \cos(\varphi)\hat{z}$. Shown are examples with the easy axis along $\hat{x}$ and the medium axis along $\hat{y}$ and $\hat{z}$ (blue and green respectively), easy axis along $\hat{y}$ (red) or easy axis along $\hat{z}$ (black).

energy of the system with magnetization in μ-direction. One easily checks that $\underline{\mathbf{K}}$ is traceless and we notice that all energies enter each component of $\underline{\mathbf{K}}$.

We want to calculate the energy δE_{ani}, which is required to turn the magnetization from the easy axis to $\mathbf{S} = (0, \sin(\varphi), \cos(\varphi))^{\mathrm{T}}$ (these terms occur e.g. in a cycloidal spin spiral along $\hat{y}$). We have to distinguish three cases and find

$$
\begin{aligned}
\text{easy axis is along } \hat{x}: \quad & \delta E_{\mathrm{ani}} = k_y \sin^2(\varphi) + |k_x| \\
\text{easy axis is along } \hat{y}: \quad & \delta E_{\mathrm{ani}} = |k_y| \cos^2(\varphi) \\
\text{easy axis is along } \hat{z}: \quad & \delta E_{\mathrm{ani}} = |k_y| \sin^2(\varphi).
\end{aligned}
$$

These functions are illustrated in figure 4.3. Similar equations are obtained when the spins have the form $(\sin(\varphi), 0, \cos(\varphi))$ (corresponding to a cycloidal spin spiral along $\hat{x}$; exchange then $\hat{x} \leftrightarrow \hat{y}$).

5 Micromagnetic models

In the previous chapter we assumed that the magnetic structure is realized by atoms exhibiting a magnetic moment, i.e. its a arrangement of discrete magnetic moments $\{\mathbf{M}_i\}$ or $\{\mathbf{S}_i\}$. However, in micromagnetic models one treats the magnetization as a continuous vector field, so the substitution $\mathbf{S}_i \to \mathbf{m}(\mathbf{r})$ with $|\mathbf{m}| = 1$ is made. This is valid if the magnitude of the moments is constant and the length scale on which the magnetic structure varies is large compared to inter-atomic distances (and to the length scale where the exchange interactions, i.e. J_{ij} and $\mathbf{D}_{ij}$, decay). In the following it is assumed, that the magnetization changes only along one spatial direction r (direction of the q-vector). The energy equation becomes a functional of the magnetization,

$$\tilde{E} = \int \mathrm{d}r \left(\tilde{A}\, \dot{\mathbf{m}}^2 + \tilde{\mathbf{D}} \cdot (\mathbf{m} \times \dot{\mathbf{m}}) + \mathbf{m}^{\mathrm{T}}\, \underline{\tilde{\mathbf{K}}}\, \mathbf{m} \right) , \tag{5.1}$$

where $\quad \tilde{E} = E/b\,, \quad \tilde{A} = \dfrac{\Delta}{2b}\sum_{j>0} j^2\, J_{0,j}\,, \quad \tilde{\mathbf{D}} = \dfrac{1}{b}\sum_{j>0} j\, \mathbf{D}_{0,j}\,, \quad \underline{\tilde{\mathbf{K}}} = \dfrac{1}{b\Delta}\underline{\mathbf{K}}\,, \tag{5.2}$

and the meaning of b and Δ is illustrated in figure 5.1. The dot denotes the derivative with respect to r, i.e. $\dot{\mathbf{m}} = \partial\mathbf{m}/\partial r$. $\tilde{A}$ is called spin stiffness constant and is an (effective) isotropic exchange constant, $\tilde{\mathbf{D}}$ is an effective Dzyaloshinskii vector and $\underline{\tilde{\mathbf{K}}}$ is the anisotropy tensor. The exchange interactions have to decay fast, because all contributions in (5.1) are local.

We again consider the bcc(110) surface in the following. If the parameters $\tilde{A}$, $\tilde{\mathbf{D}}$ and $\underline{\tilde{\mathbf{K}}}$ lead to a spin-spiral solution, due to the symmetry considerations made in section
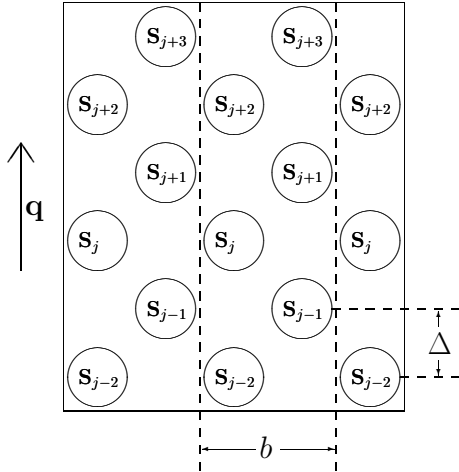

Figure 5.1: Definition of the parameter Δ and b for the effective exchange parameters (5.1).

4.2, we expect cycloidal spin structures. The DM term favors flat spin spirals and we shall consider only these in the following. This assumption is even more evident, if $\tilde{\mathbf{D}}$ points parallel to the hard axis and the anisotropy confines the magnetization to a plane perpendicular to the hard axis:

$$\mathbf{m}(r) = \sin(\varphi)\,\hat{r} + \cos(\varphi)\,\hat{z}\,, \qquad \text{where } \varphi = \varphi(r) \text{ and } \hat{r} \in \{\hat{x},\,\hat{y}\}\,. \tag{5.3}$$

The coordinate system is chosen such that $\hat{x} \parallel [1\bar{1}0]$, $\hat{y} \parallel [001]$ and $\hat{z} \parallel [110]$. Equation (5.1) takes then the form

$$\tilde{E}[\varphi] = \int \mathrm{d}r \left(\tilde{A}\,\dot{\varphi}^2 + \tilde{D}_r\,\dot{\varphi} + \delta E_{\text{ani}}(\varphi) \right) \tag{5.4}$$

where $\tilde{D}_r = \tilde{\mathbf{D}} \cdot (\hat{z} \times \hat{r})$ is the Dzyaloshinskii-vector parallel to the rotation axis and δE_{ani} is the anisotropy energy which is needed to rotate a magnetic moment from the easy axis into the direction of $\mathbf{m}$ (as defined in section 4.3.1).

5.1 Homogeneous spin spirals

If we assume homogeneous spirals, we can replace $\varphi = \frac{2\pi}{\lambda}r$ and integrating over an entire period, λ, yields

$$E' = \frac{\tilde{E}}{\lambda} = \underbrace{(2\pi)^2\tilde{A}}_{A'}\,\lambda^{-2} + \underbrace{2\pi\,\tilde{D}_r}_{D'}\,\lambda^{-1} + \bar{K}, \tag{5.5}$$

where E' has the meaning of *energy per period length*. In the following we omit the primes. The average anisotropy energy over an entire period, $\bar{K}$, depends on the direction of the easy axis $\hat{e}$:

$$\bar{K} = \begin{cases} |E_r - E_z|/2 & \text{if } \hat{e} \in \{\hat{r},\,\hat{z}\} \\ |E_e - E_z| + (E_r - E_z)/2 & \text{if } \hat{r} \perp \hat{e} \perp \hat{z} \end{cases} . \tag{5.6}$$

We find that a spin spiral with period length $\lambda = -2\,A/D$ minimizes the energy to $E = -\frac{D^2}{4A} + \bar{K}$. The spin spiral is only established, if the energy is smaller than the collinear state in the easy axis ($E = 0$). So, we find the criterion

$$\frac{\bar{K}\,A}{D^2} < \frac{1}{4} \tag{5.7}$$

for the occurrence of a spin-spiral ground state.

5.2 Inhomogeneous spin spirals

The previously mentioned homogeneous spirals, $\varphi(r) \sim r$, in fact minimize the energy functional (5.4) only when the anisotropy term is neglected (or vanishes). Minimizing the whole functional yields the following shape of the spirals [45, 46]:

$$\varphi(x) = (-\operatorname{sign}\tilde{D})\,\operatorname{am}\left(\frac{1}{\epsilon}\left(x - \frac{1}{4}X\right),\,\epsilon\right), \tag{5.8}$$

where 'am' is the Jacobian elliptic amplitude function and $x = \sqrt{\frac{\bar{K}}{\bar{A}}}\, r$ is the reduced length. We additionally assumed that $\hat{z}$ is the easy axis and thus we can write $\delta E_{\mathrm{ani}}(\varphi) = K \sin^2(\varphi)$, where $K = E_r - E_z$. X is the (reduced) period length of the inhomogeneous spiral and ϵ is a parameter corresponding to the inhomogeneity of the spiral. X and ϵ are defined via the complete elliptic integrals of first and second kind, $\mathrm{K}(\epsilon)$ and $\mathrm{E}(\epsilon)$, via

$$\frac{4}{\pi\,\epsilon}\mathrm{E}(\epsilon) \;=\; \left| \frac{\tilde{D}}{\sqrt{\tilde{A}\tilde{K}}} \right| \quad \text{and} \tag{5.9}$$

$$X \;=\; 4\epsilon\,\mathrm{K}(\epsilon)\,. \tag{5.10}$$

Instead of ϵ one often uses another dimensionless measure for inhomogeneity, namely

$$\kappa = (\mathrm{E}(\epsilon)/\epsilon)^{-2} = \frac{16}{\pi^2}\frac{AK}{D^2}\,, \quad \kappa \in [0,\,1]\,. \tag{5.11}$$

The spiral is (nearly) homogeneous for $\kappa \searrow 0$ (resulting in a nearly constant slope of the profile $\varphi(r)$) and becomes maximally inhomogeneous for $\kappa \nearrow 1$. In the latter case, the magnetization rotates slowly when it points in direction of the easy axis (regions with $\varphi = 0$ and $\varphi = \pi$) and rotates very fast over the hard axis ($\varphi = \pi/2$ and $\varphi = 3\pi/2$, respectively), which corresponds to two collinear domains with $\sin^2\varphi \approx 0$. Different profiles of inhomogeneous spirals are shown in figure 5.2. Additionally the pitch of an inhomogeneous spiral increases compared to the pitch of a homogeneous one, which is shown in the right panel of the picture. Thus, a spin spiral is only established for $\kappa < 1$, which corresponds to the condition

$$\frac{K\,A}{D^2} < \frac{\pi^2}{16} \Leftrightarrow \frac{\bar{K}\,A}{D^2} < \frac{1.23}{4} \quad \text{with } \bar{\mathrm{K}} = \frac{\mathrm{K}}{2}\,. \tag{5.12}$$

This condition is weaker than the equation (5.7) for homogeneous spirals.

5.3 About the general form of the micromagnetic model

We can transform the discrete expressions of the magnetic interactions (equation (4.10)) into a micromagnetic model following Aharoni [47] using the Taylor expansion around a fixed point $\mathbf{r}_j$ for one component, μ, of the magnetization

$$m_\mu(\mathbf{r}) = m_\mu(\mathbf{r}_i) + (\mathbf{r} - \mathbf{r}_i) \cdot \nabla m_\mu|_{\mathbf{r}=\mathbf{r}_i} \tag{5.13}$$

and neglect higher order terms if the magnetization varies slowly from $\mathbf{r}_i$ to $\mathbf{r}$. We can now insert $\mathbf{r} = \mathbf{r}_j$ and notice that $\mathbf{m}(\mathbf{r}_i) \to \mathbf{S}_i$. This allows us to write

$$\mathbf{S}_i - \mathbf{S}_j \to \mathbf{m}(\mathbf{r}_i) - \mathbf{m}(\mathbf{r}_j) = (\mathbf{r}_{ij} \cdot \nabla)\mathbf{m}(\mathbf{r}_i)\,, \tag{5.14}$$

where $\mathbf{r}_{ij} = \mathbf{r}_i - \mathbf{r}_j$ is the distance between lattice site i and j.
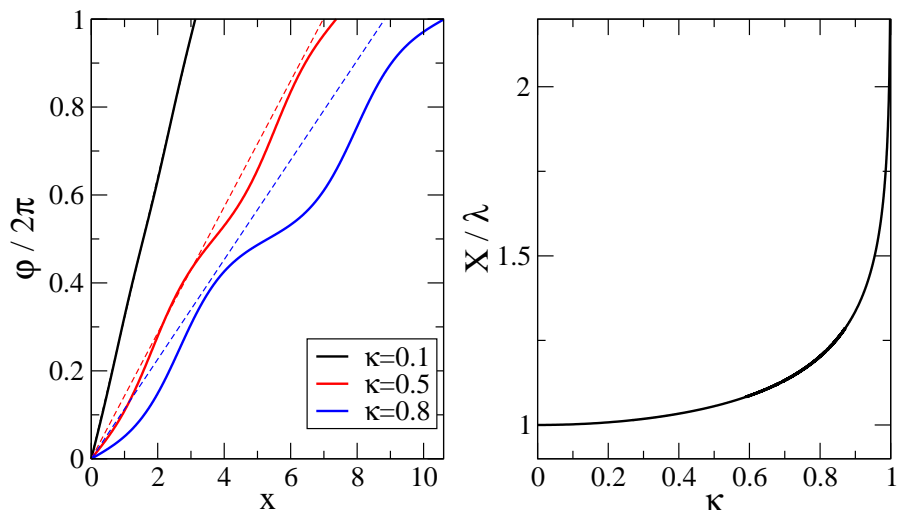
Figure 5.2: Left panel: Profiles of inhomogeneous spin spirals with different values for κ (solid lines). $x = \sqrt{\frac{\tilde{K}}{\tilde{A}}}\, r = 2\pi\sqrt{\frac{K}{A}}\, r$ is the reduced length. The dashed lines represent the profile of homogeneous spirals with the same A, D and K. When κ is large, the pitch of an inhomogeneous spiral is larger than the corresponding homogeneous one. This is also illustrated in the right panel, where the ratio X/λ is shown as function of κ, where X and λ is the pitch of an inhomogeneous and homogeneous spiral, respectively. The ratio diverges at $\kappa = 1$. If $\kappa > 1$, the collinear state is energetically preferred and no spin spiral is created.

Considering only quasi-onedimensional magnetic structures (as above $\mathbf{m} = \mathbf{m}(r)$), we can write

$$\mathbf{m}(r_i) - \mathbf{m}(r_j) \propto \left. \frac{\partial \mathbf{m}}{\partial r}\right|_{r=r_i} = \dot{\mathbf{m}}(r_i)\,. \tag{5.15}$$

This allows us e.g. to transform

$$1 - \mathbf{S}_i \cdot \mathbf{S}_j = \frac{1}{2}\left(\mathbf{S}_i - \mathbf{S}_j\right)^2 \rightarrow \frac{1}{2}\left(\mathbf{m}(r_i) - \mathbf{m}(r_j)\right)^2 \propto \dot{\mathbf{m}}(r_i)^2 \tag{5.16}$$

or

$$\mathbf{S}_i \times \mathbf{S}_j = \mathbf{S}_i \times \left(\mathbf{S}_j - \mathbf{S}_i\right) \rightarrow \mathbf{m}(r_i) \times \left(\mathbf{m}(r_j) - \mathbf{m}(r_i)\right) \propto \mathbf{m}(r_i) \times \dot{\mathbf{m}}(r_i)\,, \tag{5.17}$$

which is the form as they appear in the micromagnetic energy functional (5.1).

Finally we also want to mention that the shape of a material with finite extensions gives contributions to the anisotropy tensor $\underline{\tilde{\mathbf{K}}}$. However, this contribution vanishes in the case of antiferromagnetic materials and can therefore be assumed to be zero for antiferromagnetic spin spirals.

6 Unsupported monolayer of bcc Cr(110)

In this chapter, spin-spiral calculations are done to investigate the spin stiffness in the system

> 1 atomic layer Cr(110) with W-lattice constant, referred to as Cr(110).

This very small and simple system is chosen because the validity of approximations (e.g. the force theorem) and the stability of the results with respect to numerical cutoffs can be tested quickly.

  This chapter is divided into the following parts: First, the structural setup is explained and definitions are given, then the computational details are described briefly. Finally the results (followed by several tests) are presented.

6.1 The structural setup

6.1.1 The bcc(110) unit cell

Let us first describe the chemical lattice: Cr has a body centered cubic (bcc) unit cell. Thus, the unit cell in a (110)-plane is rectangular with lattice parameters a and $\sqrt{2}\,a$, where a denotes the lattice constant of the bcc unit cell. The atoms are placed at the corners of the rectangle and in the middle (see figure 6.1). The optimal choice (i.e. the smallest) is the centered rectangular (c-r) unit cell containing one atom. In this chapter, the W bulk lattice constant was chosen because in chapter 7 we will describe a system, where an atomic monolayer of Cr is deposited on a W substrate.

  If Cr was non- or ferromagnetic, one could work with the centered-rectangular unit cell right from the start. However, Cr(110) exhibits an antiferromagnetic order, where the magnetic moments of two neighboring atoms point in opposite direction. Therefore a primitive rectangular (p-r) unit cell should be chosen in order to describe the two magnetic sublattices caused by the different orientation of magnetic moments. However, the centered-rectangular unit cell can still be used to produce the antiferromagnetic state, but in this case a spin-spiral calculation must be performed, where additionally to
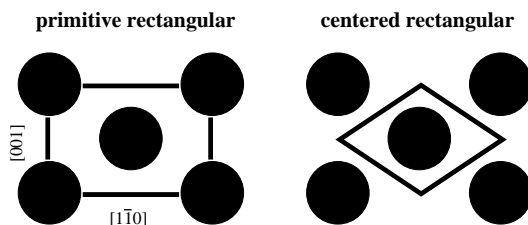

Figure 6.1: The two possible choices of the unit cell of the bcc(110) lattice plane.

computation time c-r vs. p-r unit cell	
number of k-points needed	$1 : \frac{1}{2}$
diagonalization of (non-magnetic) Hamiltonian	$1 : 8$
extension to AFM calculation	$8 : 2$

Table 6.1: Comparison of computation time for calculations using the two different unit cells.

a translation also a rotation in spin space is performed. The corresponding spin-spiral q-vector is $\tilde{\mathbf{q}} = (0.5, 0.5)$, where the $\tilde{\ }$ denotes that the vector is given in units of the Bravais vectors of the reciprocal space (see also chapter 6.1.3).

6.1.2 What about the computation time?

So which unit cell shall we use? In case of reproducing the AFM state it does not matter, because for both unit cells the computation time is 8 times larger than in a non-magnetic calculation in the c-r unit cell, as it is summarized in table 6.1: Because the computation time scales with the third power of the number of basis atoms, one iteration for one k-point takes 8 times longer when the p-r unit cell is used, but the Brillouin zone is smaller and can be sampled equally good by using only half as many k-points. This leaves a factor of 4 in comparison with the smaller unit cell. When the AFM state is computed one can still perform collinear calculations with the p-r unit cell, which leads to an increase in computation time by 2 compared to a nonmagnetic calculation because the Kohn-Sham equation can be solved for the up- and down-component separately. In case of the c-r unit cell, a non-collinear calculation must be performed and because of that, the coupled Kohn-Sham equations must be solved which takes 8 times as long as solving the the non-magnetic equation.

When we leave the special case of the AFM but want to compute spin spirals with arbitrary $\mathbf{q}$, non-collinear calculations have to be performed anyway and a calculation with the c-r unit cell is faster by a factor of 4 and therefore used preferably in the following analysis. However, the p-r unit cell has to be used e.g. if spin spirals with a cone angle $\theta \neq \pi/2$ are computed.

Finally we remark, that the choice of the unit cell does not matter if the same magnetic structure shall be computed with them. This is further pointed out in section 6.5.

6.1.3 Brillouin zone and q-vectors

The q-vectors of spin spirals are elements of the reciprocal space. The Brillouin zone for both unit cells is is shown in figure 6.2. The c-r unit cell (in blue) is spanned by the vectors $\mathbf{b}_1$ and $\mathbf{b}_2$. The AFM state is produced by a q-vector which points to the edge of the c-r unit cell (shown in red).

Let us consider the case of the p-r unit cell: the q-vector producing the AFM lies outside the first Brillouin zone. This is the case, because here we have a two-atomic basis and thus q-vectors in the second Brillouin zone produce other magnetic structures
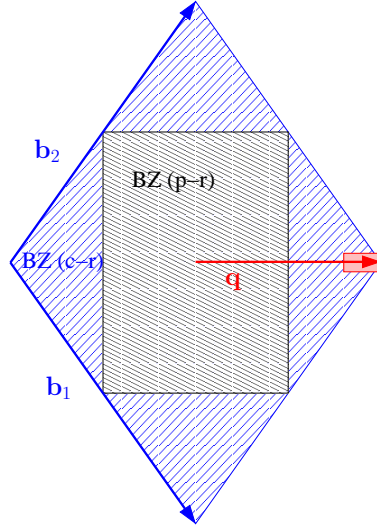
Figure 6.2: Brillouin zones of c-r (shaded blue area) and p-r (shaded black area) unit cells. The c-r unit cell is spanned by the reciprocal basis vectors $\mathbf{b}_1$ and $\mathbf{b}_2$. The AFM state is produced by the spin-spiral vector $\mathbf{q}$ (red). The investigated range around the AFM state is denoted by the red area.

than the corresponding q-vectors from the first Brillouin zone (i.e. the ones which differ by a reciprocal lattice vector).

Let us come back to the c-r unit cell. The Bravais matrix, consisting of the basis vectors of reciprocal space defined as row-vectors, reads

$$
B = \begin{pmatrix} \frac{2\pi}{a_1} & -\frac{2\pi}{a_2} \\ \frac{2\pi}{a_1} & \frac{2\pi}{a_2} \end{pmatrix} = \begin{pmatrix} \frac{\sqrt{2}\pi}{a} & -\frac{2\pi}{a} \\ \frac{\sqrt{2}\pi}{a} & \frac{2\pi}{a} \end{pmatrix} \tag{6.1}
$$

where $a_1 = \sqrt{2}a$ and $a_2 = a$ are the length of the edges of the rectangular unit cell. Thus, q-vectors in units of the Bravais lattice (in the following denoted by a $\tilde{\ }$) can be transformed into Cartesian units by multiplication from the left, $\mathbf{q} = \tilde{\mathbf{q}} \cdot B$.

A vector pointing along the long axis of the crystal ($[1\bar{1}0]$-direction) is defined as

$$
\tilde{\mathbf{q}} = (q, q), \quad q \in (-0.5, 0.5]. \tag{6.2}
$$

Multiplication with the Bravais matrix quickly ensures that this vector is indeed pointing along $[1\bar{1}0]$: $\mathbf{q} = (\sqrt{8}\pi q/a, \, 0)$ and its length is determined by q. The angle between the magnetic moments of two atoms is determined by their distance vector $\mathbf{R}$ via

$$
\varphi = \mathbf{q} \cdot \mathbf{R}. \tag{6.3}
$$

In the following we want to describe antiferromagnetic spin spirals. It is convenient to split the spin-spiral q-vector into 2 parts:

$$
\tilde{\mathbf{q}} = \tilde{\mathbf{q}}_0 + \tilde{\mathbf{q}}_{\text{eff}} \, . \tag{6.4}
$$

The first part corresponds to a rotation of π from one lattice site to another (i.e. it creates the antiferromagnetic order) and one finds $\tilde{\mathbf{q}}_0 = (0.5, 0.5)$. The second part describes the antiferromagnetic spin spiral,

$$\tilde{\mathbf{q}}_{\text{eff}} = (\Delta q,\, \Delta q)\,. \tag{6.5}$$

Again it can be transformed into the Cartesian coordinate system by multiplication with the B-matrix giving

$$\mathbf{q}_{\text{eff}} = (\sqrt{8}\pi\Delta q/a,\, 0). \tag{6.6}$$

The period length is then determined by $2\pi = \mathbf{q}_{\text{eff}} \cdot (\hat{e}\,\lambda)$, where $\hat{e}$ is the unit vector in $[1\bar{1}0]$-direction. This leads to an expression for the period length of the AFM-spiral:

$$\lambda_{[1\bar{1}0]} = 2\pi\,\frac{a}{\sqrt{8}\pi\Delta q} = \frac{a}{\sqrt{2}\Delta q} \tag{6.7}$$

Similar expressions are obtained, when the effective part of the q-vector is pointing along $[001]$:

$$\tilde{\mathbf{q}}_{\text{eff}} = (\Delta q,\, -\Delta q)\,, \tag{6.8}$$

$$\mathbf{q}_{\text{eff}} = (0,\, -4\pi\Delta q/a)\,, \tag{6.9}$$

$$\lambda_{[001]} = \frac{a}{2\Delta q}\,. \tag{6.10}$$

Finally we note, that spin spirals with q-vectors $+\mathbf{q}$ and $-\mathbf{q}$ are degenerate in absence of spin orbit coupling, as already pointed out in chapter 4.

6.2 Computational details

The following cutoff-parameter were found to be sufficient: Concerning the generation of the Hamiltonian: $g_{\text{max}} = 10.3\,a_0^{-1}$ and $g_{\text{max,xc}} = 8.5\,a_0^{-1}$ were used for the plane wave expansion of the potential and XC-potential, respectively, and $\ell_{\text{nonsph}} = 6$ was used as cutoff for the non-spherical part of the Hamiltonian. Its spherical part and LAPW basis set contained spherical harmonics up to $\ell_{\text{max}} = 8$. The basis' plane wave expansion cutoff was set to $k_{\text{max}} = 3.8\,a_0^{-1}$. The GGA lattice constant of W was used, i.e. $a = 6.03\,a_0$. The muffin-tin radius was chosen as $2.3\,a_0$ and the temperature broadening was set to $k_B T = 0.001\,\text{htr}$.

Force theorem calculations were done for flat spirals in the $[001]$-direction: First, the charge density was converged in antiferromagnetic order, until its distance from one iteration to the other was less than $10^{-6}\,\frac{\text{e}}{a_0{}^3}$ (if it was converged even further, it will be pointed out explicitly in the next chapter 6.3). The full two dimensional Brillouin zone (2DBZ) was sampled by 512 k-points. Then force theorem calculations were only a self-consistent solution to the antiferromagnetic magnetization (AFM) was calculated, and this charge density was used for 11 q-vectors ranging from $|\Delta q| = 0$ to $|\Delta q| = 0.1$. One has to keep in mind, that in the force theorem step only the magnetization in the muffin-tin spheres is rotated, but the interstitial magnetization stays the same. This

induces an error in the computation of the energy, because the situation is similar to rotating a magnetic moment in an external magnetic field. The larger the rotation is, the larger the energy to rotate the moment becomes. Therefore it is necessary to set the interstitial magnetization to zero. Then also an error is made, but it is at least independent of the rotation angle. This procedure seems to be quite venturesome, but it leads to correct results, as will be shown in section 6.4.

Also self-consistent calculations were performed for the same q-vectors, either for flat spirals or for spirals with a cone angle $\theta = 30°$.

6.3 Dispersion and non-parabolic behavior
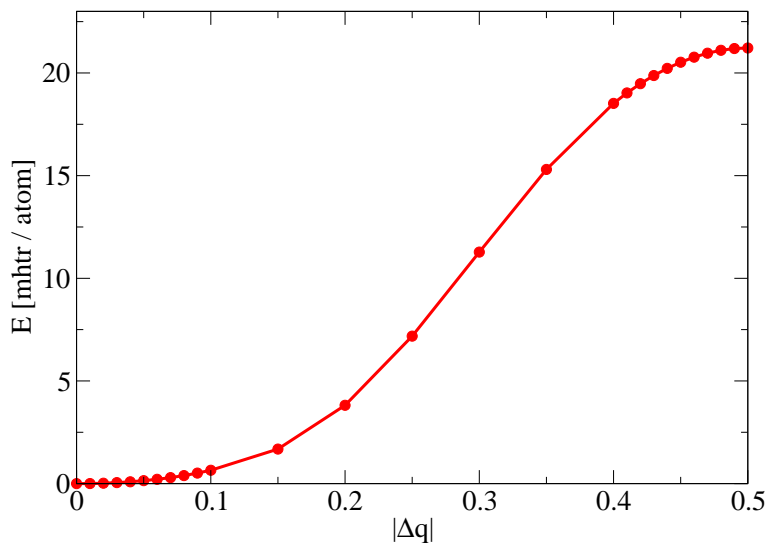
Figure 6.3: Dispersion relation $E(\mathbf{q})$ along the [001]-direction for flat spin spirals. The energy was computed for several spin spirals between the AFM state ($\Delta q = 0$) and the FM state ($\Delta q = 0.5$).

In figure 6.3, the dispersion curve along the [001]-direction is shown. One sees that the antiferromagnetic state is the ground state. One should regard this figure as a qualitative behavior, because due to the force theorem only spirals around the AFM should be described well. The main difference between force theorem and self-consistent calculations is, that the magnetic moment (which in general is also a function of $\mathbf{q}$) changes much less in a force theorem calculation.

From the nearest neighbor Heisenberg model, which assumes also a constant magnetic moment over the whole magnetic structure, one expects a behavior of the form $E \propto -J \cos(qd)$ where d is the nearest neighbor distance and J is the nearest neighbor exchange integral. Because of this behavior, the curve is expected to start quadratically for small Δq:

$$E(\Delta q) = A \, (\Delta q)^2 + E_0 \tag{6.11}$$

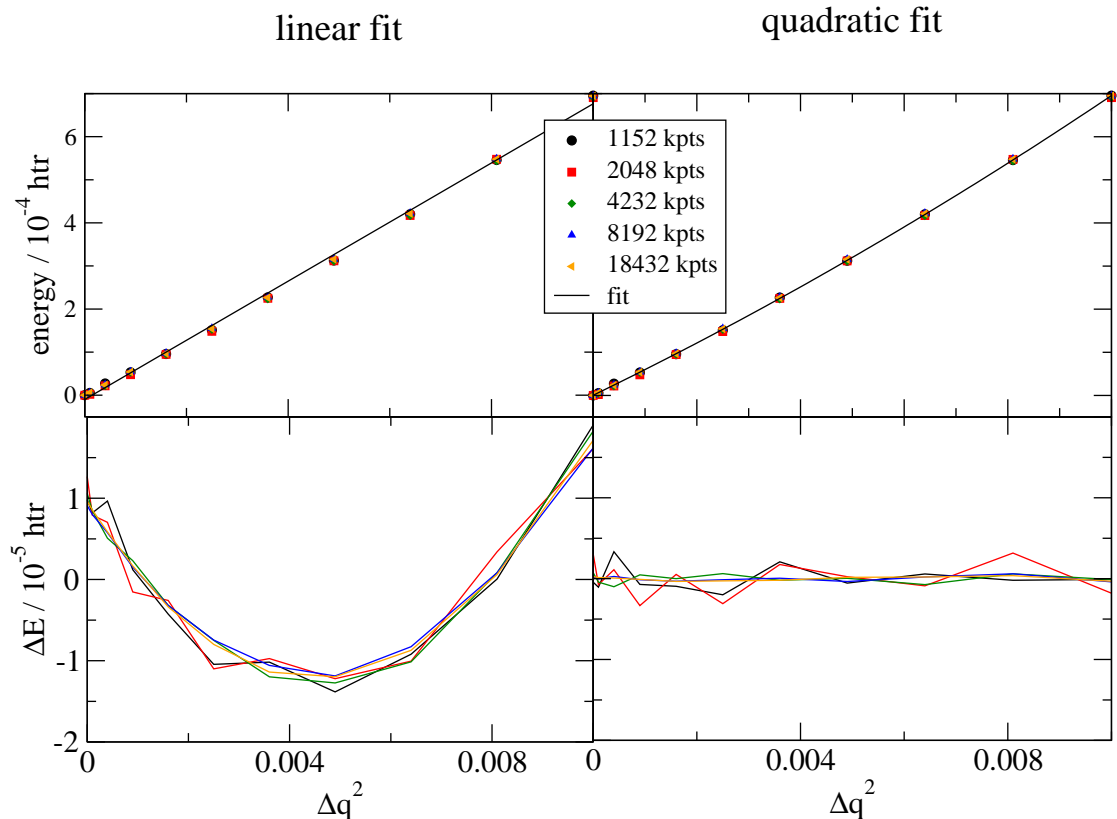where A is the spin stiffness and E_0 is the energy of the AFM state.

Figure 6.4: Top: calculated energies of spin spirals with different k-point sets (colored symbols) including a linear (left) and quadratic (right) fit to the 1152 k-points data. Bottom: residuals to the linear and quadratic fits, respectively. To each k-point set an individual fit was performed and the residuals were calculated. However, the fitted parameters do not change much with respect to the used k-point set, see text.

In the top left panel of figure 6.4, the calculated energies for spin spirals for different k-point sets (colored symbols) are plotted against $(\Delta q)^2$. Thus, a parabolic dispersion relation becomes a straight line in this picture. Least squares fit to the data corresponding to the 1152 k-point set is shown as solid line. At the left bottom panel the residuals $\Delta E = E_{calc} - E_{fit}$ are shown, which are not randomly distributed around zero but follow a regular behavior.

The behavior of the residuals is not a consequence of a badly converged calculation, as it was resistant against many cutoff parameters: the number of k-points (as seen in this picture), ℓ_{max}, ℓ_{nonsph}, g_{max} and $g_{max,xc}$. Neither changing the lattice constant nor the muffin-tin radius nor choosing another unit cell (primitive-rectangular with 2-atomic basis instead of centered-rectangular with 1-atomic basis) made this regular deviation

from a parabolic fit vanish.

But the dispersion relation around the AFM could be described better by applying a fit of the form

$$E(\Delta q) = A_2 \left(\Delta q\right)^4 + A_1 \left(\Delta q\right)^2 + E_0 \qquad (6.12)$$

with fit parameters A_2, A_1 and E_0. Such a quartic fit appears as a parabolic curve in figure 6.4 (upper right panel, solid line). The residuals to a fit of this form are one order of magnitude smaller than the corresponding residuals to a quadratic fit and do not follow a regular behavior, but are randomly distributed around zero (cf. right bottom panel of figure 6.4).

The fitted parameters are shown in the following table. The uncertainties are in the range of a few percent or less.

parameter	value / htr	relative uncertainty
A	0.0687	5%
A_1	0.0583	2%
A_2	1.02	0.5%

However, this deviation cannot be addressed to the next higher order term in a Taylor expansion of the previously mentioned cosine,

$$E = \frac{J}{2}(2\pi q)^2 - \frac{J}{24}(2\pi q)^4 + O(q^6)\,, \qquad (6.13)$$

because the ratio $A_2/A_1 = 17$ is much bigger than the ratio of the expansion coefficients ($\frac{\pi^2}{3} \approx 3.3$) and the sign differs! The non-parabolic behavior might be due to higher order interactions, such as bi-quadratic or four-spin interactions.

6.4 How good is the Force Theorem? - Calculations with coned spirals

As already explained earlier, the force theorem provides a tool to accomplish calculations with different magnetic states very quickly. The energy difference of two states (an initial and a final state) is first order in the deviation of their magnetic structure with respect to each other, which corresponds in our case to the deviation of the q-vectors of the two states. The force theorem gives a good estimate if the deviation is small, and the quality of the approximation will decrease with increasing difference Δq.

In order to disturb the initial magnetic structure less, one can introduce a cone angle (in contrast to flat spirals as used in the previous section). Such a spiral with a cone angle $\theta = 45°$ is shown in the top half of figure 6.5. The azimuthal angle of the spin differs by $\Delta\varphi = 45°$ on neighboring sites, which can be seen in the lower half of the picture, where the projection of the spin onto the xy-plane is shown. The different orientation of spin-up (blue) and -down (red) moments with respect to the quantization axis causes an additional change of $\Delta\varphi = 180°$ to the projection of the blue magnetic moments. Because antiferromagnetic spin spirals with $\theta \neq \pi/2$ cannot be computed
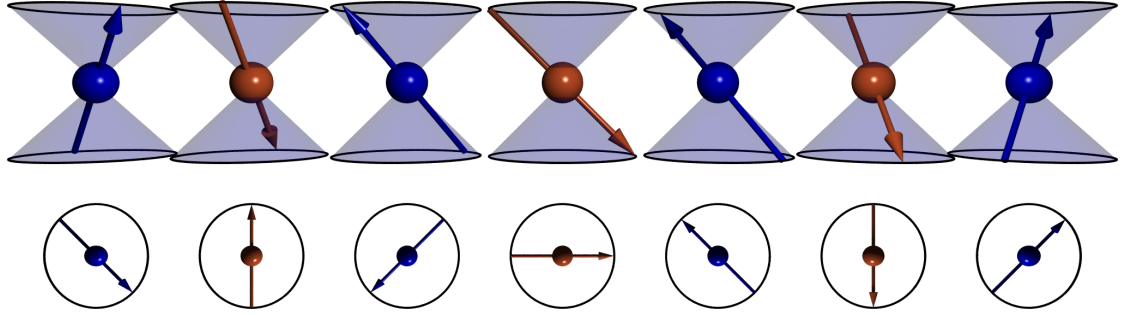
Figure 6.5: Coned spirals with cone angle $\theta = 45°$ and spin rotation axis pointing along $\hat{z}$-direction. Upper half: view from the side. The projection of the magnetic moments onto the $\hat{z}$-axis is positive for blue and negative for red atoms, respectively. Lower half: projection onto the xy-plane.

with a 1-atomic unit cell, we have to use two atoms to form a sublattice structure. Then also a phase shift α between the two sublattices can be introduced.

In the simplest case of a classical Heisenberg model where only nearest neighbor interactions are taken into account, the interaction energy per atom is given by

$$E = -\frac{J_1}{4} \sum_{i=1}^{4} \mathbf{S}_0 \cdot \mathbf{S}_i \,, \tag{6.14}$$

where the five spins are defined by

$$\mathbf{S}_0 = \begin{pmatrix} \sin\theta \\ 0 \\ \cos\theta \end{pmatrix} \,, \qquad \mathbf{S}_i = \begin{pmatrix} \sin\theta \, \cos(\varphi_i) \\ \sin\theta \, \sin(\varphi_i) \\ \cos\theta \end{pmatrix} \,, \tag{6.15}$$

$$\varphi_1 = \varphi_4 = -2\pi\Delta q + \alpha \,, \tag{6.16}$$

$$\varphi_2 = \varphi_3 = 2\pi\Delta q + \alpha \,. \tag{6.17}$$

The situation is also sketched in figure 6.6, where $\mathbf{S}_0$ is represented by the red arrow in the middle. The two sublattices exhibit a phase shift, denoted by the angle between the red and the black arrow (which corresponds to a normal spin spiral without phase shift).

By simple calculation and using some trigonometric equations, one finds

$$E(\Delta q, \alpha, \theta) = -2J_1 \sin^2\theta \left[\sin^2\frac{\alpha}{2} + \pi^2 \cos\alpha \, (\Delta q)^2 + \mathcal{O}\left((\Delta q)^4\right)\right] + J_1 \,. \tag{6.18}$$

The changes in the magnetic structure (when varying $\mathbf{q}$) are small when the cone angle is small. This can be easily seen when one considers the limit $\theta = 0$: The magnetic moments point in $\hat{z}$-direction and any rotation around $\hat{z}$ leaves the magnetic structure invariant (and thus the energy is constant). The changes in the magnetic structure also increase with α, as can be seen when one considers spirals with $\theta = 90°$: then $\alpha = 0$
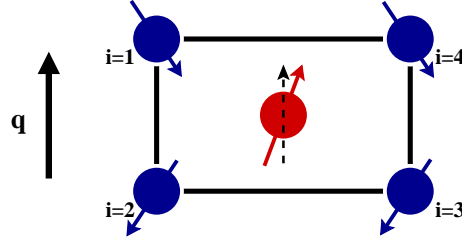
Figure 6.6: The spin $\mathbf{S}_0$ (red arrow) is canted with respect to it's normal position of a spin spiral (black) by an angle α.

describes the antiferromagnetic (initial) state and the deviation is largest for $\alpha = 180°$, where the ferromagnet is obtained.

One can also take higher order terms into account, e.g. interactions of $N = 5$ neighboring shells with exchange constant J_n (see figure 6.7). The energy of the red atom then reads

$$E(\Delta q, \alpha, \theta) = -2J \sin^2 \theta \left[\chi \sin^2 \frac{\alpha}{2} + \pi^2 \left(\zeta \cos \alpha + (1 - \zeta) \right)(\Delta q)^2 + \mathcal{O}\left((\Delta q)^4 \right) \right] + \text{const.},$$
(6.19)

$$\text{where} \quad J = J_1 + 2\,J_2 + 4\,J_4 + 9\,J_5 \;, \quad \chi = \frac{J_1 + J_5}{J} \quad \text{and} \quad \zeta = \frac{J_1 + 9\,J_5}{J} \;.$$
(6.20)

Thus, the general form of equation (6.18) is obtained with scaling factors χ and ζ, which occur because only spins from the other sublattice contribute to the change in energy when a phase shift between the two sublattices is introduced. One could also take more neighboring shells than $N = 5$ into account, but the form of equation (6.19) would not change (but the constants J_{eff}, χ and ζ would contain more contributions).
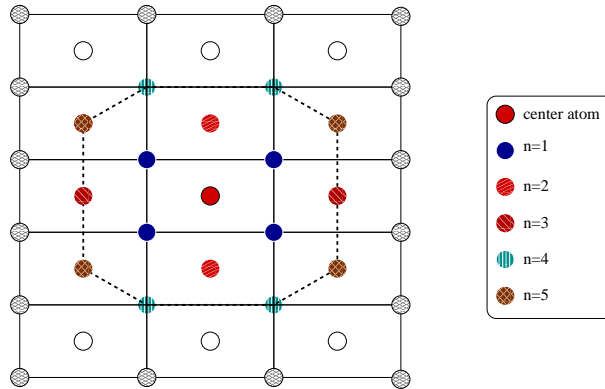
Figure 6.7: The bcc(110) lattice structure. The 5 next nearest neighbors to the center atom (red) are indicated where n denotes the order of the neighbor.

6.4.1 Computational details

Antiferromagnetic coned spin spirals are calculated in the 2-atomic unit cell. The cutoff parameters concerning the basis set and potential are the same as in the first paragraph of 6.2.

The force theorem was applied to investigate the dependence of the spin-spiral energy on (a) the cone angle θ and (b) the phase shift α. The Hartree- and XC-potential were computed from a converged density (with 256 k-points). Usually 2304 k-points were used for the calculation of the single particle energies (if not, it is mentioned explicitly).

Because the unit cell is now twice as large as the one-atomic unit cell (the Brillouin zone is then half as big), the q-vector $\tilde{\mathbf{q}}_{2-\text{atomic}} = (0, q_0)$ has to be chosen as $q_0 = 2\,\Delta q$ (Δq as in equation (6.5)) to produce the same magnetic structure as in spin-spiral calculations using the 1-atomic unit cell. For better comparison to the 1-atomic unit cell, in the following Δq is used as scale of the plots. Energies are usually given per 2-atomic unit cell.

6.4.2 Variation of the cone angle θ

From equation (6.18) a $\sin^2\theta$ - behavior is expected and can actually be confirmed by our force theorem calculations (see figure 6.8). The spin-spiral vector was chosen to be $\Delta q = 0.03$. Two sets of calculations were done, where the initial state was a coned spiral with $\theta_{\text{start}} = 30°$ (diamonds) or the AFM state ($\theta_{\text{start}} = 0°$, diamonds), which agree very nice. From the $\sin^2\theta$-curve an effective exchange constant $J = \frac{105\,\mu\text{htr}}{2\pi^2\,0.03^2} = 5.9\,\text{mhtr}$ can be deduced.

6.4.3 Variation of the spin-spiral vector q

The dependence on the q-vector is shown in figure 6.9 (here 4608 k-points were used). A large range of q-vectors is shown and it is not believed that the force theorem can be used with the flat spirals to describe the dispersion curve accurately in the whole region. However, one can see the trend and estimate a limit for Δq, in which the force theorem can be applied: The energy difference $\delta E = E_{\text{flat}} - 4\,E_{\text{cone}}$ is with less than $10^{-5}\,\text{htr}$ very small for for very long spin spirals ($\Delta q \leq 0.03$), in a range of $0.03 < \Delta q \leq 0.17$ flat spirals underestimate and for larger q-vectors they overestimate the energy compared to coned spirals.

In figure 6.10 the uncertainty in the spin stiffness is determined. In case of coned spirals a higher number of k-points is needed to gain convergence. Please note that the self consistent values are obtained by using a one-atomic unit cell, which needs twice as many k-points to sample the Brillouin equally dense as a unit cell containing two atoms. The energies were multiplied by 2 for the same reason. Values for the spin stiffness are determined by linear fits in the right panel of this picture. They are:
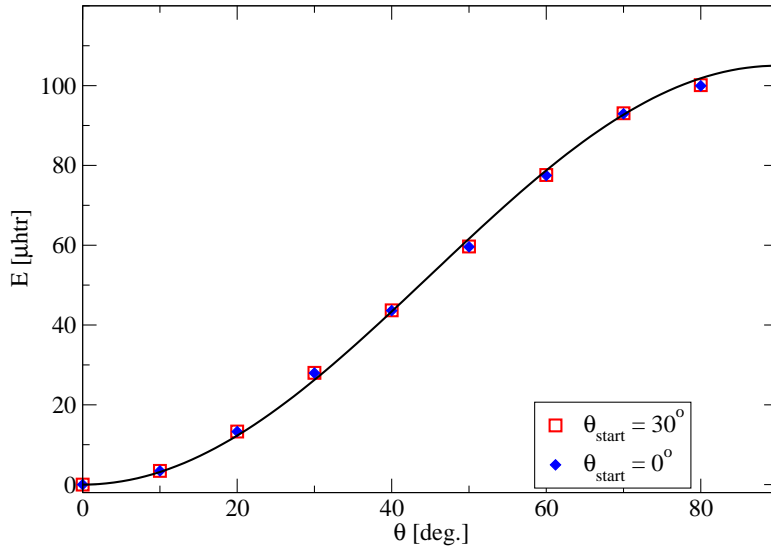
Figure 6.8: Energy dependence of the cone angle θ for a fixed q-vector ($\Delta q = 0.03$). For $\theta = 0$ the spins are ordered antiferromagnetically along the $\hat{z}$-axis, for $\theta = 90°$ the flat spiral is established. The two sets differ in the cone angle θ_{start} of the initial magnetic state. The solid line is a $\sin^2$-curve as guide to the eye.
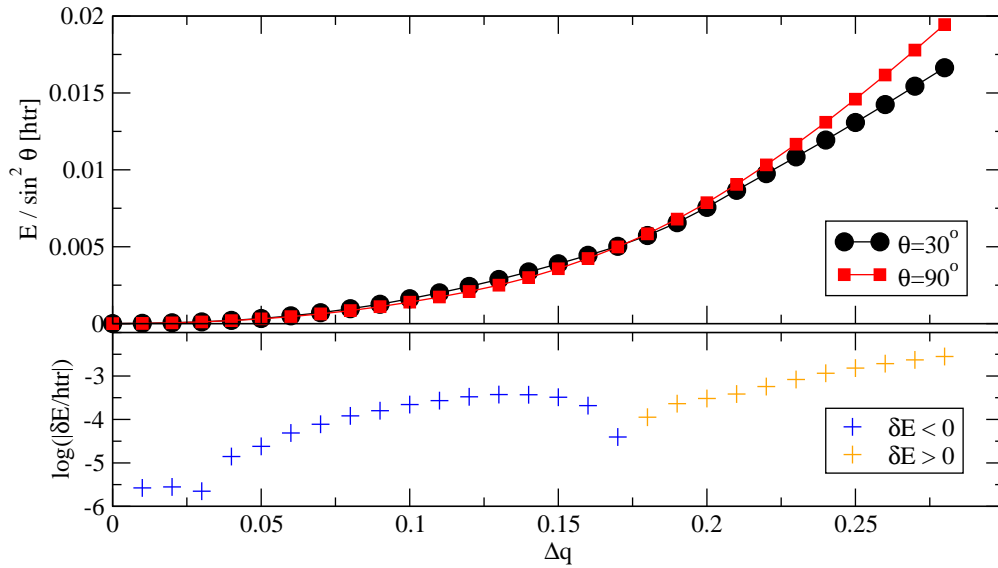

Figure 6.9: Comparison between flat and coned spirals ($\theta = 30°$) computed with the 2-atomic unit cell. The energies are given per unit cell. The sign of the energy difference $\delta E = E_{flat} - 4\,E_{cone}$ is coded by the color in the log-plot (lower half).

data set	A [htr]
FT, $\theta = 90°$	0.119
FT, $\theta = 30°$ (1)	0.127
FT, $\theta = 30°$ (2)	0.122
SC, $\theta = 90°$	0.110

Thus the error made by applying the force theorem is found to be about 10% for the investigated range around the AFM. Interestingly, the fit to the noisy data gives already a quite resonable etimate for the spin stiffness. Using equation (6.19) we can deduce an effective echange constant $J = -A/2\pi^2 \approx 6.0$ mhtr, which agrees with the value $J = 5.9$ mhtr obtained from varying the cone angle θ.
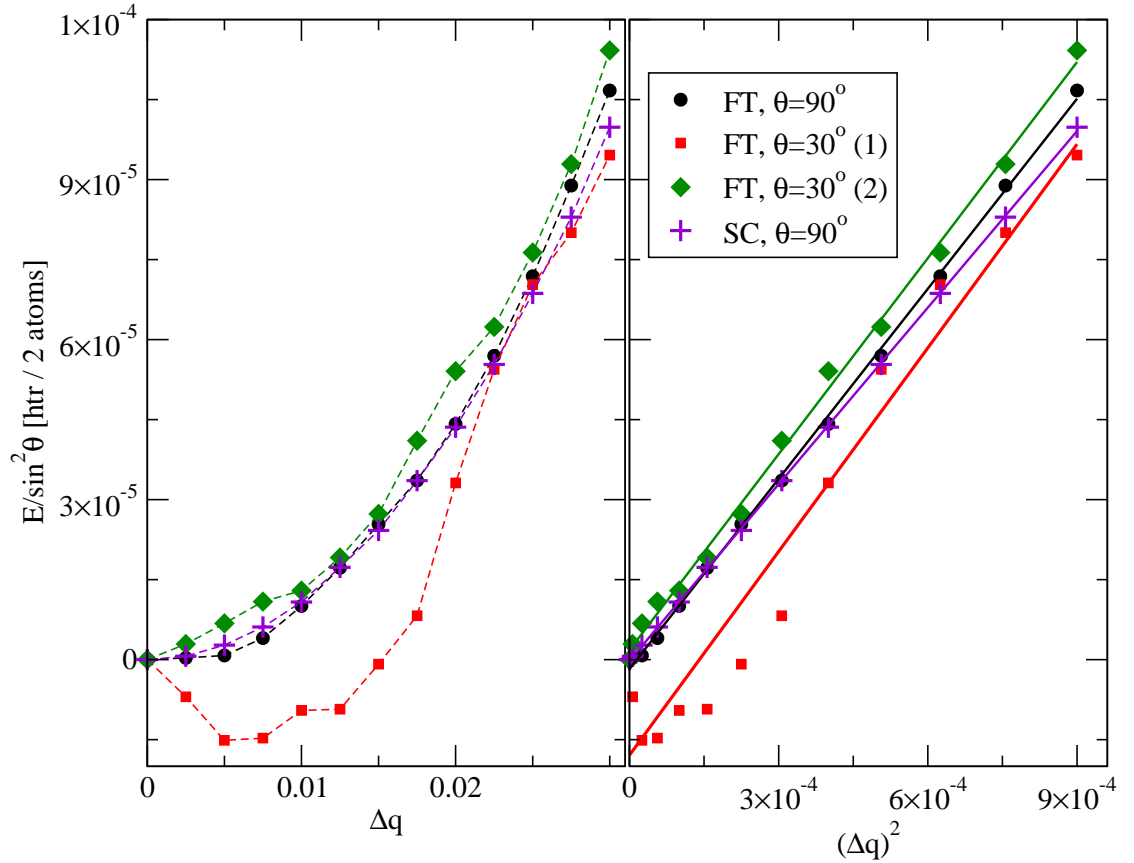
Figure 6.10: Determination of spin stiffness: The calculated energies are plotted in the left panel. For flat spirals (circles) 2304 k-points are sufficient to get a converged dispersion, for coned spirals the same number of k-points (squares) is insufficient. Instead, 8464 k-points (diamonds) give a smoother curve. The self consistent values (crosses) are obtained with flat spirals using 4232 k-points and a one-atomic unit cell. Right panel: linear fits to the data (plotted against $(\Delta q)^2$) give the spin stiffness (see text).

6.4.4 Variation of the phase shift α

The dependence on the phase shift α between the two sublattices for two different cone angles is shown in figure 6.11 where $\Delta q = 0$ was chosen. Let's compare the results for the two cone angles $\theta = 30°$ (filled symbols) and $\theta = 90°$ (open symbols): The same energies (up to 10^{-10} htr) were obtained for $\alpha = 0$, for $\alpha = \pi/4$ they are nearly the same and the difference becomes big for $\alpha \geq 3\pi/4$.

The $\theta = 30°$-data is nicely described by a $\sin^2(\alpha/2)$–fit, as expected from equation (6.18), giving a value of $-2\chi J = 33$ mhtr. This gives a value $\chi = 2.7$. The energies obtained with flat spirals are less good described by a $\sin^2(\alpha/2)$–fit, which indicates that the force theorem is less valid.
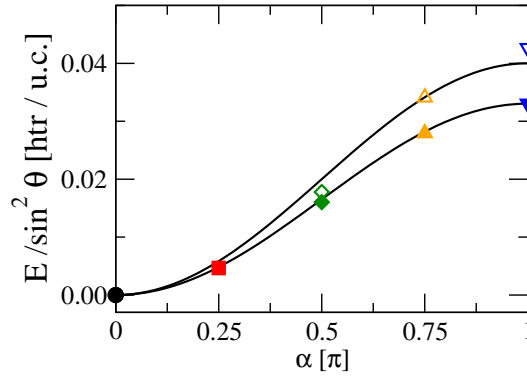
Figure 6.11: Energies of magnetic configurations with phase shift α. Open symbols denote flat spirals, filled symbols represent coned spirals ($\theta = 30°$). The data for $\alpha = 0$ and $\alpha = \pi/4$ are the same for both types of data and thus the open symbols are hidden behind the filled ones. The colors correspond to the branches shown in figure 6.12

Also the dispersion $E(\Delta q)$ for $\alpha = 0$, $\pi/2$, $\pi/2$, $3\pi/4$ and π was computed. Let us first consider flat spirals, which are shown in the top left panel of figure 6.12. The dispersion is very flat for fixed α. The AFM state is produced by $(\Delta q, \alpha) = (0, 0)$ (black) and spin spirals with nearly antiferromagnetic order ($\Delta q \leq 0.03$) are lowest in energy. The other limit, namely when the spins are aligned ferromagnetically, is obtained by choosing $(\Delta q, \alpha) = (0, \pi)$ (blue). Flat spin spirals with nearly ferromagnetic ordering are about 0.043 htr higher in energy.

To reveal the shape of the dispersion the quantity $\delta E = E(\Delta q, \alpha) - E(0, \alpha)$ for each α is plotted as function of Δq in the lower left panel of the figure, where one indeed identifies the AFM to be the ground state and the energy increases quadratically with Δq because of the lowest order expansion of equation (6.18) with $\alpha = 0$. For the $(\alpha = \pi)$−branch, the "pure" ferromagnet $(\Delta q, \alpha) = (0, \pi)$ is highest in energy and the energy of nearly ferromagnetic spin spirals deviates also quadratically because of the same reason (Taylor expansion with $\alpha = \pi$), but now with different prefactor $1 - 2\zeta$ in equation (6.19)). However, because the very different magnetic structure with respect
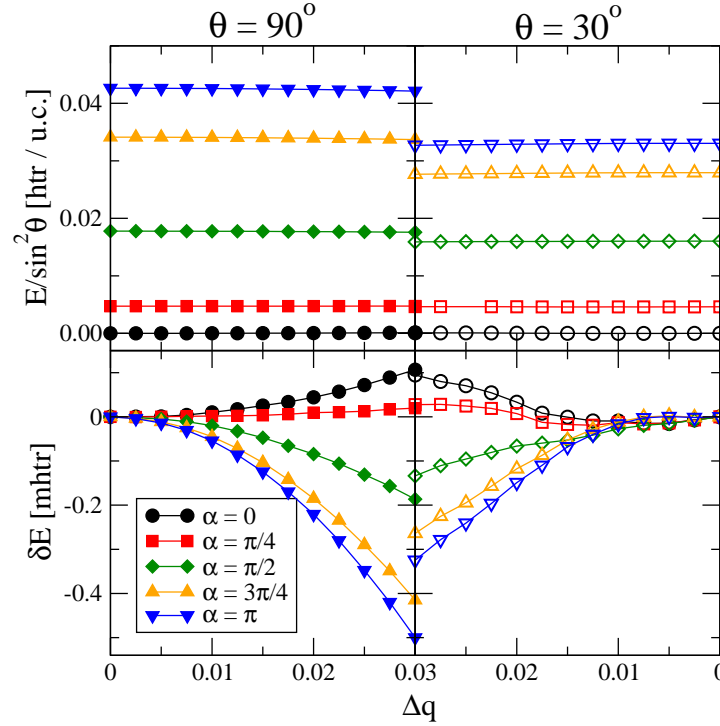
Figure 6.12: Top: Dispersion curves $E(\Delta q)$ for different phase shifts α for flat (left, closed symbols) and coned spirals (right, open symbols). The dispersion is very flat for a fixed α (top panel). In the lower panel $\delta E = E(\Delta q, \alpha) - E(0, \alpha)$ for each α is shown. For details see text.

to the initial (i.e. converged) state, the force theorem gives a wrong result in magnitude. Please remember that the whole $(\alpha = \pi)$−branch is 0.043 htr higher in energy than the $(\alpha = 0)$−branch and thus the negative values of δE do not indicate the ground state.

One can compare this behavior with the dispersion $E(\Delta q)$ where Δq ranges over the whole Brillouin zone (figure 6.3, page 45): the $(\alpha = 0)$−branch reflects the region around $\Delta q = 0$ and the $(\alpha = \pi)$−branch reflects the behavior around $\Delta q = 0.5$, respectively. Also the energy (per atom) between AFM and FM is the same:

$$\Delta E = \frac{0.043 \, \text{htr}}{2 \, \text{atoms}} = 22 \, \text{mhtr}$$

agrees nicely with the value of 22 mhtr obtained from figure 6.3. However, we have to keep in mind that the force theorem is only applicable when the changes in the magnetic structure are small. This is obviously not the case when one compares the two extremal cases of AFM and FM.

The same calculations as for flat spirals were done with coned spirals ($\theta = 30°$). One finds the same trends (cf. right half of figure 6.12). If one compares the several branches of coned spirals with the corresponding energies from flat spiral calculations (upper

right), one recognizes that the energies agree nicely for $\alpha = 0$ and $\alpha = \pi/4$ (as already seen in figure 6.11). The shape of the dispersion is again plotted in the lower panel of figure 6.12. One again sees that the dispersion curves for coned spirals are more noisy, but they will get smoother for a more dense k-point set (in analogy to figure 6.10 for the $\theta = 30°$-curves).

6.5 Dependence on the choice of the unit cell

Test calculations with flat spin spirals were done to investigate, if calculations with a one- and two atomic unit cell are consistent. Force theorem calculations were done using a starting density which was converged with 256 k-points. The following k-point sets were used to calculate the single particle energies (the sets are also illustrated in figure 6.13):

- set A: for c-r unit cell, 4608 k-points (excluding the Γ-point)

- set B_1: for p-r unit cell, 2304 k-points (including the Γ-point)

- set B_2: for p-r unit cell, 2304 k-points (excluding the Γ-point, congruent with set A)

Please notice that since the 2DBZ of the two-atomic unit cell is half as big as the 2DBZ of the one-atomic one, only half of the k-points have to be used to reproduce the same accuracy.
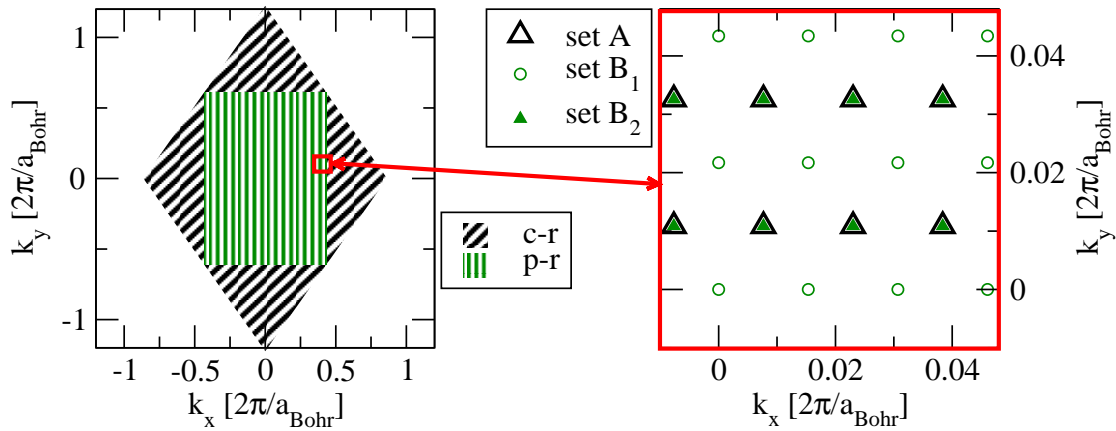
Figure 6.13: On the left the whole Brillouin zone of the c-r and p-r unit cell is shown. On the right the sampling with three k-point meshes is shown. Mesh A and B_2 are congruent, B_1 is shifted.

The computed energies are shown in figure 6.14. The comparison shows that the energy dispersion is in very good agreement between the two unit cells ($\Delta E \approx 10^{-6}$ htr). When one compares the sets A and B_2, which result in the same sampling of the 2DBZ,
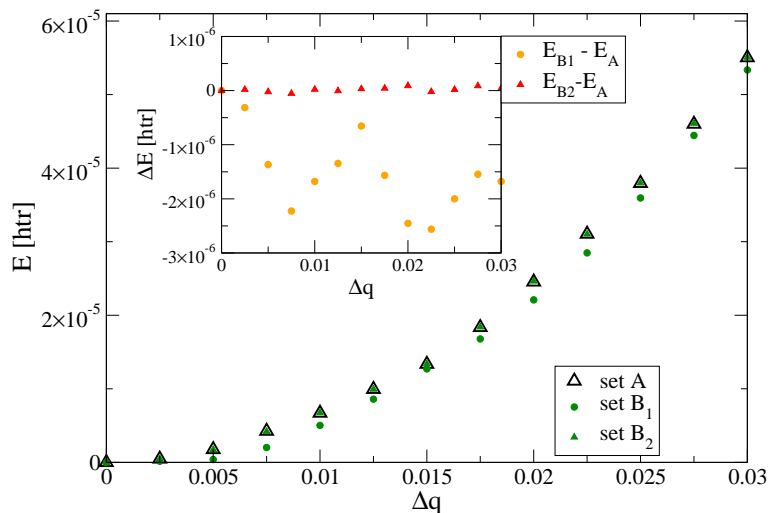
Figure 6.14: Energy calculations using the force theorem with different k-point sets and unit cells. The calculations of 1 atomic unit cells and 2 atomic unit cells with equivalent k-point sampling give the same results (set A and B$_2$, respectively).

the curves are even nearly identical: the deviations are of order 10^{-8} htr. They come from slight differences in the starting density. Quadratic fits to the data give the following spin stiffness and they agree within 1 percent or less:

	A	B$_1$	B$_2$
$[10^{-2} \frac{\text{htr}}{(2\pi/a)^2}]$	6.06	5.94	6.07

6.6 Conclusion

We have investigated the spin stiffness for an atomic monolayer of Cr for spirals along [001] with period lengths $\lambda > 5\,a \approx 1.6$ nm (corresponding to $\Delta q < 0.1$). In the dispersion also higher order interactions are revealed. For spin spirals with very long period lengths ($\lambda > 16\,a \approx 5.2$ nm, corresponding to $\Delta q < 0.03$), the applicability of the force theorem was tested and it was found, that the error made by the force theorem can be addressed to approx. 10%. In the test, the following accuracies could be evaluated:

- Flat spiral calculations using the 1-atomic and 2-atomic unit cell, respectively, agree within 1%.

- Force theorem calculations with coned and flat spirals, respectively, agree within 3%.

- Flat spiral calculations applying the force theorem and and self-consistent calculations, respectively, agree within 8%.

7 Spin spirals in 1 atomic monolayer of Cr on W(110)

The previously described concepts are used to analyze the magnetic properties of one atomic monolayer Cr on a (non-magnetic) W(110) substrate. The ground state of this system is of particular interest. The broken inversion symmetry can give rise to the Dzyaloshinskii-Moriya interaction (DMI), which will in general favor canted spin structures and compete with other magnetic interactions such as magnetocrystalline anisotropy (MCA). Experiments [48] indicate a noncollinear ground state, which supports our interest in a theoretical analysis of this particular system.

Ab-initio calculations can show the magnitude of the different effects and therefore help to identify the relevant interactions. Different approximations can be used to determine certain effects, e.g. it is sufficient to perform calculations in scalar-relativistic approximation to determine the spin stiffness, whereas spin-orbit coupling is crucial for the MCA and DMI.

In this chapter, the three model parameters for a micromagnetic model (anisotropy, K, Dzyaloshinskii-Moriya interaction, D, and spin stiffness, A) are determined by fits to suitable DFT calculations. Then, the ground state of the system is determined and a comparison to the experiment is made.

7.1 The tungsten substrate

Tungsten is chosen as substrate, because it has a high spin-orbit coupling strength. Its bulk structure can be described by a body centered unit cell, i.e. a cubic lattice with lattice parameter a and a two atomic basis:

$$\tau_1 = (0,\, 0,\, 0)^T\,,\quad \tau_2 = (a/2,\, a/2,\, a/2)^T\,.$$

The experimental lattice parameter is $a_{\mathrm{exp}} = 3.1652\,\text{Å} = 5.98\,a_0$.

We performed DFT calculations using GGA [20] and LDA [18] exchange correlation functionals to determine the lattice parameter. The total energy was calculated for various lattice constants around the experimental value for both types of XC-functionals. The following cutoff-parameter were used (without testing the convergence with respect to these): Concerning the generation of the Hamiltonian: $g_{\mathrm{max}} = 11.8\,\mathrm{a}_0^{-1}$ and $g_{\mathrm{max,xc}} = 9.9\,\mathrm{a}_0^{-1}$ were used for the plane wave expansion of the potential and XC-potential, respectively, and $\ell_{\mathrm{nonsph}} = 8$ was used as cutoff for the non-spherical part of the Hamiltonian. Its spherical part and LAPW basis set contained spherical harmonics up to $\ell_{\mathrm{max}} = 10$. The muffin-tin radius was chosen as $2.52\,\mathrm{a}_0$ and the temperature broadening was set to $k_B T = 0.001$htr.

Figure 7.1: Total energy calculations to determine the W bulk lattice constant (symbols) and quadratic fits (lines). The arrows indicate the minimum with respect to the fits. The experimental value is indicated by a blue arrow.
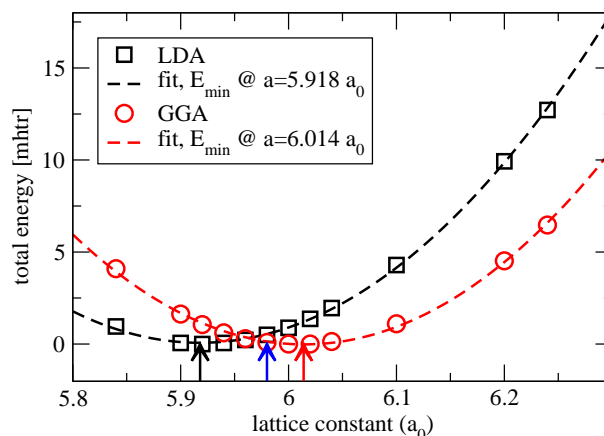
Self-consistent, non-magnetic total energy calculations were performed. The convergence with respect to the number of k-points in the irreducible part of the Brillouin zone IBZ (N_{kpts}, the IBZ equals to 1/48 of the full Brillouin zone) and the basis' plane-wave expansion cutoff k_{max} was tested. The following values were found to be sufficient: $N_{kpts} = 252$ and $k_{max} = 4.0\,a_0^{-1}$. Changing these values to $N_{kpts} = 616$ and $k_{max} = 4.5\,a_0^{-1}$ lead to no changes in the differences of the total energy.

The results are plotted in figure 7.1. The lattice constants agree within 1%:

in a.u.	LDA	GGA	exp.
$a\,[a_0]$	5.92	6.01	5.98

For the following analysis, the GGA lattice parameter was used.

7.2 The thin film Cr/W(110): structure

The system of interest is approximated by a thin film consisting of 1 layer of Cr and 7 layers of W(110) (if more than 7 W-layers were used, it is mentioned explicitly in the rest of this chapter). The two-dimensional unit cell of the bcc(110) structure is rectangular with lattice parameters a and $\sqrt{2}a$ (as already discussed in chapter 6.1.1). The position of the atoms in the surface and interface layer is indicated in figure 7.2 and subsequent layers are repeated according to this sequence.

The Cr layer was relaxed with respect to the W substrate, where the W-W interlayer distance was kept constant at $d_{W-W} = a/\sqrt{2} = 4.264\,a_0$. A symmetric film with 7 W layers, covered with a Cr layer on each side was used to determine the relaxations. Self-consistent calculations with an antiferromagnetic order of the Cr layer were performed. The following parameters were used: GGA was used as exchange-correlation functional, because LDA tends to overestimate the relaxation and thus leads to a stronger hybridization (and thus an overestimated transfer of magnetic moment to the substrate) [49]. The muffin-tin radii were set to $2.3\,a_0$ for Cr and $2.5\,a_0$ for W. The irreducible part of the two-dimensional Brillouin zone was sampled by 20 k-points (corresponding to 80 k-points in the full 2DBZ). For the basis set plane waves up to a wave vector of $k_{max} = 4.5\,a_0^{-1}$
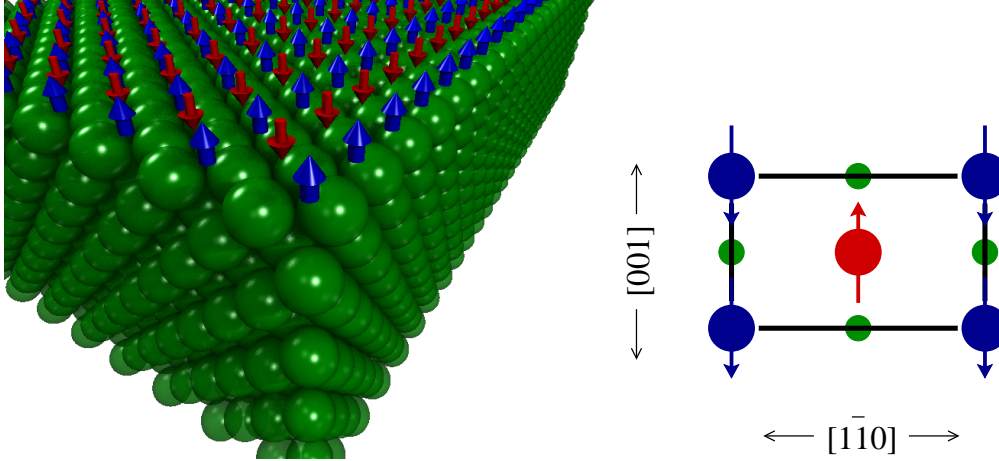
Figure 7.2: Left: W(110) slab covered with an atomic monolayer of Cr. Green spheres represent the non-magnetic W atoms, red and blue arrows represent the magnetic moments of the Cr atoms. Right: top-view onto the surface. Cr-surface atoms (i.e. layer 1) are shown as red and blue circles. The position of the W-interface atoms (i.e. layer 2) is indicated by green circles. The subsequent layers are repeated according to this sequence (i.e. ABAB...)

were used and spherical harmonics up to $\ell_{max} = 8$ were used in the muffin tins. The potential $g_{max} = 11.8\,a_0^{-1}$ and $g_{max,xc} = 9.9\,a_0^{-1}$ were used. Nonspherical parts to the Hamiltonian were taken up to $\ell_{nonsph} = 6$ were considered. The temperature broadening was set to $k_B T = 0.001\,htr$.

The Cr-W distance was determined to be $d_{Cr-W} = 3.896\,a_0$, which corresponds to an inwards-relaxation of 8.6% with respect to the W-W interlayer distance. This agrees with the experimental observation of an relaxation of $-8.0 \pm 0.7\%$ from LEED studies and other GGA calculations (-8.5%, both results from Ref. [48]).

7.3 Magnetic structure

For the rest of this chapter, the structure described in section 7.2 is used. LDA [18] is used as exchange correlation functional for magnetic calculation, because the most widely used PBE-GGA functional [20] is constructed especially for collinear magnetic structures. Additionally, LDA is mostly used for magnetic calculations and thus the community is most experienced with it.

The cutoff parameter for the basis set and potential generation are chosen as described in section 7.2. The number of desired k-points varies with respect to the searched quantity and convergence with respect to this parameter will be an issue of each subsequent chapter.

7.3.1 Magnetic Moments

Magnetic moments originating from the spin of the electrons were calculated with 512
k-points (in the whole 2DBZ of the centered rectangular unit cell) in scalar-relativistic
approximation. Checks with 1152 k-points allow to estimate an uncertainty of $0.001\,\mu_\mathrm{B}$.
Additionally, the spin and orbital moments including SOC were calculated in the primi-
tive rectangular unit cell, where it was found that 256 k-points are sufficient to determine
them: for the spin (orbital) magnetic moments a relative uncertainty of $1\% = \mathcal{O}(10^{-2})$
($\mathcal{O}(10^{-1})$) in the 4 (5) topmost layers remained, whereas it was one order of magnitude
larger in the other layers (comparisons were made with moments obtained by sampling
the full BZ with 1024 k-points).

layer - no.	1	2	3	4	5
atom - type	Cr	W	W	W	W
$\mu_\mathrm{S}\,[\mu_\mathrm{B}]$ (SR)	2.41	0.211	0.044	0.016	0.003
$\mu_\mathrm{S}\,[\mu_\mathrm{B}]$ (SOC)	2.41	0.206	0.0422	0.0114	0.004
$\mu_\mathrm{L}\,[10^{-2}\,\mu_\mathrm{B}]$	-2.42	-1.7	-0.36	-0.28	-0.38

Let's first look at the spin moments: The non-magnetic W atoms get spin-polarized
due to hybridization with the magnetic Cr atoms, where the magnitude of spin-polarization
decreases with increasing distance from the Cr-layer. The coupling is antiferromagnetic
within the W layers and from layer to layer, if the nearest neighbor atoms are considered
(see figure 7.3). The other W-layers (number 6 to 8) have vanishing spin moment within
the limit of our accuracy or are too close to the W surface on the other side of the film,
where an enhanced magnetic moment due to the lower coordination number of the W
atoms exists. This is an artifact due to the finite thickness of the film in contrast to
a semi-infinite substrate, as it almost appears in nature. This fact is also revealed by
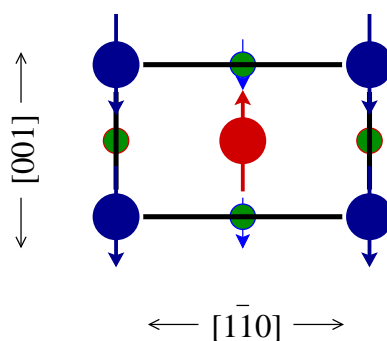calculations with a different number of W layers (see figure 7.4).

Figure 7.3: Unit cell analog to figure 7.2, with induced spin-polarization of the W in-
terface layer. The orientation of the magnetic moment of the W interface is
indicated by blue and red outer circles, which correspond to spin-down and
-up, respectively.

The orbital moments are by a factor of 100 smaller in magnitude, but decay slower than the spin moments. By comparison it is found, that the five topmost layers are not affected too much by the finite thickness of the film. Additionally, the orbital moment depends on the direction of the magnetic moment due to spin-orbit coupling (see figure 7.5). The orbital moments are largest in magnitude for an in-plane magnetization along the [001]-direction.
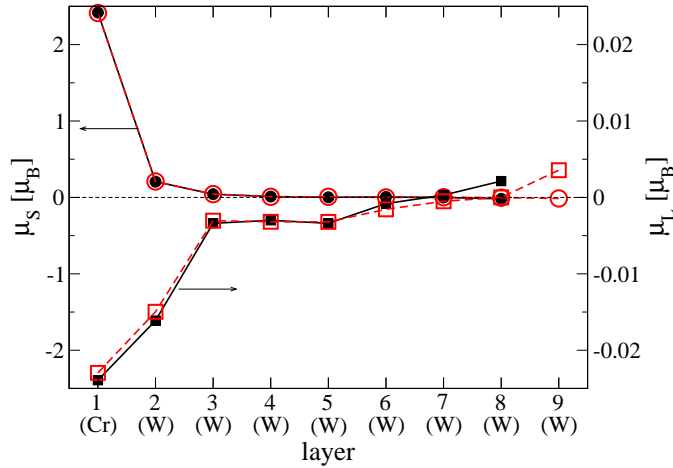

Figure 7.4: Spin and orbital moments (circles and squares, respectively) for the layers of a 8 layer (black) and 9 layer (red) film. They couple antiparallel. Mind the different scale for the spin- (left) and orbital-moments (right) of 2 orders of magnitude.
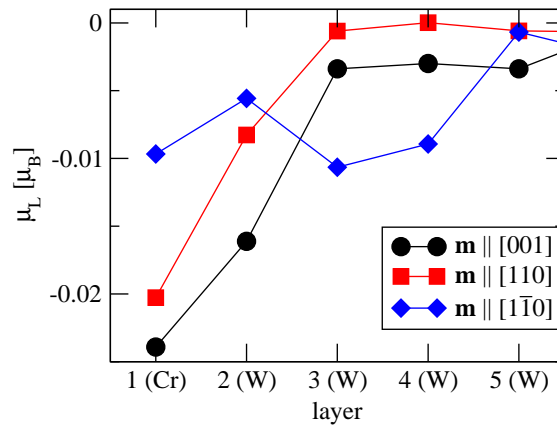
Figure 7.5: Orbital moments of the 5 topmost layers of a 8 layer film with spin moments along the three high symmetry directions. The orbital moments depend on the magnetization direction due to spin-orbit coupling. The orbital moments are largest in magnitude for an in-plane magnetization along [001].

kpts-set	$l_x/\delta x$	ρ	N_{kpts}
1a	48	1	4608
2a	48	2	2304
3a	48	3	1536
4a	48	4	1152
1b	72	1	10368
2b	72	2	5184
3b	72	3	3456
4b	72	4	2592

Table 7.1: Used k-point sets to investigate the importance of the distribution of k-points in the 2DBZ. ρ is the ratio $(\delta y/l_y)/(\delta x/l_x)$ where the meaning of these quantities is illustrated in figure 7.6.

7.4 Calculation of the Dzyaloshinskii-Moriya-Interaction

7.4.1 Computational Scheme

A charge density of the AFM state was converged using the generalized Bloch theorem with 512 k-points in the full 2DBZ, until the distance in charge density from one iteration to the other was $\mathcal{O}(10^{-6}\,\frac{\text{e}}{\text{a}_0^3})$. Afterwards, the spin-spiral ground state was computed (i.e. the force theorem was applied) and first order perturbation theory was used to evaluate the change in energy due to spin-orbit coupling. Five spin spirals with q-vectors pointing along the [1$\bar{1}$0] and [001]-direction were computed, where $\Delta q = 1/96, 3/96, \cdots 9/96$ (as defined in equation (6.5)) was chosen.

7.4.2 Test: optimal Brillouin zone sampling

It was tested which sampling of the Brillouin zone (BZ) ensures the fastest convergence of the result. For this test only spin spirals along the long axis of the two-dimensional unit cell (i.e. [1$\bar{1}$0]) were computed. The k-points were distributed as illustrated in figure 7.6: the length of the BZ are $l_x = \pi/\sqrt{2}a$ and $l_y = \pi/a$ (x and y correspond to the crystallographic directions [1$\bar{1}$0] and [001], respectively). Different ratios $\rho = (\delta y/l_y)/(\delta x/l_x)$ of densities among x and y-direction were tested, as well as different total numbers of k-points $N_{\text{kpts}} = 2\,(l_y/\delta y)\,(l_x/\delta x) = 2(l_x/\delta x)^2/\rho$. The sets given in table 7.1 were used.

Let us comment on the fact that k-meshes of type $\rho > 1$ were considered: When SOC in spin spirals is treated beyond first-order perturbation theory, the q-vectors and the k-point grid have to match [14]: when $\mathbf{k}$ is a point of the k-mesh, then $\mathbf{k}' = \mathbf{k} + \mathbf{q}$ must be a point of the mesh as well. This results in very dense k-meshes and a large number of k-points for long spirals (i.e. small q-vectors). The computational effort can then be reduced by sampling the BZ in the direction normal to $\mathbf{q}$ with less accuracy. However, this restriction does not hold if SOC is treated in first order perturbation theory.

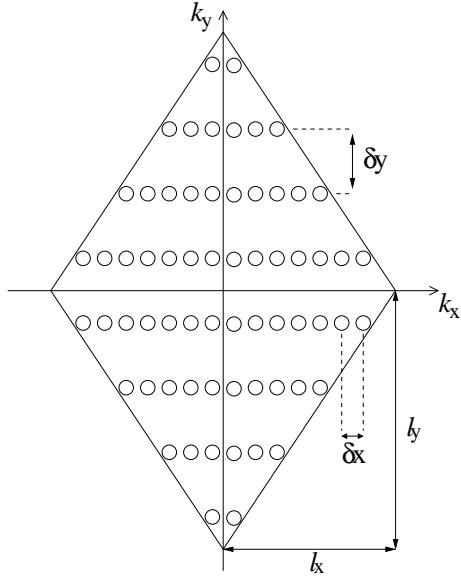The result is shown in the left panel of figure 7.7. Calculations having $\rho = 1$ (set 1a

Figure 7.6: Illustration of a k-point set, sampling the two-dimensional Brillouin zone (2DBZ).
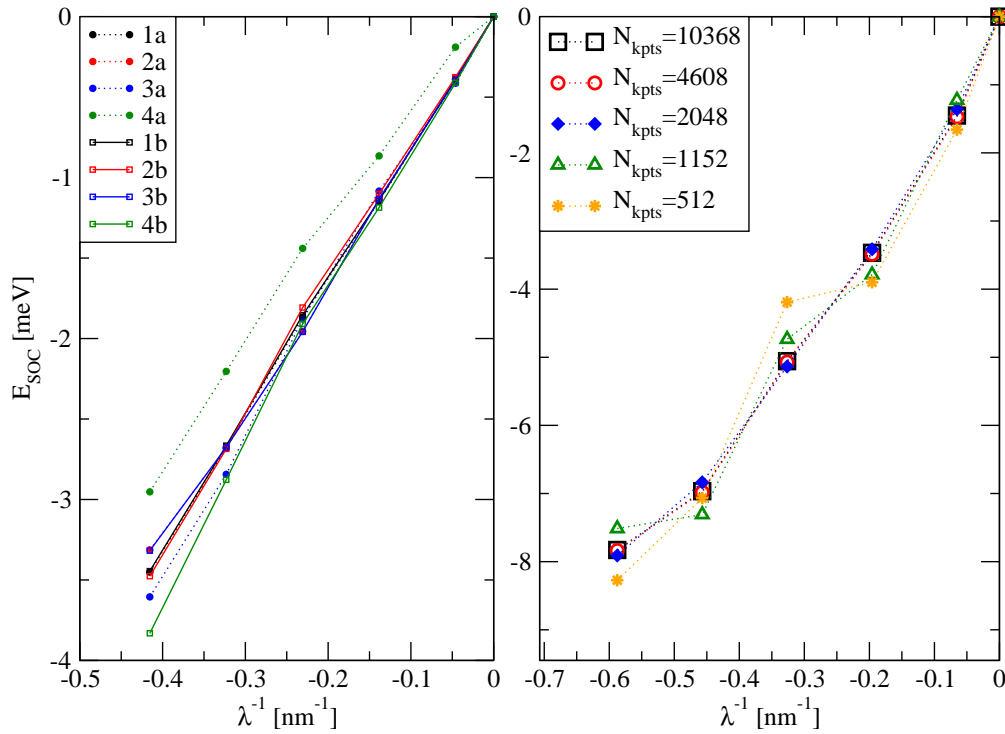

Figure 7.7: Energy due to spin-orbit coupling in spin spirals in first-order perturbation theory. Left: Different k-point distributions in the BZ were tested for spirals along [1$\bar{1}$0]. Right: Convergence with respect to the number of k-points for a mesh with $\rho = 1$ for spirals along [001].

Figure 7.8: Atom resolved spin-orbit energy for spin spirals along [001] with various period lengths λ. The labels count the atoms in the unit cell. Solid lines represent fits to the data. The data points are converged with respect to the k-point grid. The largest contributions come from the Cr (black) and first three W layers (blue).
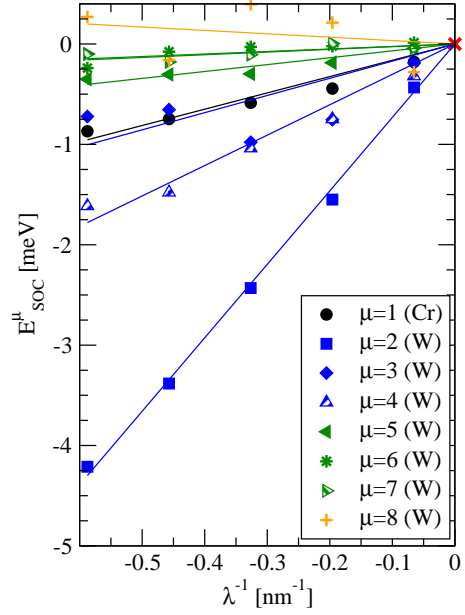
and 1b, respectively) are converged with respect to $\delta x/l_x$ and give the same SOC-energy up to 0.01 meV. For the other k-meshes with $\rho > 1$, the energies are not converged. The deviations in energy using two k-sets with same ρ increases as ρ increases, but this might also be due to the fact that the total number of k-points decreases as well.

To estimate which number of k-points of a homogeneously distributed k-point grid is sufficient, the same calculations as above were done with spin-spiral q-vectors pointing along [001]. Five k-point grids were used containing 512 to 10368 k-points. The plot in the right panel of figure 7.7 shows that at least 2048 k-points should be used. To make sure, that the k-point number is chosen high enough, we used the set with 4608 k-points for all the following calculations of this section and checked the convergence of the results by using the 2048 k-point set.

7.4.3 Layer-resolved analysis of the DMI

As seen in chapter 3.6.2, an atom-resolved change in energy can be obtained by applying SOC as perturbation in first-order perturbation theory. For each atom a curve $E_{\text{SOC}}^{\mu}(q)$ is obtained, where μ labels the atoms in the unit cell (cf. figure 7.8). In first-order perturbation theory, the symmetry

$$E_{\text{SOC}}^{\mu}(\mathbf{q}) = -E_{\text{SOC}}^{\mu}(-\mathbf{q}) \,, \tag{7.1}$$

holds if the changes in the occupation of the electronic states are small, as it is usually the case for W-substrates. Therefore, it is enough to calculate spin spirals of one rotational sense (e.g. $q \sim \lambda^{-1} < 0$). Linear fits of the form $E_{\text{SOC}}^{\mu} = D^{\mu} q$ give values for the contribution of the μth atom to the total Dzyaloshinskii-Moriya interaction $D = \sum_{\mu} D^{\mu}$. These fits are indicated as solid lines in figure 7.8.

To investigate the influence of the film thickness on D, the atom resolved analysis was also performed for slabs with 1 layer of Cr in 8 and 9 layers of W. The results for spirals along [001] are shown in figure 7.9. The left panel shows the values corresponding to the fits shown in figure 7.8 (filled bars). Values obtained with a film consisting of 1 layer Cr and 8 layers W are also shown (striped bars). The errorbar corresponds to the uncertainty in D^μ from the least square fit. The results for the two films agree quite well for layer 1-6. Additionally, the data was analyzed in a similar fashion, but only considering spin spirals with $|\lambda^{-1}| \leq 0.2\,\mathrm{nm}^{-1}$, because we are interested in spin spirals of very long period length. Two datapoints are sufficient to estimate a value and an error of D^μ. The results (shown in the right panel) contain also data from a film with 9 W layers. A slight enhancement of DMI compared to the fits containing spirals with $|\lambda^{-1}| < 0.6\,\mathrm{nm}^{-1}$ in layer 1, 2, 4 and 5 and a considerable enhancement in layer 3 is observed. Comparing the results from the 10-layers film to the others, the magnitude differs in layer 3 and 4, but the overall DMI (summing up layer 1 to 5) agrees quite well (see table 7.2).
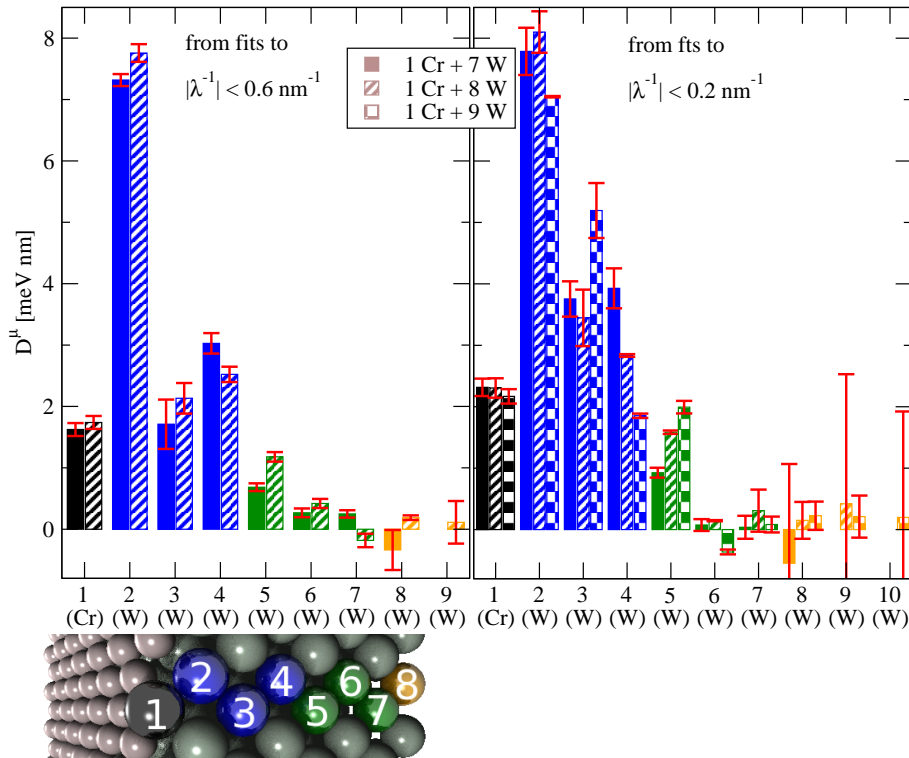

Figure 7.9: Layerwise contribution to D for spirals along [001]. The left panel shows the values from fits to five spin spirals for a film consisting of 8 and 9 layers. The right panel shows the values from fits to two spirals with $|\lambda^{-1}| \leq 0.2\,\mathrm{nm}^{-1}$, where additionally one more film with 10 layers was computed.
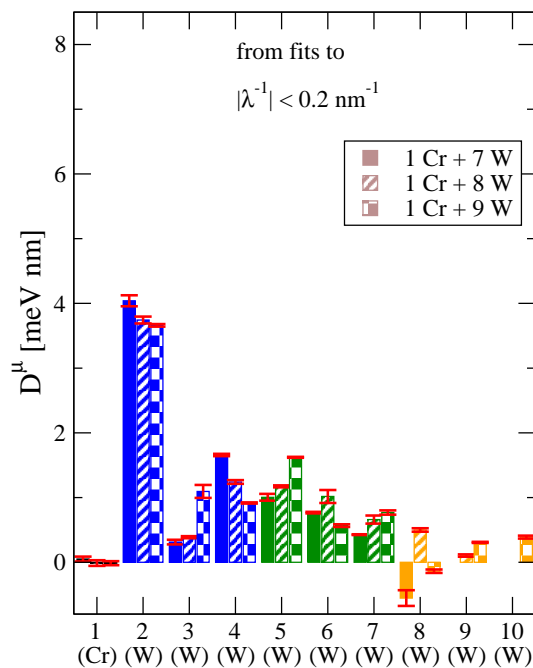
Figure 7.10: Same as in the right panel of figure 7.9 for spirals along $[1\bar{1}0]$.

[meV nm]	[001]		$[1\bar{1}0]$
	$\sum_{\mu=1}^{5} D^{\mu}$		$\sum_{\mu=1}^{7} D^{\mu}$
	fit 1	fit 2	fit 2
1+7 layer	15.2	19.9	8.5
1+8 layer	16.0	19.3	8.5
1+9 layer	–	19.0	8.8

Table 7.2: Results from the layer-resolved analysis of the DMI. Spirals with $|\lambda^{-1}| < 0.6\,\mathrm{nm}^{-1}$ and $|\lambda^{-1}| < 0.2\,\mathrm{nm}^{-1}$ (corresponding to 5 and 2 datapoints) were taken for fit 1 and 2, respectively.

Spin spirals along $[1\bar{1}0]$ have a smaller DMI, but the contribution seems to decay slower with increasing distance from the Cr-layer, so that contributions from more layers have to be taken into account (see figure 7.10). We took the first 7 layers to determine the total DMI, because the the results of the different layers agree nicely. Another difference to spirals along [001] is, that the uncertainties in D^{μ} are much smaller. Interestingly, the Cr-layer does not contribute significantly to the DMI in this direction.

Common for all slabs and both directions is, that the first W-layer contributes the most to DMI. Due to the high charge of the W-atoms, spin-orbit coupling is strong and already small magnetic moments (see chapter 7.3.1) are sufficient to cause a strong contribution to the DMI.
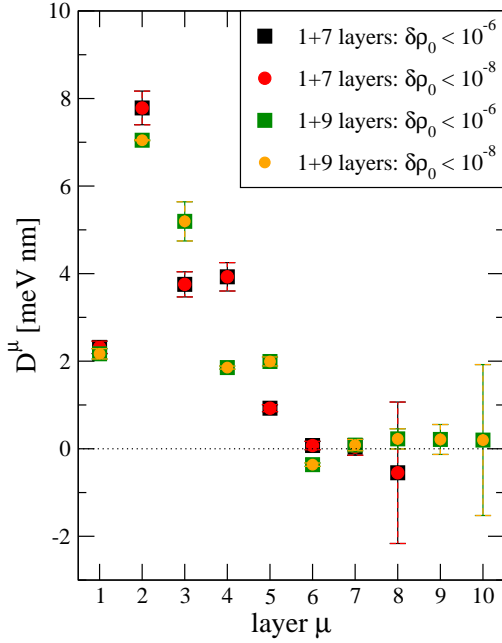
Figure 7.11: Layer-resolved DMI D^μ, obtained from spin-spiral calculations in [001]-direction using the force theorem with differently converged starting densities and two film thicknesses. The two curves for the 8 layer slab (black and red) and 10 layer slab (green and orange) are the same, so self-consist calculations converged to a distance of $10^{-6} \frac{\text{e}}{\text{a}_0{}^3}$ are sufficient.

Test of force theorem approximations

Only spin spirals with q-vectors parallel to [001] are considered in this section.

In the force theorem a collinear charge density is converged with relatively few k-points and then a single iteration with many k-points is done to determine the sum of single particle energies. Typically a distance in input- and output charge density of approximately $\delta\rho_0 = 10^{-6} \frac{\text{e}}{\text{a}_0{}^3}$ is sufficient to determine the Hartree and XC-potential for the force-theorem step and not all details of the charge density are needed to obtain good results. This was tested by comparing the results of a force-theorem calculation with a pre-converged density of distance in charge density $\delta\rho_0 < 10^{-6} \frac{\text{e}}{\text{a}_0{}^3}$ and $\delta\rho_0 < 10^{-8} \frac{\text{e}}{\text{a}_0{}^3}$, respectively. The DMI does not change (figure 7.11) and using a converged charge density up to $\delta\rho_0 < 10^{-6} \frac{\text{e}}{\text{a}_0{}^3}$ is enough.

Additionally, some spin spirals (without SOC) were computed self-consistently and then only the influence of SOC was treated as a perturbation (in first-order perturbation theory). This procedure is much more time consuming as the one explained above, because the charge density for each q-vector has to be obtained self-consistently. Therefore 512 k-points were used until the distance of input and output charge density was less than $10^{-6} \frac{\text{e}}{\text{a}_0{}^3}$. Afterwards SOC was included in first order perturbation theory, where 4608 k-points were used. As seen in the left panel of figure 7.12 it is valid to treat the change in the q-vector as a small perturbation – at least in the investigated range of q-vectors. For sure this approximation will fail when the calculated magnetic structure differs much from the (antiferromagnetic) structure of the converged density. Also in the layer-resolved contribution to the DMI the changes are negligible (see right panel of figure 7.12). We can also draw the conclusion that the "brutal" approximation in setting the interstitial magnetization to zero when the force theorem is applied (as explained in

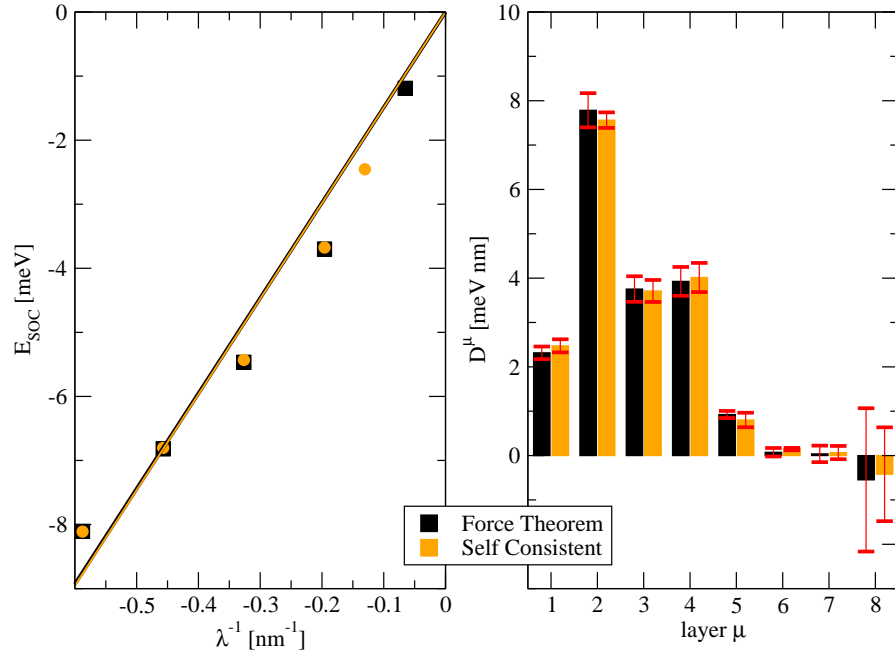chapter 6.2) does not influence the result.

Figure 7.12: Comparison between force theorem and self-consistent spiral calculations. Left panel: Spin-orbit contribution to the total energy from layers 1 to 7 and fits to the data yielding to the same value for D. Right panel: Layer-resolved DMI. The changes are negligible.

Concluding this test section one can say, that applying the force theorem is valid.

Influence of SOC on the starting density

In the calculations performed above, SOC is only included in the last iteration when the sum of single particle energies is calculated (force theorem step). However, the small influence on SOC on the (converged) density can induce sizable changes in the total energy (as observed in calculations of the magnetocrystalline anisotropy). Therefore a primitive rectangular unit cell with 2 atoms per layer was used to perform collinear self-consistent calculations including SOC, and afterwards the DMI was calculated according to the procedure explained above: the energies of 2 spin spirals were computed and linear fits of the form $E = D \cdot \lambda^{-1}$ were made to get the strength of DM-interaction. The spin-spiral q-vector was pointing in [001]-direction. Calculations were done for a starting density with a spin quantization axis pointing along the [001] and [110]-directions, respectively. The influence of SOC on the starting density is small for all layers (figure 7.13). However, in case of the 8 layers film, the total DMI gets enhanced by about 8% and for the 9 layer film it gets reduced by 2%, so estimating a trend for the inclusion of SOC in the convergency cycle can not be made. However, if one wants

to include SOC in the self-consistent calculations, the direction of the spin quantization axis does not matter.
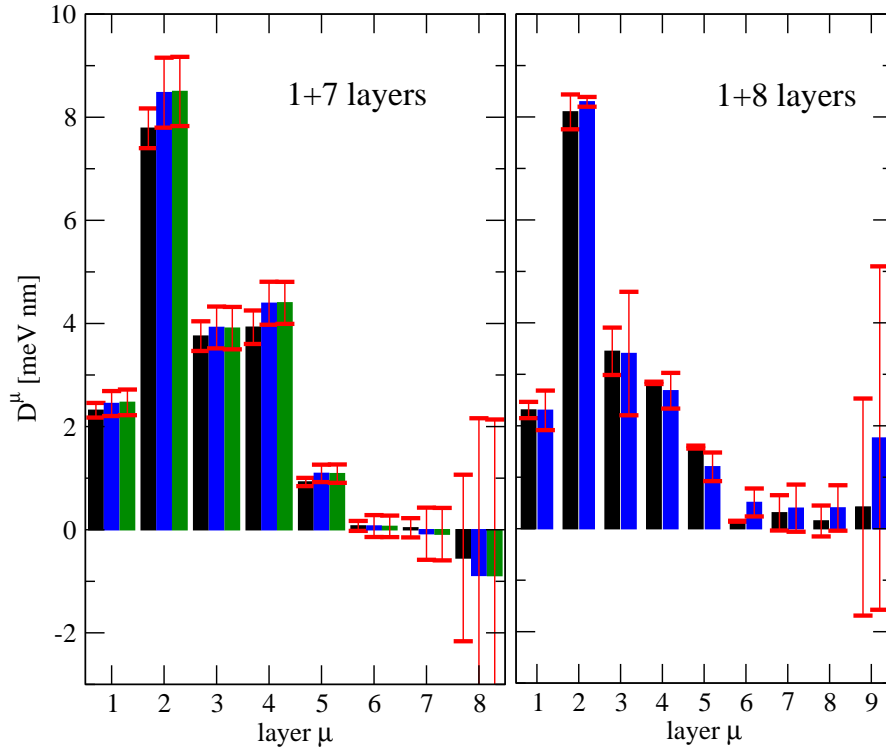

Figure 7.13: Converged charge densities which were obtained without SOC (black), with SOC and magnetization direction along [001] (blue) and [110] (green) were used to calculate the layer-resolved DMI. Calculations with 1+7 layers (left panel) show, that SOC enhances the DMI in layers 1 to 5 by about 8%, whereas the magnetization direction does not matter. For the 1+8 layers film (right panel), SOC reduces the total DMI in layer 1 to 5 slightly by 2%.

7.5 Calculation of the spin stiffness

The spin-stiffness constant is calculated in this section. It is dominated by non-relativistic effects and thus calculations can be done without SOC (i.e. in scalar-relativistic approximation), which reduces the computational effort a lot since in this case the generalized Bloch theorem allows calculations in the chemical unit cell. The dispersion relation is of the form

$$E_{\text{SR}} = \tilde{A}\,(\Delta q)^2 + \text{const} = A\,\lambda^{-2} + \text{const}\,, \tag{7.2}$$

where A is the spin-stiffness constant. This approximation is only valid for small deviations from the antiferromagnetic state ($\Delta q = 0$), and for larger values of Δq corrections to this approximation are expected.

7.5.1 Convergence with k-point number

In the left panel of figure 7.14 the energies of spin spirals with different period lengths are shown (please notice, that λ^{-2} is chosen as scale of the abscissa). A parabolic curve would appear as straight line in this plot, as indicated by a solid line which represents a fit of the form (7.2) to the data calculated with 2048 k-points giving a value of $A \approx 130\,\text{meV}\,\text{nm}^2$. Additionally, an oscillatory energy contribution in $\Delta q \sim \lambda^{-1}$ occurs, as can be seen from the residuals $\Delta E = E_{\text{fit}}(\lambda) - E_{\text{SR}}(\lambda)$ to the presented fit (black circles in the upper right panel). Also when the number of k-points is increased, the residuals retain their magnitude and oscillation period. Please notice that for each k-point set, a fit to the data was performed and the residuals were calculated with respect to this fit (although only the fit to the 2048 k-point mesh is shown).

However, if we take the value for the spin stiffness from the fit presented in figure 7.14, $A \approx 130\,\text{meV}\,\text{nm}^2$, and determine the pitch of the established spin spiral (approximation of homogeneous spirals in the micromagnetic model with $D = 19.9\,\text{meV}\,\text{nm}$), we find $|\lambda| = |2A/D| \approx 13\,\text{nm}$ (15.4 nm was found in the experiment, indicated by the green arrow). This is a long pitch corresponding to spirals reaching over approx. 40 unit cells and small q-vectors ($\Delta q \approx 0.02$). Please notice, that a strong anisotropy, K, can also influence the shape and the period length of a spin spiral, but the assumption of homogeneous spirals shall be enough to estimate the region of Δq, in which we are interested.

To resolve the correct behavior in this regime of small q-vectors, the number of k-points has to be very high as well. This can be seen in the zoomed in region (lower right panel of figure 7.14. We notice that the calculated energy depends strongly on the k-grid for small λ^{-2} when the number of k-points is chosen too low: For $\lambda = 1/\sqrt{3.2 \cdot 10^{-2}}\,\text{nm}$ (data points most to the right) the 4 energies obtained with the different k-point meshes are the same. However, for $\lambda = 1/\sqrt{2.8 \cdot 10^{-2}}\,\text{nm}$ mesh with 2048 k-points gives an imprecise energy while the other meshes give consistent results. The next denser k-point mesh (4608 k-points) gives another small deviation from the other data at $\lambda = 1/\sqrt{0.8 \cdot 10^{-2}}\,\text{nm}$, whereas the two sets with the highest number of k-points remain consistent for the investigated spirals. (Please notice that the antiferromagnetic ordering ($\lambda^{-1} = 0$) was chosen as origin of energy for each k-point mesh.) Thus at least 4608
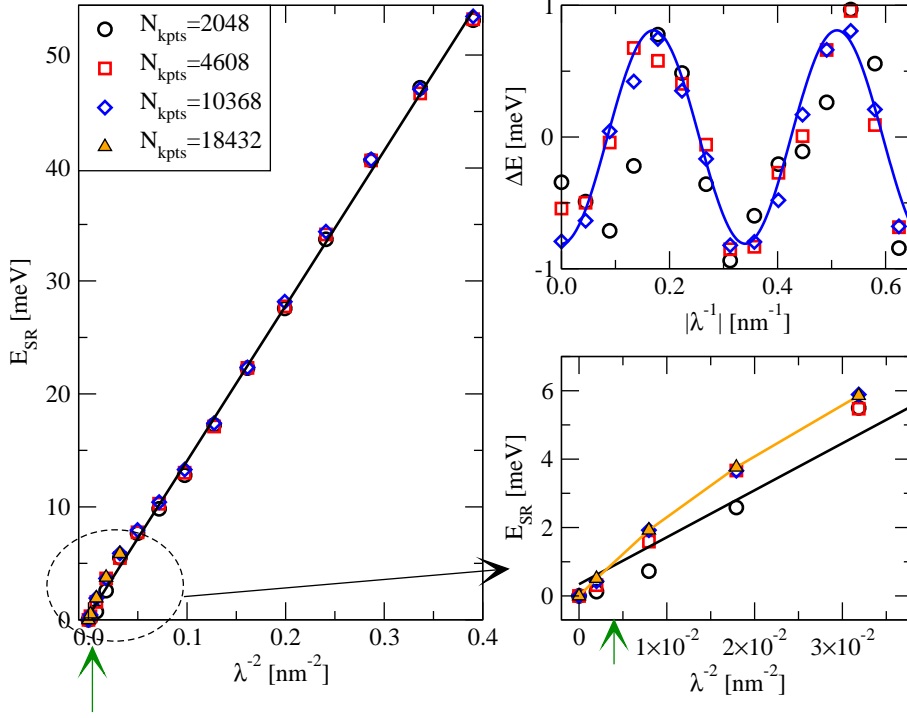
Figure 7.14: Total energy calculations in scalar-relativistic approximation for spin spirals along the [001]-direction. Left panel: dispersion relation for different k-point meshes (symbols) and a fit according to eq. 7.2 to the data obtained with 2048 k-points (solid line). The green arrow indicates the region of interest (corresponding to the period length which is found in the experiment). Lower right panel: zoom into the region of very long spirals. The orange line connects the data obtained with the very dense k-point mesh (18432 k-points). Upper right panel: symbols represent the residuals from fits and the blue line represents the curve $\Delta E = -0.8\,\mathrm{meV}\,\cos(\frac{2\pi\,2.9\,\mathrm{nm}}{\lambda})$.

k-points must be chosen to give reliable results for small q-vectors, better are about 10000 k-points.

The same analysis was done for spirals along the long axis of the two-dimensional unit cell 7.15. Similar features are obtained, e.g. the oscillatory modulation, many k-points are needed to describe the spin stiffness for small q-vectors correctly. In contrast to the [001]-direction the spin stiffness is smaller (corresponding to the smaller slope of the fit yielding a spin stiffness $A \approx 110\,\mathrm{meV\,nm^2}$). We can again estimate the pitch by assuming homogeneous spirals with $D = 8.5\,\mathrm{meV\,nm}$, giving $\lambda \approx 25\,\mathrm{nm}$. This corresponds to a spiral over 60 unit cells and is also in the regime of very small q-vectors ($\Delta q \approx 0.02$).

71

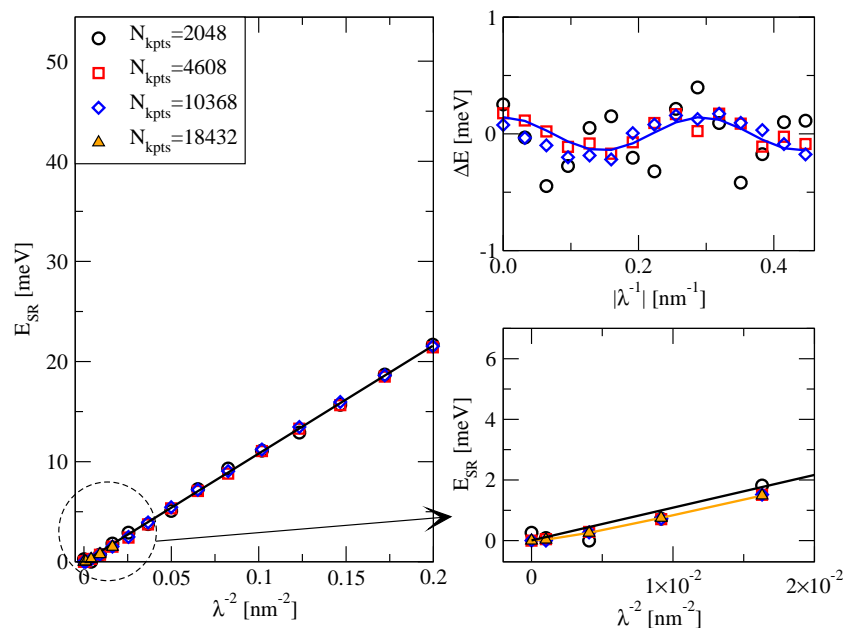Figure 7.15: Energies of spin spirals along $[1\bar{1}0]$ in analogy to figure 7.14. Residuals follow a curve of the form $\Delta E = 0.14\,\mathrm{meV}\,\cos(\frac{2\pi\,3.4\,\mathrm{nm}}{\lambda})$.

7.5.2 Oscillatory deviations from a parabolic dispersion

The remaining question is, whether the oscillatory deviations are a numerical artifact or a physical effect in the system. In calculations of monowires (in FLAPW [50] and tight binding [51]) oscillatory numerical artifacts were observed, but their amplitude decreased with increasing number of k-points, whereas the oscillations observed here do not.

We also did force theorem calculations of spin spirals in the 2-atomic unit cell, which allows us to compute spirals with a cone angle θ. If we choose $\theta = 0$, the energy is expected to be independent of the spin-spiral vector $\mathbf{q}$, because the magnetic structure is antiferromagnetic in any case. However, we find an oscillation with an amplitude of $5\,\mathrm{meV}$ (see figure 7.16), which must be of numerical origin. The amplitude and the length of the oscillation decrease when a denser k-mesh is used.

So, the oscillations observed in figures 7.14 and 7.15 might depend on other parameters than the k-point meshes, e.g. the muffin-tin radius, the plane-wave cutoff, or they are arising from the fact, that the interstitial magnetization is set to zero in the force theorem step (cf. chapter 6.2). Further checks would be necessary to determine the origin of the oscillations. However, we did not do that, but first assume that the oscillations are not physical (as we also do not have a model which describes them) and determine the spin stiffness accordingly in the next section. Additionally we describe the changes in the spin stiffness as if the oscillations were of physical origin and employ the impact on the established spin spiral.
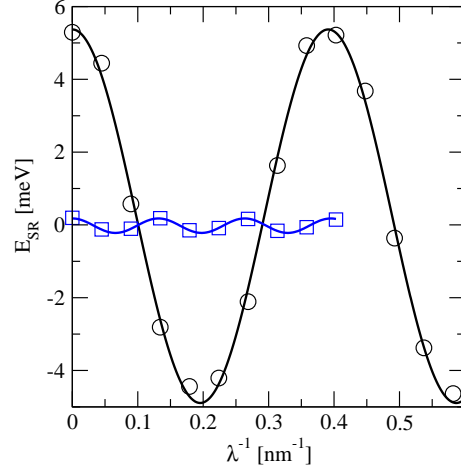
Figure 7.16: Spin-spiral energies with a cone angle $\theta = 0$, computed with 1024 (black circles) and 2304 (blue squares) k-points. The energy is expected to be constant, but oscillations are observed which decrease with increasing number of k-points. Solid lines represent curves of the form $E_{\mathrm{SR}} = (0.2 + 5.1 \cos(16.1 \, \mathrm{nm}/\lambda)) \, \mathrm{meV}$ (black) and $E_{\mathrm{SR}} = (0.0 + 0.2 \cos(47.6 \, \mathrm{nm}/\lambda)) \, \mathrm{meV}$ (blue) obtained by least square fits.

7.5.3 Spin stiffness from a quadratic fit

Due to the considerations before, we fit the data by a function

$$E_{\mathrm{SR}} = A \, \lambda^{-2} + a_0 \, \cos(2\pi \, a_1 \lambda^{-1}) + \mathrm{const.} \qquad (7.3)$$

We find the following parameters:

$$A = 135 \, \mathrm{meV \, nm^2} \, , \; a_0 = -0.8 \, \mathrm{meV} \, , \; a_1 = 2.9 \, \mathrm{nm} \; \text{ for } \mathbf{q} \parallel [001]$$
$$A = 112 \, \mathrm{meV \, nm^2} \, , \; a_0 = 0.16 \, \mathrm{meV} \, , \; a_1 = 3.5 \, \mathrm{nm} \; \text{ for } \mathbf{q} \parallel [1\bar{1}0]$$

We neglect the cosine part in the model because we assume it to be of numerical origin and take A as spin stiffness constant. Taking also the Dzyaloshinskii-Moriya interaction into account ($D_{001} = 19.9 \, \mathrm{meV \, nm}$ and $D_{1\bar{1}0} = 8.5 \, \mathrm{meV \, nm}$) and assuming homogeneous spirals as a first approximation, we can estimate a period length for the spin-spiral ground state $\lambda_{[001]} \approx 14 \, \mathrm{nm}$ and $\lambda_{[1\bar{1}0]} \approx 26 \, \mathrm{nm}$.

7.5.4 Spin stiffness including the oscillatory deviations

However, if we would take the oscillatory part into account, the spin stiffness depends on the period length λ as well. The region of interest can be approximated from the values obtained by neglecting the oscillations. We perform fits of the following form to the dispersion curve of spirals with $\lambda^{-2} < 3.5 \cdot 10^{-2} \, \mathrm{nm^{-2}}$ for [001]-direction and $\lambda^{-2} < 2 \cdot 10^{-2} \, \mathrm{nm^{-2}}$ for [1$\bar{1}$0]-direction:
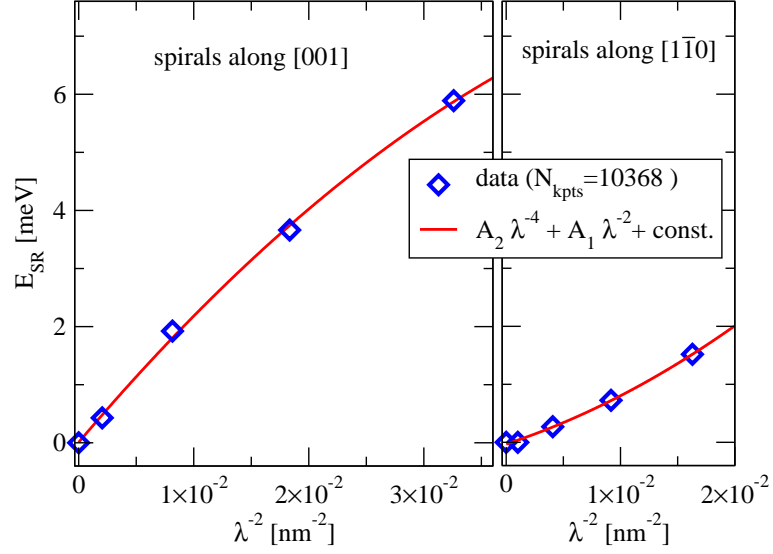
Figure 7.17: 4th order fit to the small λ^{-1} regions shown in figures 7.14 and 7.15. The energy dispersion relation is well described by a fit of the form of equation (7.4) in the region of spirals with very long period length.

$$E_{\text{SR}}^{(2)} = A_2\,\lambda^{-4} + A_1\,\lambda^{-2} + \text{const.} \tag{7.4}$$

The following parameter are obtained:

	$\mathbf{q}\,\|\,[001]$	$\mathbf{q}\,\|\,[1\bar{1}0]$
$A_1\,[\text{meV nm}^2]$	246 ± 11	69 ± 12
$A_2\,[\text{eV nm}^4]$	-2.0 ± 0.3	1.6 ± 0.7

The data in this region of long period lengths is described very nicely by this fit, as can be seen in figure 7.17.

Taking also the Dzyaloshinskii-Moriya interaction into account and assuming homogeneous spin spirals, we can compute the period length λ_0 and the energy gain E' (neglecting the anisotropy energy, which is independent from λ_0 in this approximation) for the model by finding the energy minimum,

$$\left.\frac{\partial E^{(2)}}{\partial \lambda}\right|_{\lambda=\lambda_0} = \lambda_0^{-2}\left(-4\,A_2\,\lambda_0^{-3} - 2\,A_1\,\lambda_0^{-1} - D\right) = 0\,. \tag{7.5}$$

We find the following values:

	$\mathbf{q}\,\|\,[001]$		$\mathbf{q}\,\|\,[1\bar{1}0]$	
	$\lambda_0\,[\text{nm}]$	$E'\,[\text{meV}]$	$\lambda_0\,[\text{nm}]$	$E'\,[\text{meV}]$
from eq. (7.4)	-23	-0.4	-18	-0.3
neglecting oscillations	-14	-0.7	-26	-0.2

The dependence of the final result on the choice of the model is not huge. The value of λ lies in any case in the region investigated above, which makes the analysis self-consistent.

We can alternatively rewrite (7.4) to

$$E_{\text{SR}} = \underbrace{\left(A_2\,\lambda^{-2} + A_1\right)}_{A'(\lambda)}\,\lambda^{-2} \tag{7.6}$$

and define an effective spin stiffness A'. Its dependence on λ is small for long period lengths: We find

$$
\begin{aligned}
225 < \quad & A'_{[001]} \quad < 245 \;(\text{meV nm}^2) \text{ and} \\
85 > \quad & A'_{[1\bar{1}0]} \quad > 70 \;(\text{meV nm}^2) \text{ for} \\
10 < \quad & |\lambda| \quad < 30 \;(\text{nm}),
\end{aligned}
$$

so the difference is comparable to the uncertainty in A_1. However, the spin stiffness A' is notably enhanced compared to A (which is obtained neglecting the oscillatory part in the energy dispersion) in the case of $\mathbf{q}$ along [001], because the oscillatory deviations start in a valley for $\Delta q \approx 0$ and the average slope gets an additional positive contribution. For the [1$\bar{1}$0]-direction A' is reduced compared to A, because the oscillations start at a hill and oscillatory residuals add a negative value to the slope. We finally estimate the spin stiffness for both directions by evaluating

$$
\begin{aligned}
A' = (242 \pm 10)\,\text{meV nm}^2 \quad & \text{at } \lambda_0 = -23\,\text{nm}\,,\; \mathbf{q} \parallel [001] \text{ and} \\
A' = (74 \pm 10)\,\text{meV nm}^2 \quad & \text{at } \lambda_0 = -18\,\text{nm}\,,\; \mathbf{q} \parallel [1\bar{1}0]\,.
\end{aligned}
$$

7.6 Calculation of the anisotropy

In this part, we consider the magnetocrystalline anisotropy (MCA). Two effects contribute to the MCA, namely (a) the spin-orbit coupling (SOC) and (b) the magnetostatic dipole-dipole interaction. The bcc(110) structure possesses two mirrorplanes which are perpendicular to each other. As shown in chapter 4.3, the corresponding anisotropy tensor is diagonal and possible extrema of the anisotropy energy are the high symmetry directions.

The classical dipole-dipole energy is calculated for magnetization directions parallel to the three high symmetry directions according to equation 4.14. The spin moments obtained from the FLAPW calculations were taken as total magnetic moment, because the contribution from the orbital moments is small and can be neglected (cf. section 7.3.1). The anisotropy energies are

$$K_{[001]}^{\mathrm{dip}} = 0.035 \, \mathrm{meV} \; \text{and} \; K_{[1\bar{1}0]}^{\mathrm{dip}} = 0.055 \, \mathrm{meV} \; \text{(per surface atom)},$$

i.e. the dipole-dipole interaction favors out-of-plane magnetization.

The contribution from SOC to the MCA must be calculated quantummechanically, thus the FLEUR code [13] is used. Because the anisotropy energy cannot be obtained by treating SOC in first-order perturbation theory (this contribution is zero), higher order terms must be considered: This is done by including SOC in a self-consistent collinear calculation, which requires a primitive rectangular unit cell containing two atoms.

The lowest order of change in energy of a state n (according to the Rayleigh-Schrödinger Perturbation Theory) is of the form

$$\Delta E_n = \sum_{n'} \frac{\left| \langle \psi_n^0 \, | \mathcal{H}_{\mathrm{SO}} | \, \psi_{n'}^0 \rangle \right|^2}{E_n^0 - E_{n'}^0} \, , \tag{7.7}$$

where the superscript ^{0} denotes the solution without SOC, n denotes an occupied state and the sum over n' is over all unoccupied states [43]. It can be seen, that the main contribution to the SOC-energy comes from states around the Fermi energy where the denominator becomes small. Therefore, it is important to calculate the occupation around the Fermi level precisely and the temperature broadening, which is introduced to obtain convergence of the system, has to be low. In our case $k_{\mathrm{B}}T = 0.0001 \, \mathrm{htr}$ was chosen. The other parameters were set according to chapter 7.3.

We did different types of calculations to obtain the anisotropy energies.

1. We started from a converged charge density (in scalar-relativistic approximation) and converged further with SOC and magnetization

   a) in [001]-direction (results are labeled "FT$_{001}^{7\mathrm{W}}$") and

   b) in [110]-direction ("FT$_{110}^{7\mathrm{W}}$")

   using 256 k-points in the 2DBZ (it is half the size of the 2DBZ of the centered rectangular unit cell), until the distance between input and output charge density was less than $10^{-6} \frac{\mathrm{e}}{\mathrm{a}_0^3}$. However, SOC effects were not considered in the muffin-tin

N_{kpts}	$K_{[001]}^{SOC}$				$K_{[1\bar{1}0]}^{SOC}$			
	FT$_{001}^{7W}$	FT$_{110}^{7W}$	FT$_{001}^{8W}$	SC^{7W}	FT$_{001}^{7W}$	FT$_{110}^{7W}$	FT$_{001}^{8W}$	SC^{7W}
576	0.78	–	–	–	1.14	–	–	–
1024	0.95	–	–	1.00	1.24	–	–	1.56
1600	–	–	–	0.80	–	–	–	–
2304	0.92	0.93	1.06	0.86	1.18	1.20	1.21	1.28
4096	0.91	0.93	–	0.83	1.13	1.15	–	–

Table 7.3: Calculated anisotropy energies in meV per surface atom. See text for further details.

of the W atom at the lower surface of the Cr covered film, because its enhanced magnetic moment due to the lower coordination number may cause an artificial contribution to the MCA.

Afterwards a single iteration was done using many k-points (force theorem) and magnetization pointing along the high symmetry directions [001], [110] and [1$\bar{1}$0], respectively. One can safely say, that 1024 k-points are enough to compute the anisotropy energy and that the magnetization direction of the converged density has no influence (see table 7.3 for the numbers).

2. We did force theorem calculations (as above) with a film consisting of (1+8) layers (results are labeled "FT$_{001}^{8W}$"). For the converged charge density, a magnetization direction along [001] was chosen. Parameters were the same as above. The results agree within 10%.

3. Obtaining converged results for the anisotropy is cumbersome because calculations are long but straight forward: Charge densities were converged with magnetization in all three high symmetry directions (results are labeled "SC^{7W}") using the (7+1) layers film. From the results on $K_{[001]}$ one sees, that 1600 k-points are needed to obtain converged results. The values also agree within 10% comparing to force theorem calculations of the film with the same thickness.

To summarize the results: it is hard to determine the anisotropy precisely, because the anisotropy energies are very small quantities and one needs high cutoffs and thus high computational power to obtain reliable results. However, all the different approaches determined the easy axis to be out-of-plane and the hard axis to be in-plane [1$\bar{1}$0]. We determined the anisotropy constant to $K_{[001]} = (0.9 \pm 0.1)$ meV and $K_{[1\bar{1}0]} = (1.2 \pm 0.1)$ meV, where the classical dipole-dipole interaction plays a minor role: its contribution is even smaller than the uncertainties in K^{SOC}.

7.7 Predicted spin spiral and comparison to an experiment

We want to conclude this chapter by comparing the model parameters for the two crystallographic directions and discuss the resulting spirals.
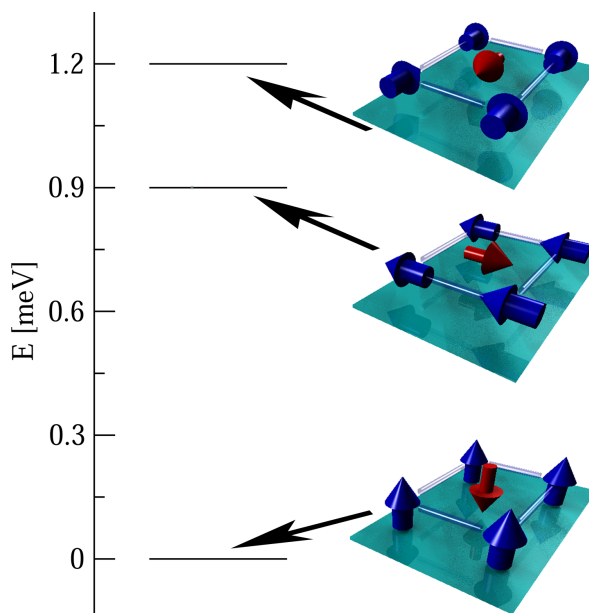
Figure 7.18: Anisotropy energies per surface atom. The easy axis is out-of-plane.

	A	D	K	κ	λ	λ_{hs}
	[meV nm^2]	[meV nm]	[meV]		[nm]	[nm]
[001]	135	19.9	0.9 ± 0.1	0.5	-14.3	-13.5
[1$\bar{1}$0]	112	8.5	1.2 ± 0.1	3.0	$-$	-26.4

Table 7.4: Model parameter from *ab-initio* calculations and resulting properties of inhomogeneous spirals for both crystallographic directions. For comparison also the period length of homogeneous spirals, λ_{hs}, is given.

A spin spiral along [001]-direction fulfills the criterion for establishing a spin-spiral ground state ($\kappa < 1$, cf. table 7.4). The profile is shown in figure 7.19. The period length is not very sensitive to the anisotropy, K:

K [meV]	κ	λ [nm]
0.8	0.45	-14.29
0.9	0.50	-14.31
1.0	0.55	-14.46

These values are only slightly enhanced as compared to the period length of homogeneous spirals $\lambda_{\mathrm{hs}} = -13.5$ nm. The energy gain per surface atom (for homogeneous spirals) is approximately (0.28 ± 0.05) meV. Thus, the Dzyaloshinskii-Moriya interaction is strong enough to create a left rotating (indicated by the minus-sign in λ) cycloidal spin spiral along [001]. This is still the case, if the oscillatory deviations to a parabolic dispersion in the determination of the spin stiffness are not neglected, resulting in $\kappa = 0.9$

and $\lambda = -25\,\text{nm}$.

In contrast to this, the Dzyaloshinskii-Moriya interaction is not strong enough to create a spiraling ground state along the $[1\bar{1}0]$-direction, because the DMI is too weak to compete against K and A ($\kappa > 1$, in both cases, neglecting and considering the oscillations in A).
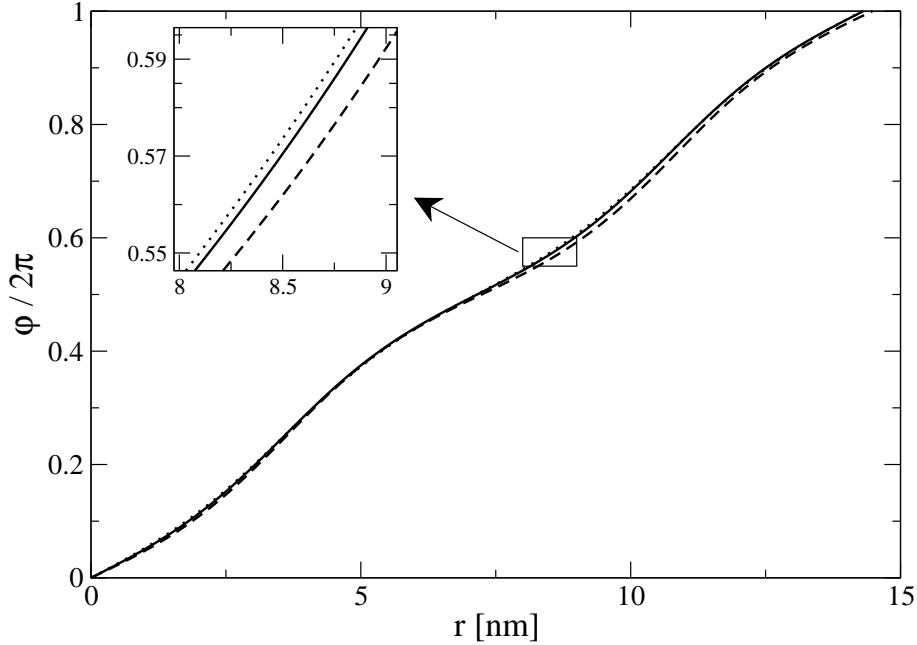

Figure 7.19: Profile of inhomogeneous spin spirals with $A = 135\,\text{meV}\,\text{nm}^2$, $D = 19.9\,\text{meV}\,\text{nm}$ and $K = (0.8,\, 0.9,\, 1.0)\,\text{meV}$, resulting in $\kappa = 0.45$ (dotted line), 0.50 (solid) and 0.55 (dashed). The period length is not very sensitive to K.

Our findings agree with these of an SP-STM experiment, as shown in figure 7.20. Let us first explain, how such a picture is obtained and what it shows. The tunneling current from the (spin-polarized) tip to the sample has, beside its normal distance dependent part I_0, also a contribution depending on the magnetization of the sample,

$$I = I_0 + I_{\text{sp}}\,\mathbf{m}_\text{T} \cdot \mathbf{m}_\text{S}\,, \tag{7.8}$$

where $\mathbf{m}_\text{T}$ and $\mathbf{m}_\text{S}$ are the unit vectors of magnetization of tip and sample, respectively.

The SP-STM picture shown in figure 7.20 reveals some remarkable features: first of all, the big spots show that it is not easy to grow a clean monolayer of Cr on the substrate. Secondly, fine stripes along the [001]-direction correspond to an antiferromagnetic ordering of magnetic moments, because they are only visible with a magnetic tip. Additionally, we see a modulation of contrast along this direction. Lines of low contrast, which are denoted by arrows, appear regularly in a distance of 7.7 nm. Possible explanations for such a modulation can be charge-density waves or spin spirals. In case
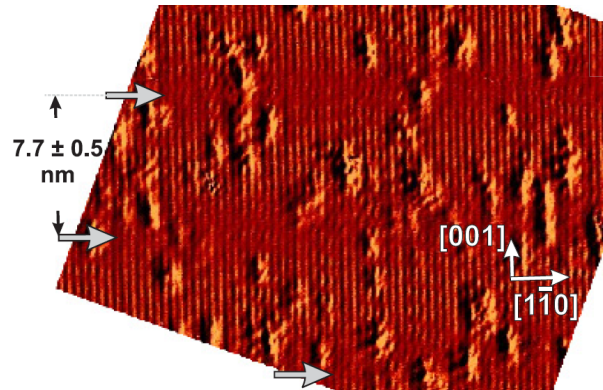
Figure 7.20: Measured SP-STM image of a monolayer Cr on W(110). The local anti-
ferromagnetic order reveals as stripes along [001]-direction. An additional
weak modulation of contrast is obtained. From [48].

of a spin spiral, the revealed modulation length of contrast would correspond to half of the spin-spiral period length.

We can now explain that the observed modulation indeed corresponds to a spin spiral. Not only the direction of propagation along [001] agrees between theory and experiment, but also the modulation length of (15.4 ± 1) nm (experiment) and 14.3 nm (theory) agrees very nicely.

8 Comparison to other thin-film systems

	Cr	Mn [1]	2 Fe [2]
A_{001} [meV nm^2]	135	$\star$	165
D_{001} [meV nm]	19.9	$\star$	-3.6
K_{001} [meV]	0.9	2.8	0.10
$A_{1\bar{1}0}$ [meV nm^2]	112	94.2	143
$D_{1\bar{1}0}$ [meV nm]	8.5	23.8	3.1
$K_{1\bar{1}0}$ [meV]	1.2	1.2	0.21

Table 8.1: Model parameter from DFT calculations for the system of a monolayer of Cr (this thesis), a monolayer of Mn (results taken from Ref. [3]) and a double layer of Fe (from Ref. [7] and [2]) on a W(110) substrate. The $\star$ means that the micromagnetic model (5.5) was not applicable to the system.

Finally, we want to compare our results to the thin film systems of a double layer of Fe and a monolayer of Mn on a W(110) substrate. Both systems were studied by DFT-calculations and SP-STM measurements.

In Mn on W(110), a strong DMI of $D_{1\bar{1}0} = 23.8$meV nm for spin spirals along the [1$\bar{1}$0]-direction was discovered (c.f. table 8.1), which creates a spiraling ground state with a comparable period length to the Cr/W(110) system (8 nm for Mn vs. 14 nm for Cr). A value of $\kappa = 0.3$ shows, that the spiral is less inhomogeneous than the predicted spirals in Cr/W(110). Additionally, the propagation direction is different, but the rotational sense and type are the same as in Cr/W(110) (namely left-rotating cycloidal spirals). Model parameters from DFT calculations could not be obtained for Mn/W(110) in the [001]-direction, because the micromagnetic model was not applicable to the obtained energy dispersion. DFT calculations show that a spin spiral would be energetically less favorable than in the one in the [1$\bar{1}$0]-direction [3]. In SP-STM measurements a modulation of magnetic contrast was observed along the [1$\bar{1}$0]-direction with a period of 12 nm.

In the double layer Fe on W(110), the DMI is too weak to compete against the anisotropy and spin stiffness ($\kappa_{001} \approx 2$ and $\kappa_{1\bar{1}0} \approx 5$) [7]. However, the parameters obtained explain the regular formation of right-rotating (indicated by the minus-sign of D_{001}, cf. table 8.1) Néel-type domain walls normal to [001], as it is also observed experimentally [2].

The following table summarizes the experimental and theoretical results of 3d transition metals on W(110):

	rot. dir.	prop. dir.	λ_{theo}	λ_{exp}
Cr	left-handed	[001]	$14\,\text{nm}$	$15.4\,\text{nm}$
Mn	left-handed	[1$\bar{1}$0]	$8\,\text{nm}$	$12\,\text{nm}$
2 Fe	right-handed	[001]	$\rightarrow \infty$	$\rightarrow \infty$

Finally, we also compare the layer resolved contributions to the DMI in these systems (see figure 8.1). In each system, the largest contribution to the total DMI can be addressed to the W interface layer. This is due to the induced spin- and orbital moments in combination with the high charge of the W-nuclei resulting in a large spin-orbit coupling strength. In Cr, the most relevant contributions come from the first four (1 Cr +3 W) layers. In the system 2 Fe/W(110), the most relevant contributions come from the first five (2 Fe +3 W) layers, but they are of alternating sign and thus partly canceling each other. For Mn, only layer-resolved results for a film consisting of 4 layers was available obtained in first order perturbation theory [14]. We can notice, that the magnitude of the W contributions is quite high, but the detailed profile of the magnitudes (and even the sign) will probably change much depending on the number of W layers.
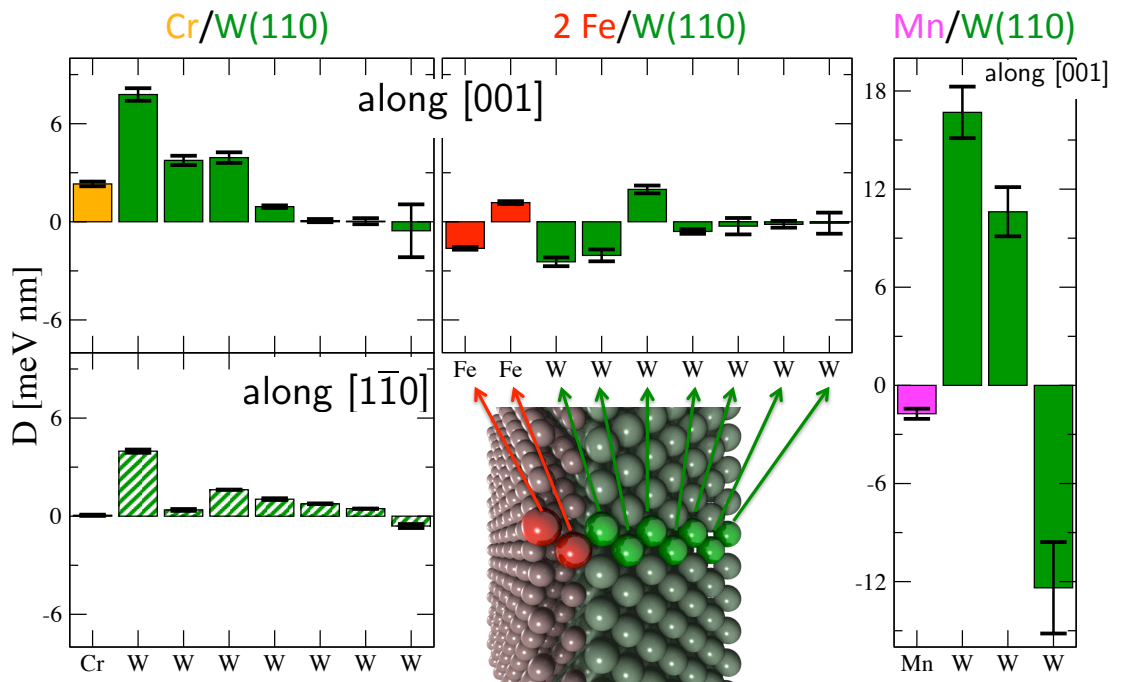

Figure 8.1: Layer resolved analysis of the DMI for different systems and crystallographic directions. Notice, that in the case of Mn only a 4-layer slab was used and thus these results can only to a certain extend be compared to the Cr and Fe calculations.

9 Summary

In this thesis, we have investigated the magnetic interactions in the thin film systems of a Cr monolayer on W(110) by means of density functional theory (DFT) in the FLAPW method. We found, that the Dzyaloshinskii-Moriya interaction is strong enough to create a left-rotating spin spiral along the [001]-direction with a period length of about 15 nm, which is in excellent agreement with the experiment by Santos et al. [48] .

We determined the ground state of the system in a micromagnetic model containing the following three interactions: the spin stiffness, Dzyaloshinskii-Moriya interaction (DMI) and the magnetocrystalline anisotropy (MCA). The strength of each of these interactions was obtained by DFT calculations employing the FLAPW method as implemented in the FLEUR code.

We calculated the energy of spin spirals with various period lengths in the scalar-relativistic approximation to determine the spin stiffness from quadratic fits to the energy dispersion. To obtain the strength of the Dzyaloshinskii-Moriya interaction (DMI), the inclusion of spin-orbit coupling (SOC) in a spin-spiral calculation is crucial. Therefore, a recently implemented method [14] was used, which treats SOC in first order perturbation theory. This method allows for fast calculations in the chemical unit cell and additionally provides the possibility to obtain an atom-resolved analysis of the Dzyaloshinskii vector $\mathbf{D}$. Additionally, both contributions to the MCA were determined: the effects due to SOC were determined with collinear self-consistent calculations, and the long range dipole-dipole interaction was treated by a classical model.

Special care was taken in the determination of the DMI and MCA, e.g. the dependence on the number of W layers and the most important cutoff-parameters as investigated. We were able to show that the main contribution to the DMI arises from the W interface layer, as it also occurs in the systems of a Mn monolayer on W(110) or a Fe double layer on W(110). The MCA favors a out-of-plane magnetization. In the study of the spin stiffness, we found an oscillatory energy contribution with an amplitude of 1 meV on top of the quadratic energy dispersion. The oscillatory behavior was independent of numerical cutoff parameters, e.g. the number of k-points, with which the Brillouin zone is sampled. However, more tests have to be performed to determine whether these oscillations are of numerical or physical origin. If they are assumed to be of physical origin, the value of the spin stiffness changes remarkably in the limit of spin spirals with long period lengths.

Nevertheless, we could show that the DMI is strong enough to compete against the spin-stiffness and MCA in both cases, favoring a left-rotating cycloidal spin spiral along the [001]-direction. The relatively strong MCA results in an inhomogeneous profile of the spiral. Both, the propagation direction and period length agree with experimental results, as it is also the case for other $3d$-transition metals on a W(110) substrate, which

are reported in literature so far. However, spin spirals in the systems investigated so far are not always qualitatively the same: they may differ in their rotational sense and/or in their propagation direction. In monolayer systems a left-rotating spiraling structure seem to be favored, as found for Cr/W(110) (this work), Mn/W(110) [3] and Mn/W(001) [6]. However, the DMI in a double layer Fe/W(110) [2,7,8] prefers the other rotational sense (right-rotating), as it was also recently predicted for a double layer Mn/W(110) [52]. However, the basic mechanism underlying the DMI which determines the rotational sense, the propagation direction and the strength (also the atom-resolved profile) is still poor understood and more insight into this complex phenomenon may be obtained by the systematic study of more thin film systems.

Danksagungen

Während meiner einjährigen Arbeit habe ich von verschiedensten Seiten Unterstützung erfahren, für die ich sehr dankbar bin.

Bibliography

[1] S. Blügel and G. Bihlmayer, Magnetism of Low-dimensional Systems: Theory, Handbook of Magnetism and Advanced Magnetic Materials, ed. H. Kronmüller and S. Parkin, Wiley, New York, 2007.

[2] A. Kubetzka, M. Bode, O. Pietzsch, and R. Wiesendanger, Spin-Polarized Scanning Tunneling Microscopy with Antiferromagnetic Probe Tips, Phys. Rev. Lett. **88**, 057201 (2002).

[3] M. Bode, M. Heide, K. von Bergmann, P. Ferriani, S. Heinze, G. Bihlmayer, A. Kubetzka, O. Pietzsch, S. Blügel, and R. Wiesendanger, Chiral magnetic order at surfaces driven by inversion asymmetry, Nature **447**, 190 (2007).

[4] I. E. Dzyaloshinskii, Thermodynamic theory of "weak" ferromagnetism in antiferromagnetic substances, Sov. Phys JETP **5**, 1259 (1957).

[5] T. Moriya, Anisotropic Superexchange Interaction and Weak Ferromagnetism, Phys. Rev. **120**, 91 (1960).

[6] P. Ferriani, K. von Bergmann, E. Y. Vedmedenko, S. Heinze, M. Bode, M. Heide, G. Bihlmayer, S. Blügel, and R. Wiesendanger, Atomic-Scale Spin Spiral with a Unique Rotational Sense: Mn Monolayer on W(001), Phys. Rev. Lett. **101**, 027201 (2008).

[7] M. Heide, G. Bihlmayer, and S. Blügel, Dzyaloshinskii-Moriya interaction accounting for the orientation of magnetic domains in ultrathin films: Fe/W(110), Phys. Rev. B **78**, 140403(R) (2008).

[8] S. Meckler, N. Mikuszeit, A. Preßler, E. Y. Vedmedenko, O. Pietzsch, and R. Wiesendanger, Real-Space Observation of a Right-Rotating Inhomogeneous Cycloidal Spin Spiral by Spin-Polarized Scanning Tunneling Microscopy in a Triple Axes Vector Magnet, Phys. Rev. Lett. **103**, 157201 (2009).

[9] P. Hohenberg and W. Kohn, Inhomogeneous Electron Gas, Phys. Rev. B **136**, B864 (1964).

[10] W. Kohn and L. J. Sham, Self-Consistent Equations Including Exchange and Correlation Effects, Physical Review **140**, A1133 (1965).

[11] D. R. Hamann, Semiconductor Charge Densities with Hard-Core and Soft-Core Pseudopotentials, Phys. Rev. Lett. **42**, 662 (1979).

[12] E. Wimmer, H. Krakauer, M. Weinert, and A. J. Freeman, Full-potential self-consistent linearized-augmented-plane-wave method for calculating the electronic structure of molecules and surfaces: $O2$ molecule, Phys. Rev. B **24**, 864 (1981).

[13] http://www.flapw.de.

[14] M. Heide, G. Bihlmayer, and S. Blügel, Describing Dzyaloshinskii-Moriya spirals from first principles, Physica B: Condensed Matter **404**, 2678 (2009).

[15] U. von Barth and L. Hedin, A local exchange-correlation potential for the spin polarized case, Journal of Physics C: Solid State Physics **5**, 1629 (1972).

[16] D. M. Ceperley and B. J. Alder, Ground State of the Electron Gas by a Stochastic Method, Phys. Rev. Lett. **45**, 566 (1980).

[17] S. H. Vosko, L. Wilk, and M. Nusair, Accurate spin-dependent electron liquid correlation energies for local spin density calculations: a critical analysis, Can. J. Phys. **58**, 1200 (1980).

[18] V. L. Moruzzi, J. F. Janak, and A. R. Williams, Calculated electronic properties of metals, Pergamon Press, New York, 1978.

[19] R. O. Jones, Introduction to Density Functional Theory and Exchange-Correlation Energy Functionals, volume 31, ed. J. Grotendorst, S. Blügel and D. Marx, John von Neumann Institute for Computing, 2006.

[20] J. P. Perdew, K. Burke, and M. Ernzerhof, Generalized Gradient Approximation Made Simple, Phys. Rev. Lett. **77**, 3865 (1996).

[21] J. P. Perdew, J. A. Chevary, S. H. Vosko, K. A. Jackson, M. R. Pederson, D. J. Singh, and C. Fiolhais, Atoms, molecules, solids, and surfaces: Applications of the generalized gradient approximation for exchange and correlation, Phys. Rev. B **46**, 6671 (1992).

[22] D. J. Singh and J. Ashkenazi, Magnetism with generalized-gradient-approximation density functionals, Phys. Rev. B **46**, 11570 (1992).

[23] M. Heide, Magnetic domain walls in ultrathin films: Contribution of the Dzyaloshinsky-Moriya interaction, PhD thesis, RWTH Aachen, 2006.

[24] A. H. MacDonald and S. H. Vosko, A relativistic density functional formalism, Journal of Physics C: Solid State Physics **12**, 2977 (1979).

[25] G. Baym, Lectures on quantum mechanics, Benjamin Reading Mass., 1974.

[26] A. H. MacDonald, W. E. Pickett, and D. D. Koelling, A linearised relativistic augmented-plane-wave method utilising approximate pure spin basis functions, J. Phys. C: Solid State Phys. **13**, 2675 (1980).

[27] D. D. Koelling and B. N. Harmon, A technique for relativistic spin-polarised calculations, J. Phys. C: Solid State Phys. **10**, 3107 (1977).

[28] A. R. Mackintosh and O. K. Andersen, The electronic structure of transition metals, ed. M. Springford, Cambridge Univ. Press, London, 1980.

[29] A. Oswald, R. Zeller, P. J. Braspenning, and P. H. Dederichs, Interaction of magnetic impurities in Cu and Ag, J. Phys. F: Met. Phys. **15**, 193 (1985).

[30] A. I. Liechtenstein, M. I. Katsnelson, V. P. Antropov, and V. A. Gubanov, Local spin density functional approach to the theory of exchange interactions in ferromagnetic metals and alloys, J. Magn. Magn. Mater. **67**, 65 (1987).

[31] J. C. Slater, Wave Functions in a Periodic Potential, Phys. Rev. **51**, 846–851 (1937).

[32] T. Loucks, Augmented plane wave method, Benjamin, 1967.

[33] O. K. Andersen, Linear methods in band theory, Phys. Rev. B **12**, 3060 (1975).

[34] D. D. Koelling and G. O. Arbman, Use of energy derivative of the radial solution in an augmented plane wave method: application to copper, Journal of Physics F: Metal Physics **5**, 2041 (1975).

[35] H. Krakauer, M. Posternak, and A. J. Freeman, Linearized augmented plane-wave method for the electronic band structure of thin films, Phys. Rev. B **19**, 1706 (1979).

[36] P. Kurz, F. Förster, L. Nordström, G. Bihlmayer, and S. Blügel, Ab initio treatment of noncollinear magnets with the full-potential linearized augmented plane wave method, Phys. Rev. B **69**, 024415 (2004).

[37] P. H. Dederichs, S. Blügel, R. Zeller, and H. Akai, Ground States of Constrained Systems: Application to Cerium Impurities, Phys. Rev. Lett. **53**, 2512 (1984).

[38] C. Herring, Exchange interactions among itinerant electrons, ed. G. T. Rado, H. Suhl, Academic Press, New York, London, 1966.

[39] L. M. Sandratskii, Energy Band Structure Calculations for Crystals with Spiral Magnetic Structure, phys. stat. sol. (b) **136**, 167 (1986).

[40] L. M. Sandratskii, Symmetry analysis of electronic states for crystals with spiral magnetic order. I. General properties, J. Phys.: Condens. Matter **3**, 8565 (1991).

[41] S. J. Youn, W. Mannstadt, and A. J. Freeman, Analytic Spin-Orbit Coupling Matrix Element Formulae in FLAPW Calculations, J. Comput. Phys. **172**, 387 (2001).

[42] T. Yildirim, A. B. Harris, A. Aharony, and O. Entin-Wohlman, Anisotropic spin Hamiltonians due to spin-orbit and Coulomb exchange interactions, Phys. Rev. B **52**, 10239 (1995).

[43] G. van der Laan, Microscopic origin of magnetocrystalline anisotropy in transition metal thin films, Journal of Physics: Condensed Matter **10**, 3239 (1998).

[44] N. S. Akulov, Zur Theorie der Feinstruktur der Magnetisierungskurven der Einkristalle, Z. Physik **69**, 78 (1931).

[45] I. E. Dzyaloshinskii, Theory of helicoidal structures in antiferromagnets. III., Sov. Phys JETP **20**, 665 (1965).

[46] Y. A. Izyumov, Modulated, or long-periodic, magnetic structures of crystals, Sov. Phys Usp. **27**, 845 (1984).

[47] A. Aharoni, Introduction to the Theory of Ferromagnetism (The International Series of Monographs on Physics), Oxford University Press, USA, 2001.

[48] B. Santos, J. M. Puerta, J. I. Cerda, R. Stumpf, K. von Bergmann, R. Wiesendanger, M. Bode, K. F. McCarty, and J. de la Figuera, Structure and magnetism of ultra-thin chromium layers on W(110), New Journal of Physics **10**, 013005 (2008).

[49] S. Heinze, private communication, 2010.

[50] F. Schubert, private communication, 2009.

[51] T. Schena, private communication, 2010.

[52] S. Schröder, P. Ferriani, and S. Heinze, Non-collinear magnetism in the Mn double layer on W(110), Frühjahrstagung der DPG, MA 31.4, 2010.

Selbständigkeitserklärung

Hiermit versichere ich, die vorliegende Arbeit selbständig und nur unter Zuhilfenahme der angegebenen Quellen und Hilfsmittel angefertigt zu haben.

_____

Bernd Zimmermann
Jülich, den 11. Mai 2010